Determining the Wavelength Dependancy of the Optical Properties of the Glacial Ice Using In-situ Light Sources

Amirreza Raissi

Supervisor: Assoc Prof. Jenni Adams

Department of Physics and Astronomy
University of Canterbury

A thesis submitted to the University of Canterbury in fulfilment
of the requirements for the degree of
Doctor of Philosophy

2021

Contents

List of Figures

List of Tables

Abstract

Neutrinos are unique cosmic messengers, their weak interactions and lack of electric charge means they can travel from cosmic distances, without absorption or deflection. IceCube is a neutrino observatory constructed at depths of 1450-2450 m below the surface at the South Pole. The main objective of IceCube is to detect astrophysical neutrinos to enable a better understanding of high-energy cosmic rays including their production mechanism and also their origins.

IceCube observes neutrinos through detecting the light emitted by the products of neutrino interactions. Characterisation of the optical properties of the glacial ice is necessary for the physical parameters of the neutrinos, such as their energies and directions, to be determined from the pattern and timing of the light detected. Embedded LEDs within the deployed modules enable the generation of in-situ light with five different wavelengths. This light can be detected by the detector array and used to determine the optical properties of the instrumented ice.

The main focus of this thesis was to investigate and parameterise the wavelength dependence of the absorption and scattering coefficients of the ice. The values found for the parameters characterising this wavelength dependence were consistent with previous measurements although slightly different values were obtained. While the new parameters are considered to be more robust than past measurements due to improved knowledge of the light emitters, it is recommended that this study is revisited when the observed anisotropic light propagation has been further modelled.

In addition to the main study into the wavelength dependence of the optical properties of the ice, investigations were also undertaken to characterise properties of the optical modules such as their orientation.

Calibration tools developed and used in this thesis will be of use when the IceCube upgrade devices are deployed, allowing our knowledge and characterisation of the ice to be improved significantly.

"Science may set limits to knowledge, but should not set limits to imagination."

— Bertrand Russell

Acknowledgement

Foremost, I would like to express my sincere gratitude to my supervisor Prof. Jenni Adams for the continuous support of my Ph.D study and research, for her patience, enthusiasm, and immense knowledge. Her guidance helped me in all the time of research and writing of this thesis.

My completion of this project could not have been accomplished without the support of the members of IceCube calibration working group, in particular, Dr. Martin Rongen, Dr. Dmitry Chirkin, and Prof. Allan Hallgren. I would like to thank them deeply for their support and patience throughout countless calls, meetings and mail discussions.

Finally, to my caring, loving, and supportive wife, Mahsa: my deepest gratitude. Your encouragement when the times got rough are much appreciated and duly noted. It was a great comfort and relief to know that you were willing to provide management of our household activities while I completed my work. My heartfelt thanks.

1 Neutrino Astronomy

The Universe can be observed with a range of different particles including cosmic rays, neutrinos and electromagnetic radiation over a range of wavelengths. Although electromagnetic radiation has revealed many details of high-energy astrophysical objects, the rate of absorption of gamma rays with energies exceeding 10^{12} eV is very high. While cosmic rays with extremely high energies have been detected, due to their electric charge, their trajectories are bent in magnetic fields making their origin difficult to determine. Neutrinos, on the other hand, interact only by the weak interaction, meaning they can reach us from the most extreme objects, and from cosmological distances. Furthermore, as they are neutral particles, their path is unaffected by magnetic fields and they can point directly back to the site of their origin. Figure 1.1 is an illustration of these different cosmic messengers. The unique messenger properties of neutrinos has motivated the field of neutrino astronomy and the construction of large telescopes to detect astrophysical neutrinos. This thesis is concerned with the calibration of the detecting medium of IceCube, which is currently the largest operating neutrino telescope.

In this chapter, the first section introduces cosmic rays including their production mechanisms, the sources in which those mechanisms occur and why they are relevant to neutrino astronomy. The second section includes a short review of neutrinos and their properties in the Standard Model of Particle Physics. In the third section I give a review of the different classifications of neutrinos based on their energy ranges and their origins. The connections between high-energy neutrinos and cosmic rays and other astronomical messengers are discussed in the final section of this chapter.

1.1 Cosmic Rays

Cosmic rays are ionized nuclei which enter the Earth's atmosphere. The cosmic ray composition varies with energy. Overall protons are the most dominant making up around 90% followed by alpha particles which constitute around 9% and heavier nuclei making up the remaining component. Cosmic rays with energies extending up to eleven orders of magnitude greater than the equivalent rest mass energy of a proton or 3×10^{20} eV have been detected[1]. These ultra-relativistic energies make

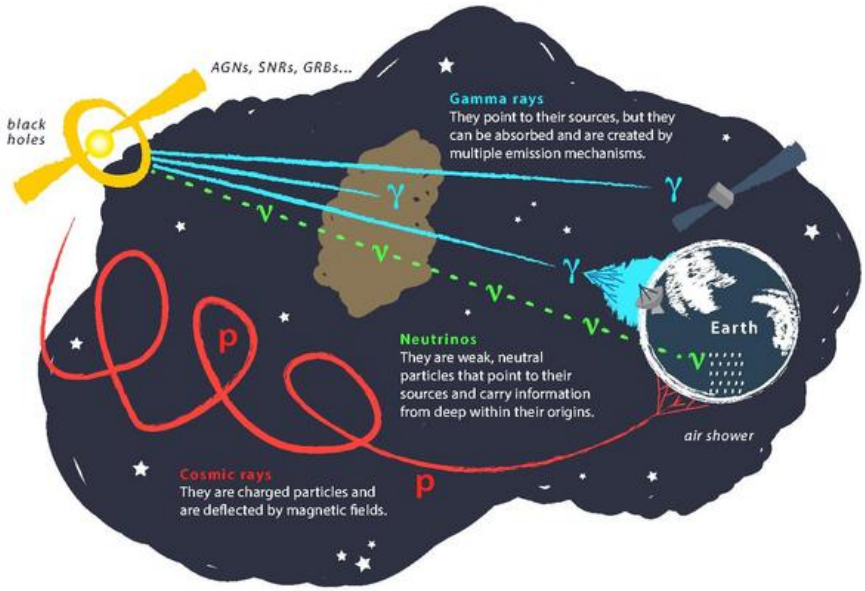

Figure 1.1: Schematic depiction of the different astronomical messengers and their propagation properties. [IceCube collaboration (2019). "Internal graphics resource"]

up a very small fraction of cosmic rays, but their existence raises a fundamental question about the mechanisms that can accelerate those particles to such high energies. Investigating the origin of cosmic rays and their acceleration mechanisms is the target of many research programmes including those of neutrino telescopes such as IceCube.

Cosmic rays are observed over a wide range of energies as can be seen from the cosmic ray spectrum shown in figure 1.2. Apart from particles associated with solar flares which are at relatively low energies, cosmic rays originate outside our Solar System. Although the origin of the majority of cosmic rays is our own Galaxy, the fact that ultra-high energy cosmic rays have gyro-radii larger than the size of the Galaxy suggests that they are most likely to have extragalactic origins[2].

The cosmic ray spectrum is close to following a single power law which could be due to common acceleration mechanisms in action, in a range of different astrophysical objects. There are some features of the spectrum however, where the spectral index changes. At energies around 10^6 GeV, the spectral index changes from 2.7 to 3.0 and this transition is called the spectral knee. A second steepening which occurs around 10^8 GeV is known as the second knee. A further transition which occurs at energies above 10^9 GeV is called the spectral ankle and as we can see from figure 1.2 at this point the spectral index changes back to around 2.7 again. The knee and second knee are believed to result from a changing origin and/or composition of the

cosmic rays. It is generally accepted that the cosmic rays with energies above the ankle have an extra-galactic origin[3].

The interactions of high energy cosmic rays with the 2.7 K relic Cosmic Microwave Background (CMB) radiation reduces the energy of the cosmic rays and provides a limit on the highest energy protons which could propagate to Earth. This energy threshold, at 5×10^{19} eV, is known as the Greisen-Zatsepin-Kuzmin (GZK) cut-off [4]. Protons above this energy, interacting with the abundant CMB photons have a centre–of–mass energy sufficient to produce a Δ^+ resonance.

Before the era of particle accelerators, our knowledge about the elementary particles were mainly based on the cosmic rays and their interactions. Due to technological limitations the reachable energies in particle accelerators cosmic rays are still a key means for investigation of particle cross sections at ultra-high energies. For example, the IceCube neutrino telescope can probe neutrino–nucleon cross sections utilising the different path lengths traveled through the Earth for neutrinos arriving from different zenith angles [5].

Direct detection of cosmic rays is only possible in space or at high altitude by balloon-borne instruments. But since the flux of cosmic rays decreases with energy the highest energy cosmic rays cannot be observed with small detectors above the atmosphere due to the rarity of particles incident on the small collecting area. However, those incoming high-energy cosmic rays produce atmospheric cascades that can be observed by large air shower arrays exposed for long periods on the surface. This indirect detection method is currently the only method with which ultra-high energy cosmic rays are detected. The first interaction with an air molecule initiates a hadronic cascade. The decay of neutral pions in this cascade into high energy photons then starts a simultaneously developing electromagnetic cascade, driven by Bremsstrahlung and pair production. In addition, charged mesons decay into long range muons. While cosmic ray detectors seek to detect the air shower particles in order to study cosmic rays, for neutrino telescopes the air showers are a source of background particles in their study of astrophysical neutrinos. Figure 1.10 shows a cartoon of a cosmic ray air shower in the context of the production of atmospheric neutrinos in air showers.

1.1.1 Acceleration Mechanism

The aim of this section is to introduce the theory of shock acceleration and its possible role as the source of high energy cosmic rays.

When the energy of a moving magnetized plasma transfers to charged particles, the energy of the charged particles will increase, and can eventually grow to many

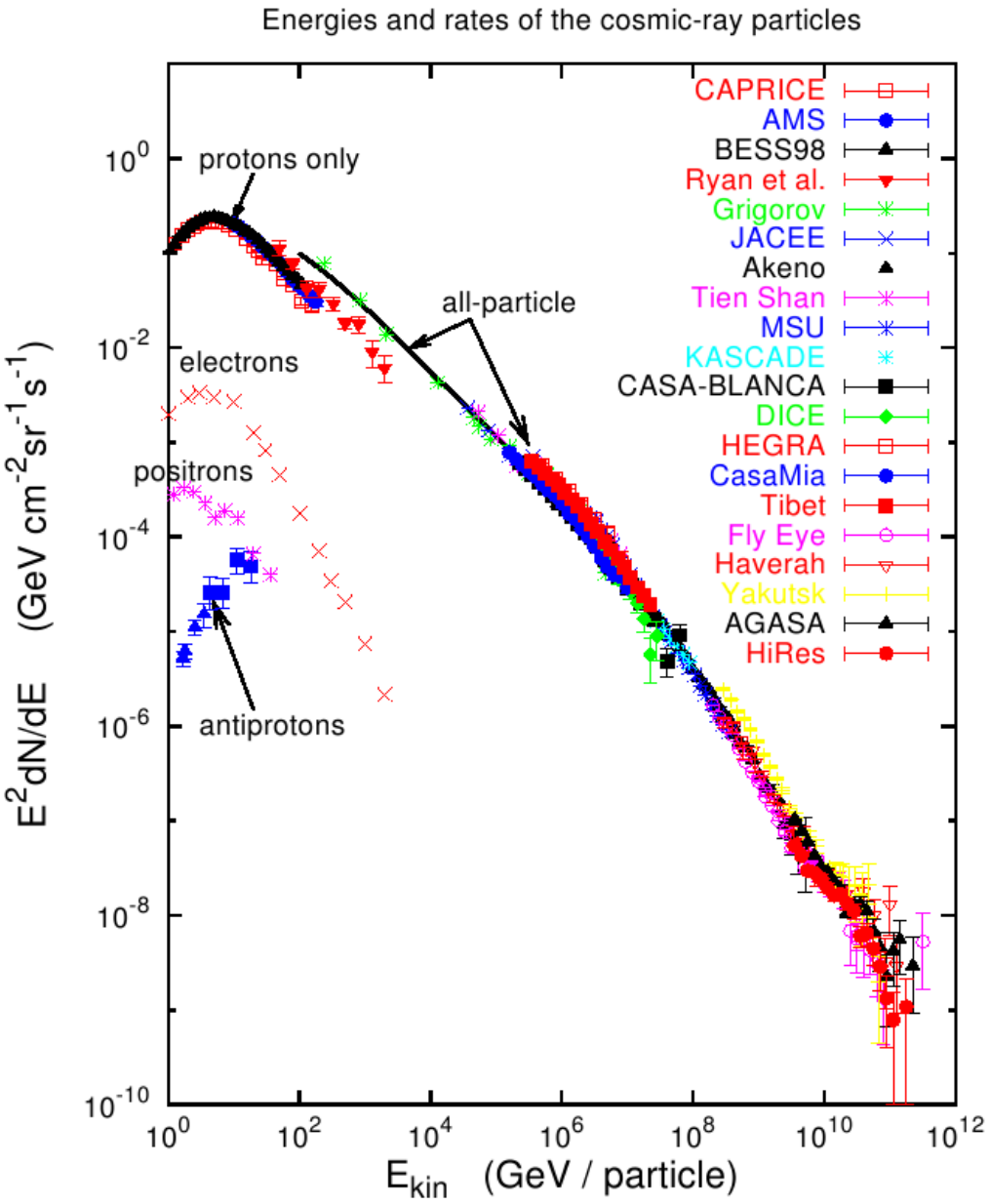

Figure 1.2: Energies and rates of cosmic-ray particles observed by different experiments. Cosmic-ray energies extend up to greater than 10^{20} eV. The spectral knee is seen at 10^6 GeV, arising from the origin of cosmic-rays changing from galactic to extragalactic sources. The spectral ankle is seen at 10^9 GeV. [Anthony M. Hillas. Cosmic Rays: Recent Progress and some Current Questions.Cosmology, Galaxy Formation and Astroparticle Physics on the pathway to the SKA Conf. Proc., 2006.]

times their initial value, resulting in the non-thermal energy distribution that is characteristic of cosmic rays. Fermi acceleration refers to the acceleration that charged particles undergo through multiple reflections[6]. Much of the theory related to Fermi acceleration at shock fronts was developed by Bell [7]. Figure 1.3 is a

cartoon illustrating Bell's shock acceleration. The aim of this section is to introduce the theory of shock acceleration and its possible role as the mechanism for the acceleration of high energy cosmic rays. Here, through a simple model, we will motivate some of the basic predictions of Fermi acceleration including the spectral index for the accelerated cosmic-ray spectrum.

Consider particles which undergo repeated interactions, with each interaction resulting in the particles gaining a constant fraction ξ of their energy. In addition, the probability of a particle to be lost from the acceleration site after each interaction is introduced to be $P_{\rm esc}$. After n interactions each particle has an energy

$$E_n = E_0(1+\xi)^n, \tag{1.1}$$

and the probability of remaining in the acceleration region after n encounters is $(1-P_{\rm esc})^n$. From equation 1.1 we can express the number of encounters required to reach energy E as,

$$n = \ln(\frac{E}{E_0})/\ln(1+\xi). \tag{1.2}$$

Thus we can see the number of particles reaching energy E_n decreases as

$$N(>E_n) \propto (1-P_{\rm esc})^n = (1-P_{\rm esc})^{\frac{\ln(E_n/E_0)}{\ln(1+\xi)}} = \left(\frac{E_n}{E_0}\right)^{\frac{\ln(1-P_{\rm esc})}{\ln(1+\xi)}}. \tag{1.3}$$

With the assumption that $P_{\rm esc}$ and ξ are energy independent, a power-law spectrum of the form

$$N(>E_n) \propto \left(\frac{E_n}{E_0}\right)^{-\alpha} \tag{1.4}$$

is expected, with $\alpha = -\ln(1-P_{esc})/\ln(1+\xi)$. Given $P_{esc} \ll 1$ and $\xi \ll 1$ yields $\alpha \approx \frac{P_{\rm esc}}{\xi}$. Consequently, the differential spectral index γ for the energy spectrum $d\Phi/dE$ is:

$$\gamma = \alpha + 1 \approx 1 + \frac{P_{\rm esc}}{\xi}. \tag{1.5}$$

This mechanism is predicted to be occurring at shock-fronts, which are the magnetic boundary surfaces between plasma fields that are in collision with each other. Shock fronts are present in many astrophysical environments such as in the jets of active galactic nuclei and supernova blast waves [8].

For a strong shock, the relative energy gain and the escape probability are found to be equal, $\xi = P_{\rm esc}$, and in this case $\gamma \approx 2$. This is the generic prediction from Fermi shock acceleration for the spectral index for the cosmic-ray source spectrum. The cosmic ray spectrum observed on Earth has a spectral index between 2.3 and

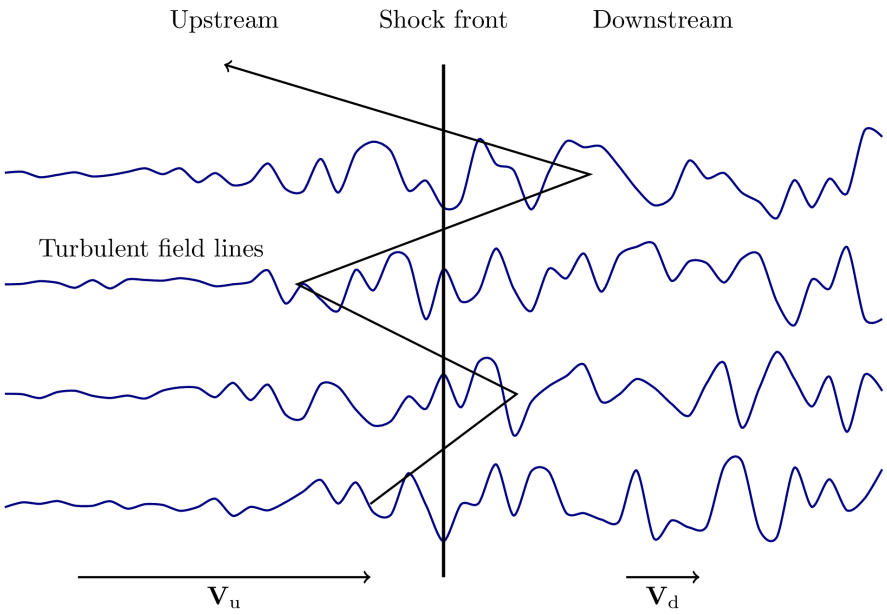

Figure 1.3: Picture of Bell's diffusive shock acceleration. Each encounter with the shock yields an average gain of energy, due to the converging flow velocities at the shock front. [courtesy of Dr. Mark Pulupa's space physics. Illustration: http://sprg.ssl.berkeley.edu/∼pulupa/illustrations/]

2.7 as discussed above. The altered spectrum is believed to be due to the energy dependent diffusion processes which the cosmic rays are subjected to during their propagation[9].

We now consider the timescales involved in the acceleration process. Firstly we return to the spectral index α, which, as we argued above is approximately $\frac{P_{\mathrm{esc}}}{\xi}$. The probability of escape from the acceleration site per encounter is the ratio of the characteristic time for the acceleration cycle, T_{cycle} and the characteristic time for escape from the acceleration region, T_{esc}. Thus we can express α as

$$\alpha \approx \frac{P_{\mathrm{esc}}}{\xi} = \frac{1}{\xi} \times \frac{T_{\mathrm{cycle}}}{T_{\mathrm{esc}}}. \tag{1.6}$$

After the acceleration process has been working for a time t the maximum number of encounters is $n_{max} = t/T_{\mathrm{cycle}}$ and

$$E \leqslant E_0(1+\xi)^{(t/T_{cycle})}. \tag{1.7}$$

Two characteristic features of Fermi acceleration can be seen from equation 1.7. Firstly, higher energy particles will take longer to accelerate than lower energy particles. And secondly, if a certain kind of Fermi accelerator has a limited lifetime (i.e. T_A), then it will also be characterized by a maximum energy per particle that it can produce.

The relationship between the maximum energy to which particles can be accelerated at a given site, and the characteristics of particular sites is expressed through the Hillas criterion. The Hillas criterion is based on magnetic confinement and requires that the size of the acceleration region has to be at least the particle's Larmor radius [2]. This indicates a maximum energy of:

$$E_{\max} \leq 10^{19}\mathrm{eV}.Z.\beta_S.\frac{R}{\mathrm{kpc}}.\frac{B}{\mu\mathrm{G}} \tag{1.8}$$

where Z is the atomic number for the particle, $c\beta_S$ is the shock velocity, R is the size of the acceleration region and B is the magnetic field confining particles in the region. Figure 1.4 shows the maximum proton energy possible for various potential source classes based on the Hillas criterion and their typical size and magnetic fields.

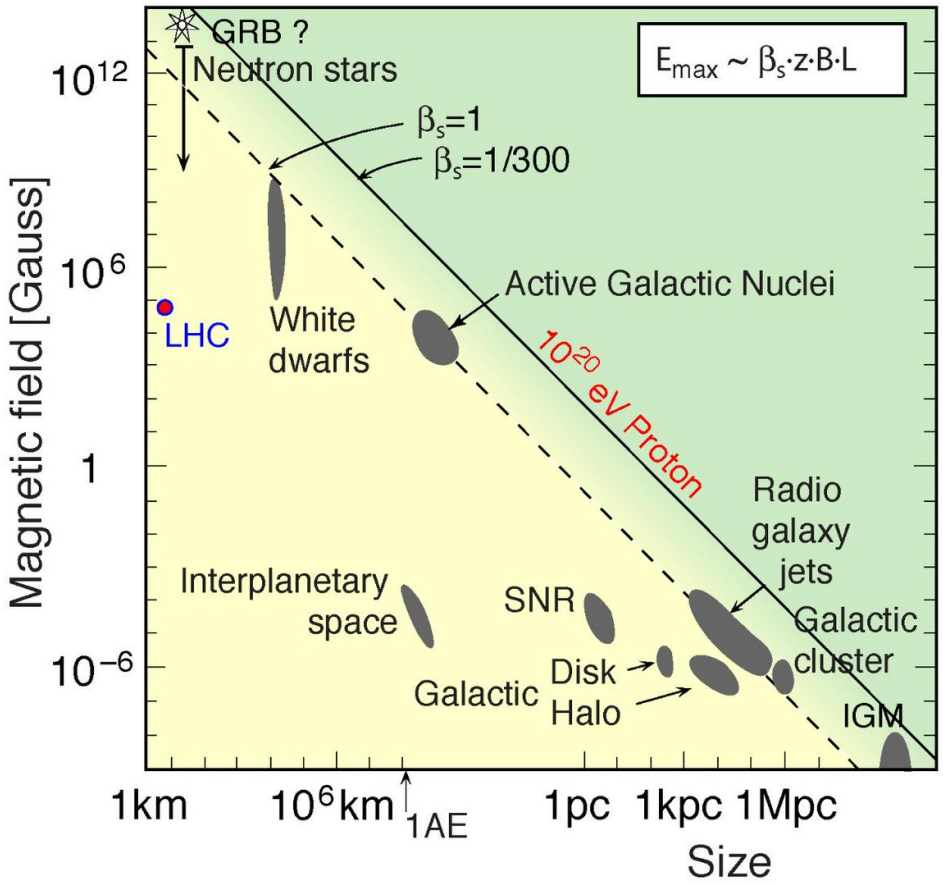

Figure 1.4: Hillas plot, depicting the typical size and magnetic field of potential source classes of ultra high energy cosmic rays and their resulting maximum energy as expected from the gyroradius. [Ralph Engel et al. (Oct. 2009)."Cosmic rays from the knee to thehighest energies"]

1.1.2 Cosmic Ray Origins

The population of cosmic rays is believed to be made up of solar, galactic and extragalactic components. Particles of solar origin are limited to energies below a few tens of GeV. The energy level marking the transition between galactic and extragalactic cosmic rays is not known with certainty but is believed to be in excess of 10^{15} eV.

Solar energetic particles (SEPs) are high-energy particles coming from the Sun. They consist of protons, electrons and other high-energy ionized nuclei with energies ranging from a few keV to many GeV. SEPs mostly originate from solar-flare sites. Other origins such as shock waves associated with coronal mass ejections for SEPs have been also discovered, but they account for a small percentage of the total detected SEPs. Two main mechanisms of acceleration of SEPs are diffusive shock acceleration and shock-drift mechanism. The former is an example of Fermi acceleration. Within only 5% of the Sun-Earth distance ($5 - 10$ solar radii) SEPs can be accelerated to an energy range as high as several MeV [10]. The Earth's magnetic field has a strong effect on SEP and their ability to reach the surface of the Earth. While cosmic rays in this energy range, and associated neutrinos are not the main target for IceCube, studies using the telescope have been made searching for neutrino emission in coincidence with solar flares [11].

The sources of high-energy cosmic rays are largely unknown. Although a study conducted in 2015 of cosmic-ray directions with the Pierre-Auger Observatory suggested a correlation between the arrival directions of cosmic rays of the highest energies of more than 5×10^{19} eV and the positions of nearby active galaxies [12], this correlation diminished with further years of observations.

The main acceleration sites for galactic cosmic rays are assumed to be in the shock waves associated with supernova shock fronts. Proposed extragalactic sources include gamma ray bursts, active galactic nuclei and starburst galaxies. These sources will be briefly reviewed below.

- **SuperNova Remnant (SNR)**

  When a massive star collapses with a supernova explosion it converts to either a very compact spinning neutron star or to a blackhole. Ejected material expands as a shock wave into the interstellar medium. These expanding shock waves of relativistic electrons are called SuperNova Remnant (SNR). They are believed to be the major source of galactic cosmic rays. Figure 1.5 shows a schematic view of an SNR in which the yellow outgoing arrows illustrate the expanding shock.

  Supernovae exist in both normal galaxies and StarBurst galaxies (SBGs), but

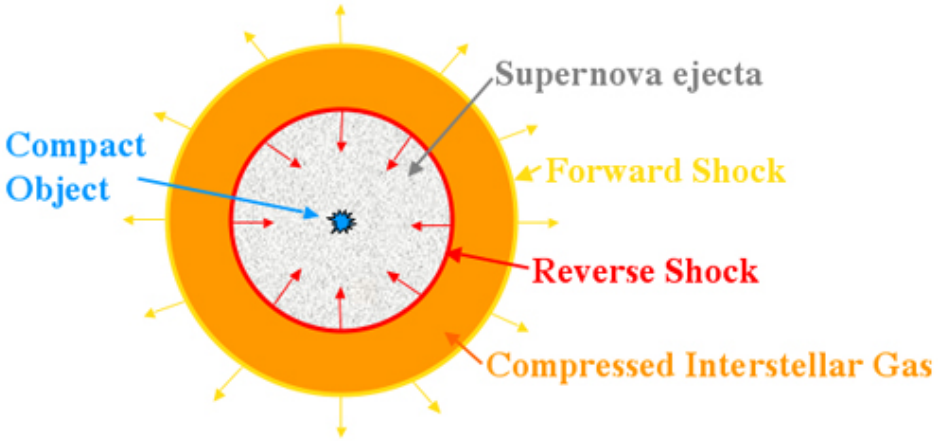

Figure 1.5: Schematic of SNe Remnant. A forward and a reverse shock are created when the supernova shock wave interacts with the interstellar medium. The forward shock continues to expand into the interstellar medium, the reverse shock travels back into the freely expanding supernova ejecta. [COSMOS - The SAO Encyclopedia of Astronomy: `https://astronomy.swin.edu.au/cosmos/S/Supernova+Remnant`]

SBGs make more SNe during their starburst phase than normal galaxies [13]. The ejecta velocities of SNe can reach up to $V_{\rm ej} \sim 10^9$ cm s^{-1} but there is a subclass of supernovae, called hypernovae (HNe) with ejecta velocities which can reach semi-relativistic values. The ejecta kinetic energies of HNe can reach up to 10^{52} erg and the ejecta kinetic energies of SNe can reach up to $10^{50}-10^{51}$ erg. Applying the Hillas criterion, equation 1.8, the maximum cosmic-ray energy achievable by Fermi shock acceleration is greater than $10^{15}Z$ eV for SNe and $\rm E_{max} \sim 10^{17}Z$ eV for HNe [14].

- **Active Galactic Nuclei (AGN)**

  AGNs are compact and bright regions at the centre of galaxies with a supermassive blackhole and an accretion disk which is formed by the cold materials close to the centre. AGNs are a small fraction of all galaxies in which their galactic nucleus is a source of radio or X-ray photons with a bright jet emanating from their nucleus.

  AGNs by their luminosity and radio emission can be classified to [15]: 1- Low luminosity AGNs (LLAGNs) with luminosities in the range of 10^{43} erg s^{-1}, 2- Radio-quiet AGNs (RQ AGNs) that are normal AGN with luminosities up to 4-5 orders of magnitude higher than LLAGNs, and 3- Radio-loud AGNs (RL AGNs) which are another subgroup of normal AGNs with luminosities similar to RQ AGNs, but unlike RQ AGNs in which radio and X-ray nuclear emissions

are the dominant emission, in RL AGNs the luminous jets can be detected not only in radio but in some cases also in optical, X and/or gamma-rays.

- **Gamma-ray Burst (GRB)**

  Gamma-ray bursts (GRB) are relativistically expanding fireballs which are extremely energetic and bright. There are at least two progenitors for gamma-ray burts. One progenitor is believed to be a specific type of supernova called a hypernova and is the core-collapse event of a massive star of more than 9 solar masses. The second progenitor is the merger of compact binary systems like neutron stars. GRBs are the most energetic explosions in the Universe and result in highly relativistic jets which emerge from the collapsing or merging system.

  An afterglow comes after the prompt emission which is slowly decaying. The energy range of the photon spectra of both afterglow and also the prompt emission is due to the mechanism of electron synchrotron and inverse Compton scattering [16] and both are non-thermal. The main difference between the prompt emission and the afterglow is the region of their acceleration. The prompt emission typically is the result of acceleration in internal shocks inside the jet usually via $p\gamma$ interactions and has been hypothesized to produce neutrinos to TeV energy ranges [17], while afterglows acceleration happen in an external shock where the jets go to the external medium and the energy of resulted neutrinos is in the range of EeV [18]. Higher energy neutrinos are also expected, GeV neutrinos for instance can be produced from pp and $p\gamma$ interactions (see the next section of this thesis) in the photosphere (the star's outer shell from which light is radiated) [19].

- **Starburst galaxies (SBGs)**

  When normal galaxies undergo periods of intense star formation, with rates around $\dot{\mathrm{M}}_\star \sim 1-10\mathrm{M}_\odot\ \mathrm{yr}^{-1}$, they are called starburst galaxies or SBGs. These episodes of star formation in SBGs are longer than the lifetime of ordinary young massive stars and last 10^6-10^7yr. Normal galaxies typically experience these episodes of star-formation several times and about 20-30% of all star formation in the Universe occurs in SBGs [13]. In figure 1.6 you can see a Hubble Space Telescope image of The Antennae Galaxies which are an example of a starburst galaxy occurring from the collision of NGC 4038/NGC 4039 of NGC 4038 (top) and NGC 4039 (bottom).

  There are other stellar sources in starburst galaxies which have been considered

for producing very high energy neutrinos, including magnetars, young pulsars and macro-novae, etc.

Figure 1.6: The Antennae Galaxies are an example of a starburst galaxy occurring from the collision of NGC 4038/NGC 4039. [NASA/ESA Hubble Space Telescope, (2009).]

1.1.3 Cosmic ray multimessenger connection

The identification of the sources of cosmic rays is difficult due to their deflection in magnetic fields. However if cosmic rays interact close to their source site then the gamma rays and neutrinos produced in the interactions will point back to the sources.

These neutrinos are usually referred to as high-energy astrophysical neutrinos and their detection was the key motivation for the construction of the IceCube detector. Cosmic ray protons can undergo interactions with either photons or protons. Proton–proton interactions produce neutrons or various mesons

$$p + p \rightarrow \pi^{\pm}, \pi^{0}, n \ldots \tag{1.9}$$

Proton interactions with a radiation field can also produce unstable mesons. The

$p\gamma$ cross section is enhanced at the Δ^+ resonance

$$p + \gamma \rightarrow \Delta^+ \rightarrow n + \pi^+ \tag{1.10}$$

$$\rightarrow p + \pi^0 \tag{1.11}$$

Subsequent decays produce gamma rays and neutrinos

$$\pi^0 \rightarrow \gamma + \gamma \tag{1.12}$$

$$\pi^+ \rightarrow \nu_\mu + \mu^+ \tag{1.13}$$

$$\rightarrow e^+ + \nu_e + \bar{\nu}_\mu \tag{1.14}$$

As indicated by the equations above, the interactions of cosmic-ray protons produce neutral and charged pions, with the neutral pions decaying to gamma rays and the charged pion decays producing neutrinos. Thus gamma rays and neutrinos are potential tracers for identifying the regions where cosmic rays are accelerated. However, given gamma rays can also be produced by inverse Compton scattering of electron synchrotron photons, their observation cannot be uniquely associated with proton acceleration. Furthermore at energies above tens of GeV, gamma rays interact readily, limiting the horizon for studying the Universe with high-energy photons. This motivates the detection of neutrinos for the identification of the sites of cosmic ray acceleration. The flux and spectrum expected of the produced neutrinos is model dependent and varies with assumptions of the source cosmic ray flux, source density, and energy transferred from the cosmic rays to the secondary particles.

The usual assumption is that the interaction length in the source medium is much larger than the decay length for muons. In this scenario the neutrinos are produced with a flavour ratio of $\nu_\mu : \nu_e = 2 : 1$ at the astrophysical sources [20]. However, due to neutrino oscillations (discussed in 1.2.2) as they travel through the interstellar medium, neutrinos from high energy astrophysical sources are expected to be observed at the Earth with a flavour ratio of $\nu_\tau : \nu_\mu : \nu_e = 1 : 1 : 1$ [21]. There are other possible scenarios which predict different source flavour ratios such as the astrophysical neutrinos originating from neutron decay [22] or when the source is sufficiently high density that muons interact or lose energy before decaying to neutrinos[23]. These scenarios predict, respectively, flavour ratios of $1 : 0 : 0$ and $0 : 1 : 0$ at source, which after oscillation, give flavour ratios at Earth of $0.55 : 0.19 : 0.2$ and $0.19 : 0.43 : 0.38$.

1.2 Introduction to Neutrinos

As motivated above, neutrinos are unique cosmic messengers due to their low interaction rate and ability to travel undeflected by magnetic fields. In this section I will provide some background to neutrinos, covering their place in the standard model of particle physics, their interactions and oscillation properties.

In the Standard Model of Particle Physics, all elementary particles are classified into two main groups: fermions which have half integer spin and bosons which possess integer spin. Quarks and leptons are the two subgroups of the fermionic family and neutrinos belong to the latter. There are three generations of leptons, each generation consists of one charged and one neutral particle. The charged leptons are the electron, the muon and the tau. Each of these charged particles has a neutral counterpart called the electron neutrino (ν_e), the muon neutrino (ν_μ) and the tau neutrino (ν_τ) respectively. Figure 1.7 represents the classification of these elementary blocks of nature in the Standard Model of Particle Physics.

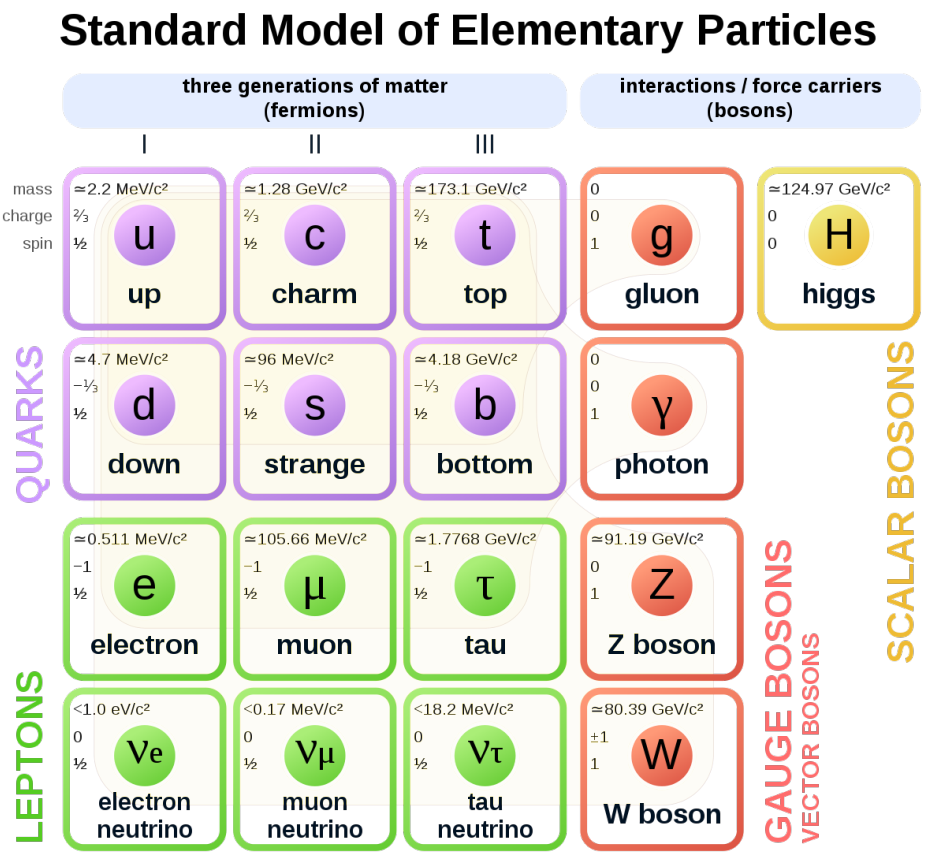

Figure 1.7: Fermions & bosons in the Standard Model of Particle Physics. [Wikimedia Commons (2018d). Standard Model of Elementary Particles]

1.2.1 Neutrino interactions

Neutrinos interact with nucleons via the electroweak interaction by exchanging $W^{\pm}$ or Z^0 bosons [24]. These interactions are classified into two types depending on the mediator of the interaction both with a very small cross-section. The charged-current "CC" interaction is mediated via the exchange of $W^{\pm}$ bosons, and the neutral-current "NC" interaction is mediated via the exchange of a Z^0 boson. Above 10 GeV, as relevant for neutrino telescopes, these two types of interactions dominate the cross section. Regardless of the interaction type in both the CC and NC cases, energy will be transferred to the quark in the nucleon, which recoils and produces a shower of hadronic particles. The energy proportion transferred to the hadronic shower is referred to as the inelasticity. The average inelasticity is a function of the energy of the incoming neutrino with the average around 0.2-0.4 at the neutrino energies relevant for IceCube[1].

As can be seen in figure 1.8 the total cross-section of neutrinos and anti-neutrinos rise at all energies above 100 GeV except for energies above several TeV where the momentum transfer becomes greater than the mass of the exchanged boson in the interactions and the slope declines. An interesting phenomenon is the Glashow Resonance which occurs at an energy of 6.325 PeV, where the anti-electron neutrino can resonantly produce a W-boson in the s-channel through the interaction with an electron at rest [26]. This process happens when the centre-of-mass energy of the system reaches the mass of the mediating boson. The interaction probability for electron Glashow Resonance locally exceeds the regular presented cross-section by more than one order of magnitude in PeV energy ranges.

Further discussion of the signatures for neutrino interactions in IceCube is given in section 2.5.

1.2.2 Neutrino Oscillations

Neutrinos exhibit an effect called oscillation, where the flavor composition of a neutrino beam changes during propagation. In 1927 it was predicted by an Italian and Soviet nuclear physicist, Bruno Pontecorvo, that the flavour of neutrinos should change during their propagation. That is, a neutrino which was generated with a certain flavour might end up having a different flavour after travelling some distance. In the "standard model of particle physics", elementary particles are defined as the eigenstates of a Hamiltonian where a minimal set of orthogonal eigenstates

[1] A recent IceCube study of the inelasticity distribution of multi-TeV neutrino interactions is presented in [25].

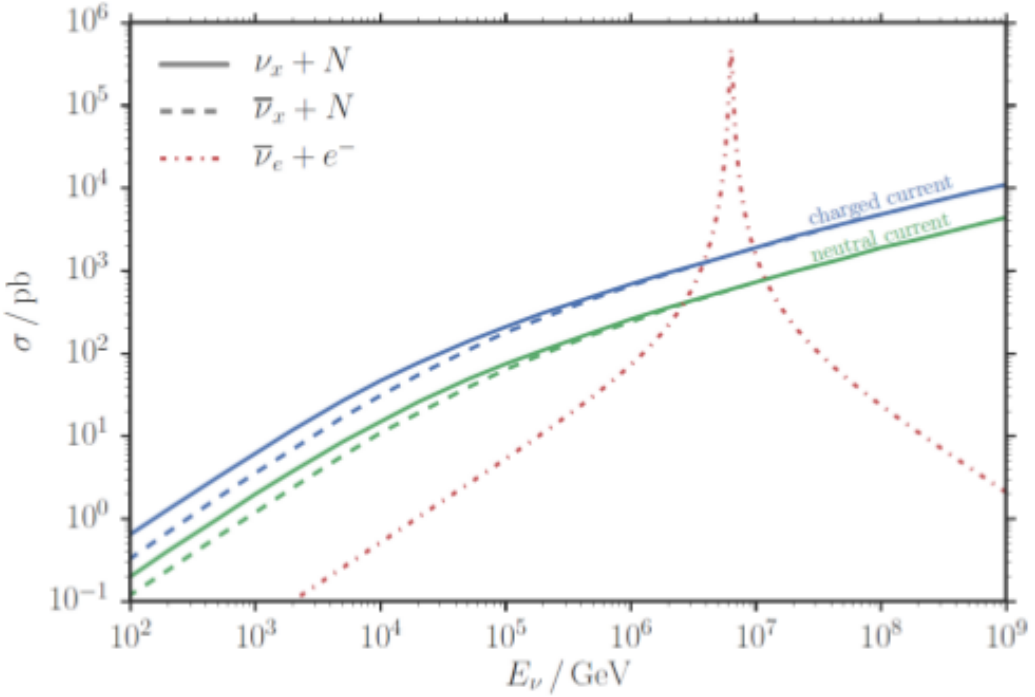

Figure 1.8: Cross sections for charged and neutral current neutrino interactions as well as the Glashow resonance. [Leif Rädel . "Measurement of High-Energy Muon Neutrinos with the IceCube Neutrino Observatory." RWTH Aachen University, (2017).]

forms a basis. For neutrinos, due to their so called oscillation behaviour, their interaction-flavour basis is not necessarily similar to their vacuum propagation-mass basis. *Pontecorvo-Maki-Nakagawa-Sakat (PMNS)* matrix (denoted by "U" below) is used [27] to express the neutrino transformation between these two sets of bases through a unitary rotation:[2]

$$\begin{pmatrix} \nu_e \\ \nu_\mu \\ \nu_\tau \end{pmatrix} = \begin{pmatrix} U_{e1} & U_{e2} & U_{e3} \\ U_{\mu 1} & U_{\mu 2} & U_{\mu 3} \\ U_{\tau 1} & U_{\tau 2} & U_{\tau 3} \end{pmatrix} \cdot \begin{pmatrix} \nu_1 \\ \nu_2 \\ \nu_3 \end{pmatrix} \tag{1.15}$$

where:

[2] $\langle \nu_i | = \sum_i U^*_{a_i} \langle \nu_i |$ where $\langle \nu_a |$ is a flavour and $\langle \nu_i |$ is a mass eigenstate.

$$
\begin{aligned}
U &= \begin{pmatrix} c_{12}c_{13} & s_{12}c_{13} & s_{13}e^{-i\delta} \\ -s_{12}c_{23} - c_{12}s_{23}s_{13}e^{i\delta} & c_{12}c_{23} - s_{12}s_{23}s_{13}e^{i\delta} & s_{23}c_{13} \\ s_{12}s_{23} - c_{12}c_{23}s_{13}e^{i\delta} & -c_{12}s_{23} - s_{12}c_{23}s_{13}e^{i\delta} & c_{23}c_{13} \end{pmatrix} \\
&\cdot \begin{pmatrix} 1 & 0 & 0 \\ 0 & e^{i\alpha_2/2} & 0 \\ 0 & 0 & e^{i\alpha_3/2} \end{pmatrix} = \\
&\begin{pmatrix} 1 & 0 & 0 \\ 0 & c_{23} & s_{23} \\ 0 & -s_{23} & c_{23} \end{pmatrix} \begin{pmatrix} c_{13} & 0 & s_{13}e^{-i\delta} \\ 0 & 1 & 0 \\ -s_{13}e^{-i\delta} & 0 & c_{13} \end{pmatrix} \begin{pmatrix} c_{12} & s_{12} & 0 \\ -s_{12} & c_{12} & 0 \\ 0 & 0 & 1 \end{pmatrix} \\
&\cdot \begin{pmatrix} 1 & 0 & 0 \\ 0 & e^{i\alpha_2/2} & 0 \\ 0 & 0 & e^{i\alpha_3/2} \end{pmatrix} \quad , \quad c_{ij} = \cos\theta_{ij} \quad , \quad s_{ij} = \sin\theta_{ij}
\end{aligned} \tag{1.16}
$$

The mixing is a function of three *mixing angles* ($\theta_{12} \sim 34°$, $\theta_{23} \sim 9°$ and $\theta_{13} \sim 34°$). The phase factors α_2 and α_3 are non-zero only if neutrinos are Majorana particles[3] and do not enter into oscillation phenomena regardless. The phase factor δ is nonzero only if neutrino oscillation violates the CP symmetry.

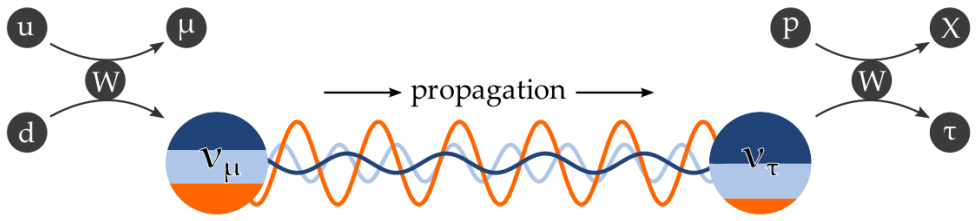

Figure 1.9: Schematic depiction of the neutrino oscillation mechanism. Neutrino interactions are governed by the flavor state, while the mass eigenstates propagate. [Sebastian Euler, "Observation of oscillations of atmospheric neutrinos with the IceCube Neutrino Observatory." Aachen: RWTH Aachen University, (2014).]

After travelling a distance L (or, equivalently for relativistic neutrinos, a time

[3]Majorana particle, is a fermion that is its own antiparticle. They were hypothesised by Ettore Majorana in 1937. The term is sometimes used in opposition to a Dirac fermion, which describes fermions that are not their own antiparticles.

t), a neutrino originally produced with flavour α evolves as follows[28]:

$$\nu_i(t)\rangle = ^{-\imath(E_i t - \vec{p}_i \cdot \vec{x})} \, |\nu_i(0)\rangle \tag{1.17}$$

In the ultra-relativistic limit ($|\vec{p}_i| = p_i \gg m_i$) one can approximate the energy as:

$$E_i = \sqrt{p_i^2 + m_i^2} \simeq p_i + \frac{m_i^2}{2p_i} \approx E + \frac{m_i^2}{2E} \tag{1.18}$$

assuming $p_i \simeq p_j \equiv p \simeq E$. Using $t \simeq L$ and also dropping the phase factors, the wave function becomes:

$$|\nu_i(t \simeq L)\rangle = ^{-\imath m_i^2 \frac{L}{2E}} \, |\nu_i(0)\rangle \tag{1.19}$$

Considering this last relation, the probability that a neutrino originally of flavor α will later be observed as having flavor β is given by:

$$P_{\alpha\to\beta} = |\langle\nu_\beta|\nu_\alpha(t)\rangle|^2 = \left| \sum_i U^*_{\alpha i} U_{\beta i} e^{-\imath m_i^2 \frac{L}{2E}} \right|^2 \tag{1.20}$$

or in more convenient form:

$$P_{\alpha\to\beta} = \delta_{\alpha\beta} - 4\sum_{i>j} \Re\Big(U^*_{\alpha i} U_{\beta i} U_{\alpha j} U^*_{\beta j}\Big) \sin^2\left(\frac{\Delta m^2_{ij} L}{4E}\right) \tag{1.21}$$

$$+2\sum_{i>j} \Im\Big(U^*_{\alpha i} U_{\beta i} U_{\alpha j} U^*_{\beta j}\Big) \sin\left(\frac{\Delta m^2_{ij} L}{2E}\right) \tag{1.22}$$

where $\Delta m^2_{ij} \equiv m_i^2 - m_j^2$ with $i, j = 1, 2, 3$. Restoring c and $\hbar$ the *oscillation phase*, that is responsible for oscillation, is often written as[29]:

$$\Phi_{ij} = 1.27 \Delta m^2_{ij}[\mathrm{eV}^2] \, \frac{L[\mathrm{Km}]}{E[\mathrm{GeV}]} \tag{1.23}$$

where $L = ct \simeq t$ is the distance between the source of ν_α and the detector (i.e. the detection point of ν_β). The transition probability $P_{\alpha\to\beta}$ has an oscillatory behaviour, with *oscillation length*:

$$L^{\mathrm{osc}} = \frac{4\pi E}{\Delta m^2_{ij}}. \tag{1.24}$$

The transition amplitude is proportional to the elements present in the mixing matrix. Thus, in order to have oscillations, neutrinos must have different masses

($\Delta m^2_{ij} \neq 0$) and they must mix ($U_{\alpha i} U_{\beta i} \neq 0$), since flavor oscillation is due to interference between different mass eigenstates.

In order to be sensitive to a given value of Δm^2_{ij}, an experiment has to be set up with $E/L \simeq \Delta m^2_{ij}$ (where L is the source-detector distance, table 1.1). If $E/L \gg \Delta m^2_{ij} \Rightarrow L \ll L^{\text{osc}}$ the oscillation does not have time to give an appreciable effect because $\sin^2 x_{ij} \ll 1$. For $E/L \ll \Delta m^2_{ij}$ ($\Rightarrow L \gg L^{osc}$), the oscillating phase goes through many cycles before detection and, since in general neutrino beams are not monochromatic, the phase is averaged to $<\sin^2 \theta_{ij}> = 1/2$ and the oscillation pattern vanishes.

Experiment	**L [m]**	**E [MeV]**	**Δm^2 [eV^2]**
Solar	10^{11}	1	10^{-11}
Atmospheric	$10^4 - 10^7$	$10^2 - 10^5$	$10^{-1} - 10^{-4}$
Reactor	$10^2 - 10^6$	1	$10^{-2} - 10^{-3}$
Accelerator	10^2	$10^3 - 10^4$	$\gtrsim 0.1$
Long Baseline Accelerator	$10^5 - 10^6$	10^4	$10^{-2} - 10^{-3}$

Table 1.1: Characteristic values of L and E for various neutrino sources and experiments.

For a two neutrino case, the mixing matrix depends on a single parameter θ and there is a single mass-squared difference Δm^2.

$$U = \begin{pmatrix} \cos\theta & \sin\theta \\ -\sin\theta & \cos\theta \end{pmatrix} \Rightarrow P_{\alpha\to\beta} = \delta_{\alpha\beta} - (2\delta_{\alpha\beta} - 1)\sin^2 2\theta \sin^2\left(\frac{\Delta m^2 L}{4E}\right) \quad (1.25)$$

A schematic depiction of the neutrino oscillation mechanism is shown in figure 1.9, in which the muon neutrino (ν_μ) has oscillated into a tau neutrino (ν_τ), producing a tau lepton in the final interaction [30]. Neutrino oscillation is important in determining the flavour ratio of neutrinos expected from various production scenarios as discussed in section 1.1.3.

1.3 IceCube Neutrino Science

As discussed above, neutrino telescopes, such as IceCube are motivated by the search for astrophysical neutrinos. However, IceCube's scientific portfolio is diverse and extends beyond astrophysical neutrinos. The threshold neutrino detection energy of IceCube is of the order $O(10)$ GeV which allows the detection of atmospheric neutrinos over a wide energy range, and also allows IceCube to be sensitive to

neutrinos produced in various dark matter annihilation scenarios. In this section some of the neutrino types which are sought by IceCube are discussed, beginning with a summary of some of the key astrophysical neutrino results from IceCube.

1.3.1 (High energy) Astrophysical neutrinos

As discussed above, high-energy neutrinos are expected to be produced in the interactions of cosmic rays close to the cosmic-ray acceleration site. These neutrinos are often referred to as high-energy astrophysical or cosmic neutrinos. The first evidence for astrophysical neutrinos was announced in 2013 by IceCube. A neutrino filtering strategy called HESE (High Energy Starting Event) was used where neutrino candidates were selected by finding events that originated within the detector interior. The HESE criteria for keeping an event was that at least 6000 p.e. had to be recorded in total and fewer than three of its first 250 observed p.e. where the veto region was defined to be the outer parts of the instrumented volume. This event selection rejects 99.999% of the muon background above 6000 p.e. while retaining nearly all neutrino events interacting within the fiducial volume at energies above a few hundred TeV.

This filtering strategy resulted in the discovery of 28 neutrino candidate events within the first initial two years search. It also provided evidence for the presence of an astrophysical flux of neutrinos events above the atmospheric background at 4σ [31]. By adding the third year data then resulted to a total of 37 events where the atmospheric explanation could be rejected at 5.7σ [32]. Most recently the 7.5 year HESE sample was released [33], with a total of 102 neutrino events. The best fit to the power spectrum of astrophysical neutrinos from the most recent sample is $\frac{d\Phi_{\nu+\bar{\nu}}}{dE} = \Phi\left(\frac{E_\nu}{100\ \mathrm{TeV}}\right)^{-\gamma} \cdot 10^{-18}$ [$\mathrm{GeV}^{-1}\mathrm{cm}^{-2}\mathrm{s}^{-1}\mathrm{sr}^{-1}$], the best fit spectral index γ is $2.89^{+0.20}_{-0.19}$ with an all-flavour flux normalization Φ of $6.45^{+1.46}_{-0.46}$.

Shortly after their discovery with the HESE filtering strategy, the presence of high energy astrophysical neutrinos events was confirmed by IceCube in the complementary channel of through-going and starting muons coming from the Northern Hemisphere where the atmospheric muon background is suppressed [34, 35]. The IceCube through-going track sample has now been updated to use nearly 10 years of data from May 2009 to December 2018 [36]. The best fit single power law spectral index is $2.28^{+0.08}_{-0.09}$, and the best fit single flavour flux normalization is $1.44^{+0.25}_{-0.24} \cdot 10^{-18}$ [$\mathrm{GeV}^{-1}\mathrm{cm}^{-2}\mathrm{s}^{-1}\mathrm{sr}^{-1}$].

To aid in the identification of neutrinos with astrophysical sources, IceCube has established an international collaboration with other astronomical messenger detectors, through a system of real-time alerts that rapidly notify the astronomical

community of the direction of astrophysical neutrino candidates [37].

This joint programme became operational in April 2016. In September 2017, the Fermi and MAGIC gamma ray telescopes followed up an IceCube alert of a high-energy neutrino event (labelled IC170922A) and found that it was consistent in direction with the blazar TXS 0506-056 which moreover, was observed to be in a flaring state[38]. Due to large number of blazar objects a positional coincidence has a reasonably high probability, however the fact that the blazar was in a flaring state added significance to the association. The chance coincidence of the IceCube 170922A event with the flare of TXS 0506+056 is statistically disfavored at the level of 3σ[38] . Furthermore in a subsequent analysis an excess of high-energy neutrino events with respect to atmospheric backgrounds was found at the position of TXS 0506-056 between September 2014 and March 2015[39] . Allowing for a time-variable flux, this constitutes 3.5σ evidence for neutrino emission from the direction of TXS 0506+056, independent of and prior to the 2017 flaring episode, and suggests that blazars are the first identifiable source contribution to the high-energy astrophysical neutrino flux[39].

1.3.2 (Low energy) Astrophysical neutrinos

Neutrinos with lower energy range can be also produced in some astrophysical sources. The typical energy range of these low-energy neutrinos is from a few MeV up to TeV. The sources where this type of low-energy astrophysical neutrinos are produced include core-collapse supernova and dark matter annihilation.

- **Core-collapse supernovae**

  When a massive star reaches the end of its life-time, core-collapse occurs and most of its gravitational energy is emitted as MeV neutrinos. Core-collapse supernovae which are dramatic explosions of giant stars at the end of their thermo-nuclear evolution give birth to either neutron stars or black holes. They are amongst the most energetic phenomena in the universe and play a key role in the formation and spreading of the chemical elements as well as triggering the formation of new stars.

  As the core collapses, protons are transformed into neutrons through multiple physical processes. The simplest process is inverse-β decay, wherein a proton combines with an electron to become a neutron. In addition to forming a neutron, a neutrino is also emitted. The only means to get direct and immediate information about the supernova "engine" is from observations of neutrinos emitted by the forming neutron star, and through gravitational waves which

are emitted when the collapse does not proceed perfectly symmetrically because of rotation, violent turbulent mass motions, and anisotropic neutrino emission. Individual galactic supernova (SN) neutrinos cannot be detected by IceCube as their energy, similar to that of solar neutrinos, is well below IceCube threshold. However a galactic supernova would produce so many neutrinos that there would be enough simultaneous SN neutrino interactions for a uniform rise in photomultiplier rates across the whole detector to be observed.

- **Dark Matter**

  A range of observational evidence suggest that between 85% up to 90% of the universe is composed of a strange substance known as "dark matter" which is hypothesised to be massive non-luminous particles. The Weakly Interacting Massive Particle (WIMP) is a common class of dark matter candidate. The mass-energy range of the WIMPs is between 10 GeV and 10 TeV. It is assumed that they interact only weakly. Depending on their cross section for interaction WIMPs can be captured in gravitational potential wells of massive astronomical objects like our Sun. This increases the annihilation rate of the WIMPs which will result in the production of other elementary particles including neutrinos. The energy of the neutrinos produced is related to the WIMP mass. The WIMPs' mass range indicates that the energy of the neutrinos produced should be intermediate in range between the energies of cosmic neutrinos and solar neutrinos [40].

1.3.3 Atmospheric neutrinos

As discussed in 1.1, when cosmic rays enter the Earth's atmosphere, their interactions produce neutrinos. Atmospheric neutrinos are typically produced around 15 kilometres above the Earth's surface. Figure 1.10 is a cartoon image showing a cosmic ray interacting with an air nucleus in the atmosphere, producing atmospheric neutrinos. These interactions in our atmosphere, result in a cascade of particles. The interaction of the cosmic rays produce mesons, such as pions and kaons which then quickly decay into either muons and muon anti-neutrinos or anti-muons and muon neutrinos. These are essentially the same processes described by equations 1.9 to 1.12 in the context of cosmic rays interacting near their source. As also mentioned in that context, muons and anti-muons are unstable particles and if they don't interact or lose energy in interactions, will decay into an electron, electron anti-neutrino and muon neutrino.

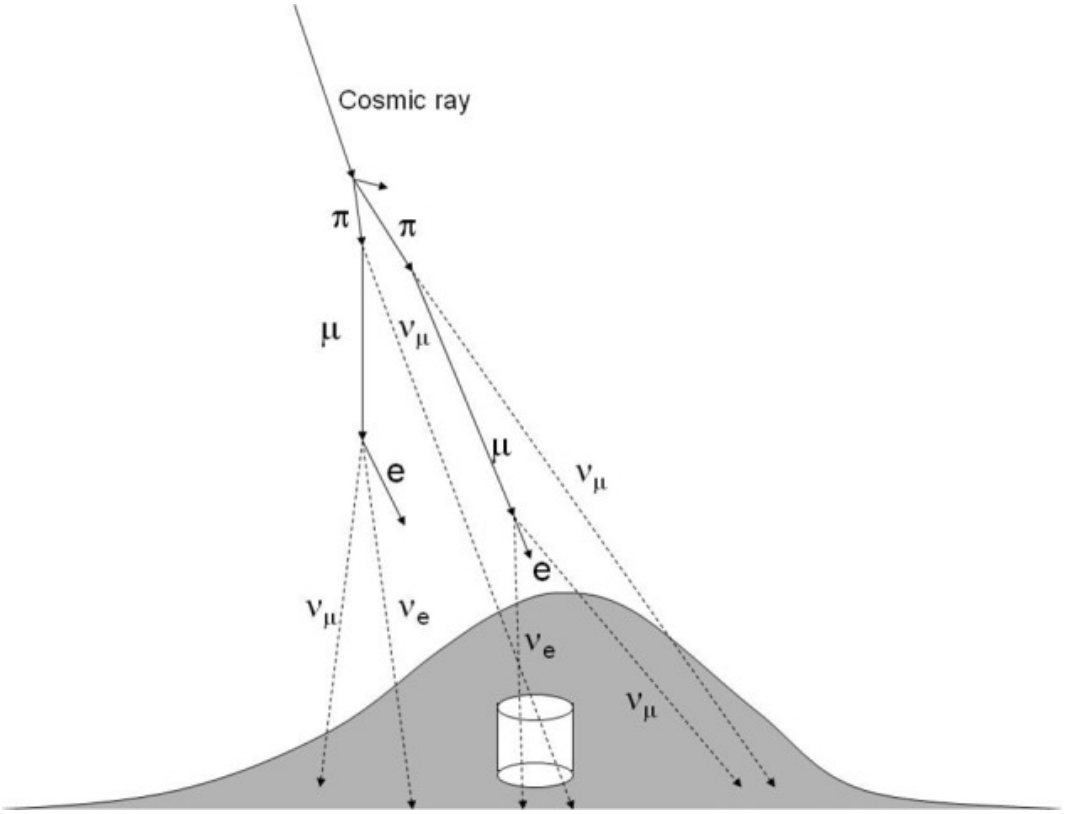

Figure 1.10: Production of neutrinos by cosmic-ray interactions with the air nucleus in the atmosphere. [Takaaki Kajita in the Proceedings of the Japan Academy, Series B, Physical and Biological Sciences (10.2183/pjab.86.303)]

A difference in the Earth's atmosphere, however, is that higher energy muons can reach the ground before decaying which results in the flavour ratio being different for atmospheric neutrinos compared to astrophysical neutrinos. Electron and muon neutrinos are produced mainly from the decay of pions, kaons, and muons. For energies less than a few GeV the fraction of muon neutrinos to electron neutrinos from these decay chains is about $\nu_\mu : \nu_e = 2 : 1$. But when energies increase, since high-energy muons have the chance to reach the surface of the Earth before decaying, this ratio increase. At energies above $E_K = 850$ GeV and $E_\pi = 115$ GeV for the kaons and pions respectively, the probability of mesons to decay is less than their interaction probability[41]. The atmospheric neutrino fluxes for muon and electron neutrinos and anti-neutrinos is shown in 1.11[4] As it can be seen for energies below

[4]This figure comes from a paper comparing the fluxes produced with the DPMJET-III Monte Carlo event generator[42, 43] with those from other event generators[44, 45]. DPMJET-III allows the simulation of hadron-hadron, hadron-nucleus, nucleus-nucleus, photon-hadron, photon-photon and photon-nucleus interactions from a few GeV up to the highest cosmic ray energies. The details of the event generators are not of particular interest here where the purpose of displaying the figure was to show the energy flavour ratio and its energy dependence.

100 GeV the ratio $(\nu_\mu+\overline{\nu}_\mu)/(\nu_e+\overline{\nu}_e)$ remains constant and climbs for higher energies.

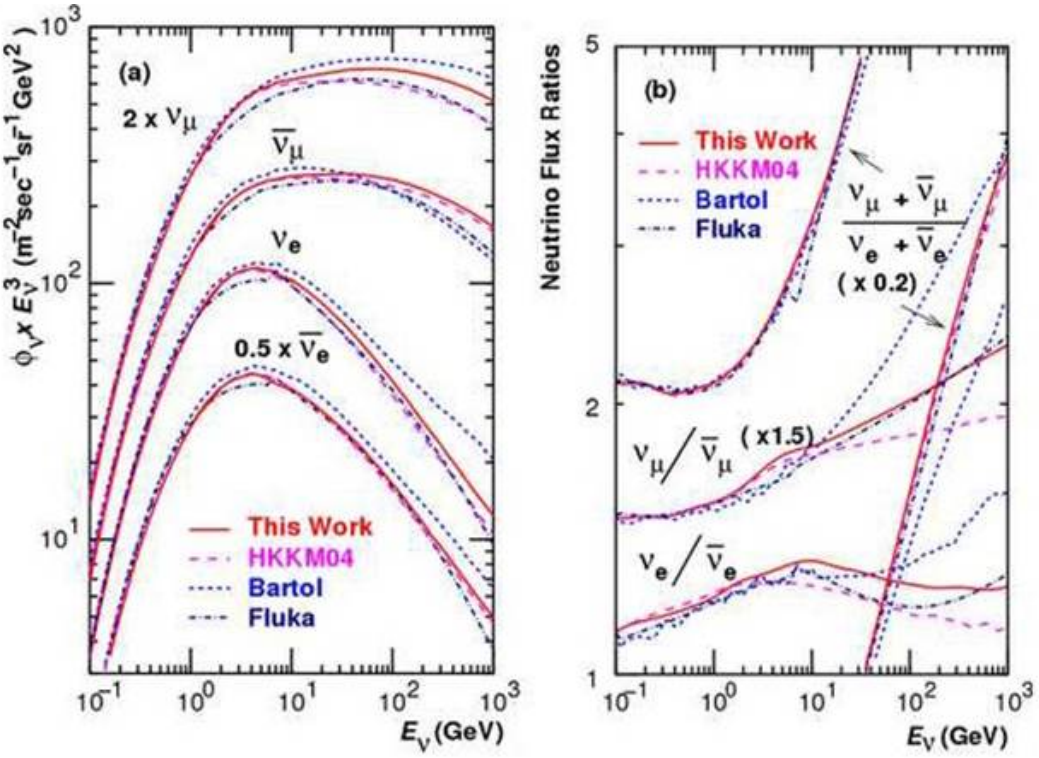

Figure 1.11: The comparison of all direction average of the atmospheric neutrino fluxes with other calculations; (left) the absolute values of each kind of neutrinos and (right) the ratio of them up to 1 TeV. [Figure from [43].]

IceCube detects atmospheric muon neutrinos above 100 GeV at a rate of over 100 000 per year. While these are an unwanted background as far as the search for astrophysical neutrinos is concerned, IceCube has various physics studies utilising atmospheric neutrinos. This includes neutrino oscillations and tau appearance [46, 47], neutrino mass ordering investigations [48], neutrino interaction cross-section studies[5], seasonal variations[49] and searches for sterile neutrinos[50].

1.4 Neutrino Observation

High-energy neutrino detectors exploit the fact that Cherenkov radiation is produced by the charged particles created when a neutrino interacts. The largest of the Cherenkov neutrino telescopes is IceCube, the detector of interest for this thesis. IceCube is described in detail in the next chapter. In this section, I will firstly present some of the key characteristics of Cherenkov radiation and give an overview of some of the past, and present, Cherenkov neutrino telescopes.

1.4.1 Cherenkov radiation

If a charged particle travels faster than the local speed of light in a given medium it emits radiation, peaked in the visible, called Cherenkov radiation [51]. There is always an angle between the direction of the produced Cherenkov light and of the path of the moving particle and the value of this angle depends on the medium [52].

The local speed of light in a medium is:

$$c_n = \frac{c}{n(\lambda)}, \tag{1.26}$$

where c is the speed of light in vacuum and n is the refractive index of the medium which is wavelength dependent. The Cherenkov angle θ_c is

$$\theta_c = \frac{1}{n(\lambda)\beta}, \tag{1.27}$$

with $\beta = \frac{v}{c} \approx 1$ for speeds close to the speed of light in vacuum.

As the secondary charged particle moves in the medium, its speed decreases. Consequently the number of Cherenkov photon produced declines while the Cherenkov angle increases and Cherenkov radiation stops being emitted when $v < c_n$ [53].

Since the Cherenkov spectrum is peaked at visible wavelengths (300 nm – 610 nm), Cherenkov radiation can be easily detected in a transparent medium such as ice or ocean water [54].

The Cherenkov radiation emitted per unit distance along the path of the particle is

$$\left(\frac{dE}{dx}\right)_{rad} = \frac{(ze)^2}{c^2} \int_{\epsilon(\omega) \geq \frac{1}{\beta^2}} \left(1 - \frac{1}{\beta^2 \epsilon(\omega)}\right) \omega d\omega, \tag{1.28}$$

where ze is the charge of the particle and $\epsilon(\omega)$ is the dielectric constant of the medium as a function of particles frequency, (ω). Cherenkov radiation is emitted in bands where $\epsilon(\omega) \geq \beta^2$. This condition indicates that the speed of the particle should be greater than the phase velocity of the electromagnetic field [55]. For energies between 10 GeV and 50 GeV the number of optical photons expected due to Cherenkov radiation is approximately 500 photons per centimetre. The produced photons of Cherenkov radiation experience either scattering or absorption in the medium. Therefore, having an extensive knowledge of the scattering and absorption properties of the medium is a key factor for any neutrino detection process. I will go in to more details about these properties in the following chapters.

1.4.2 Overview of Neutrino Cherenkov Detectors

While the extremely weak interaction properties of neutrinos makes them unique cosmic messengers, their low interaction rate means that a cubic kilometre detector is

required to study astrophysical neutrinos. The majority of high-energy neutrino detectors aim to detect optical Cherenkov light, and surround or embed a transparent medium, such as water or ice, with optical detectors. Although large underground tanks of water are used to detect solar and atmospheric neutrinos, the lower flux of astrophysical neutrinos necessitates the use of natural water sources in lakes, oceans or glacial ice for the study of cosmic neutrinos.

One of the largest neutrino detectors to employ an underground water tank is Super-Kamiokande. It is located 1000 m underground under Mount Ikneo in the Kamioka-mine, Hida-city, Gifu, Japan. Super-Kamiokande consists of a stainless-steel tank that is 41.4 m tall and 39.3 m in diameter holding 50,000 tons of ultra-pure water. About 13,000 photo-multipliers are installed on the tank wall. Super-Kamiokande, operational since 1996, was preceded by the Kamiokande neutrino detector and now the construction of a larger detector, Hyper-Kamiokande is underway. Hyper-Kamiokande will be 10 times larger than its predecessor and it is expected to start observation in 2025 [56].

The focus of Super-Kamiokande is the determination of neutrino properties through the observation of solar neutrinos, atmospheric neutrinos and man-made neutrinos. In 1998, from the observation of atmospheric neutrinos, the Super-Kamiokande Collaboration announced the first evidence of neutrino oscillation. In 2001, solar neutrino oscillations were observed and in 2011, the third neutrino oscillation mode was discovered by through the observation of accelerator neutrinos.In August 2020, the rare earth element gadolinium was introduced into the Super-Kamiokande detector, to allow the separation of neutrinos and antineutrinos in order to gain sensitivity to the diffuse background of supernova neutrinos.

As already mentioned, the detector volume needed to observe high-energy astrophysical neutrinos necessitates the use of a natural medium rather than an underground tank. Options utilised are ocean or lake water or glacial ice. A key feature of ocean water is its low diffusion which aids in estimating the neutrino direction more precisely and consequently allows a better possibility for the discovery of their sources. It is advantageous to have detectors in both the Northern and Southern hemispheres in order to cover the sky using the through-going event filtering strategy.

The first detector which was built in the ocean was called DUMAND. It was launched in 1976 in the Pacific ocean, near Hawaii, around 5000 m beneath the surface. However, the project was canceled in 1995 due to some technical difficulties [57]. In 1993, the construction of another Cherenkov detector below the surface of Lake Baikal (in Russia) was started. This project is called the Baikal

Deep or BDUNT (Baikal Deep Underwater Neutrino Telescope). This detector was completed in 1998 and was upgraded in 2005. It is the oldest operating neutrino telescope on Earth [58] and is one of the three largest operational neutrino detectors in the world along with IceCube and ANTARES in the Mediterranean Sea.

The upgraded generation of Baikal neutrino telescope which is called Baikal-GVD – Gigaton Volume Detector, will be about 50% larger than the current IceCube detector. The preparatory phase of the project was concluded in 2015 with the deployment of a demonstration cluster comprising 192 optical modules. The construction of the first phase of Baikal GVD (GVD-I) was started in 2016 by deploying the first of eight clusters in their baseline configuration, consisting of 288 optical modules. Completion of GVD-I (8 clusters, volume 0.4 km^3) is planned for 2021.

Soon after the Baikal telescope three more under water Cherenkov detectors were proposed and started operation in the Mediterranean Sea: NESTOR (3800 m depth), ANTARES (300m depth) and NEMO respectively [59]. These 3 detectors provided valuable experience for scientists in the design of KM3NeT (Cubic Kilometre Neutrino Telescope). Km3Net is a European research infrastructure with a planned instrumented volume of about five cubic kilometres. KM3NeT will act as counterpart to IceCube in the Northern hemisphere, with a sensitivity substantially planned to exceed all existing neutrino telescopes including IceCube[60].

The alternative natural medium to lake or ocean water which has been used for neutrino detection is polar ice. Unlike ocean water, ice is free of bioluminescent organisms and natural radioactive isotopes. Other advantages are that the ice possesses a rigid structure for the deployment of instrumentation, thermal noise is very low, and the size, and number of air bubbles, decreases with increasing depth[61].

The first ice Cherenkov detector was the Antarctic Muon And Neutrino Detector Array or AMANDA which was the predecessor to IceCube and also located beneath the Amundsen-Scott South Pole Station. The prototype, AMANDA-A was constructed between 800-1000 m beneath the surface. However subsequent phases of the detector, AMANDA-B & AMANDA-II, were deployed deeper in the ice (1500-1900 m) due to the fact that air bubbles disappear below 1300m due to the pressure of the bulk ice above. The AMANDA detector was decommissioned in 2009 when IceCube was fully operational. IceCube is described in the next chapter

At ultra-high energies it becomes advantageous to detect radio rather than optical Cherenkov radiation. The emission of radio wavelength radiation from particle showers is known as the Askaryan effect and was predicted by the Soviet-Armenian physicist physicist Gurgen Askaryan[62, 63]. The cascade of secondary charged

particles, emitted when a particle such as a neutrino interacts, contain a charge anisotropy and emits a cone of coherent radiation in the radio or microwave part of the electromagnetic spectrum. A number of neutrino detectors have operated or are planned with an array of radio receivers or with atmospheric balloons carrying radio receivers. A review of these detectors is provided in[64].

For neutrinos above 100 PeV the detector which currently has the highest sensitivity is the Pierre Auger Observatory (PAO)[65]. The Pierre Auger observatory is principally a cosmic-ray detector with an array of Cherenkov water tanks and fluorescence telescopes on the surface near the Andes in Argentina. The array observes cosmic rays through detecting the air shower particles created when cosmic rays interact in the atmosphere. The interaction of neutrinos produces similar air showers which can also be detected. To separate neutrino induced showers from cosmic-ray induced showers, PAO looks for showers from directions close to the horizon or through the Andes, as cosmic rays interact higher in the atmosphere than neutrinos, and cosmic-ray air showers could not reach the detector from these directions.

2 IceCube Neutrino Observatory

The IceCube Neutrino Observatory, located at the South Pole, is the largest volume neutrino telescope currently operating. It includes three components: a cubic kilometre *InIce* Cherenkov detector, a more densely instrumented infill subarray, DeepCore, and the IceTop surface array. Construction of the telescope started in 2004 and continued over the Antarctic austral summers (November to February) each year for the following six years. The InIce array was completed in 2010. In figure 2.1 a side-view of the IceCube neutrino observatory can be seen, including IceTop array, DeepCore and InIce.

In this chapter I will describe the IceCube detector, particularly concentrating on the InIce array and its instrumentation, and the techniques used for detecting neutrinos.

2.1 Detector Components

2.1.1 InIce

The IceCube *InIce* component consists of 86 strings, each with 60 spherical optical sensors attached. The optical sensors are refered to as Digital Optical Modules (DOMs) and each DOM has a PhotoMultiplier Tube (PMT). The strings are embedded vertically within a hexagonal footprint on a triangular grid with 125 m horizontal spacing and the optical sensors are deployed at depths between 1450-2450 m, spaced 17 m apart vertically along those strings[66]. The InIce component is the array optimised for detecting astrophysical neutrinos.

2.1.1.1 DeepCore

DeepCore is located in the bottom region of IceCube, starting at a depth of 2100 m. It consists of 8 additional strings each holding 50 DOMs with 7 m spacing between each DOM which makes DeepCore a denser array than the rest of IceCube. The surrounding IceCube detector can be used as an efficient veto for DeepCore by removing muon backgrounds.

The corresponding PMTs use upgraded photocathodes with a quantum efficiency

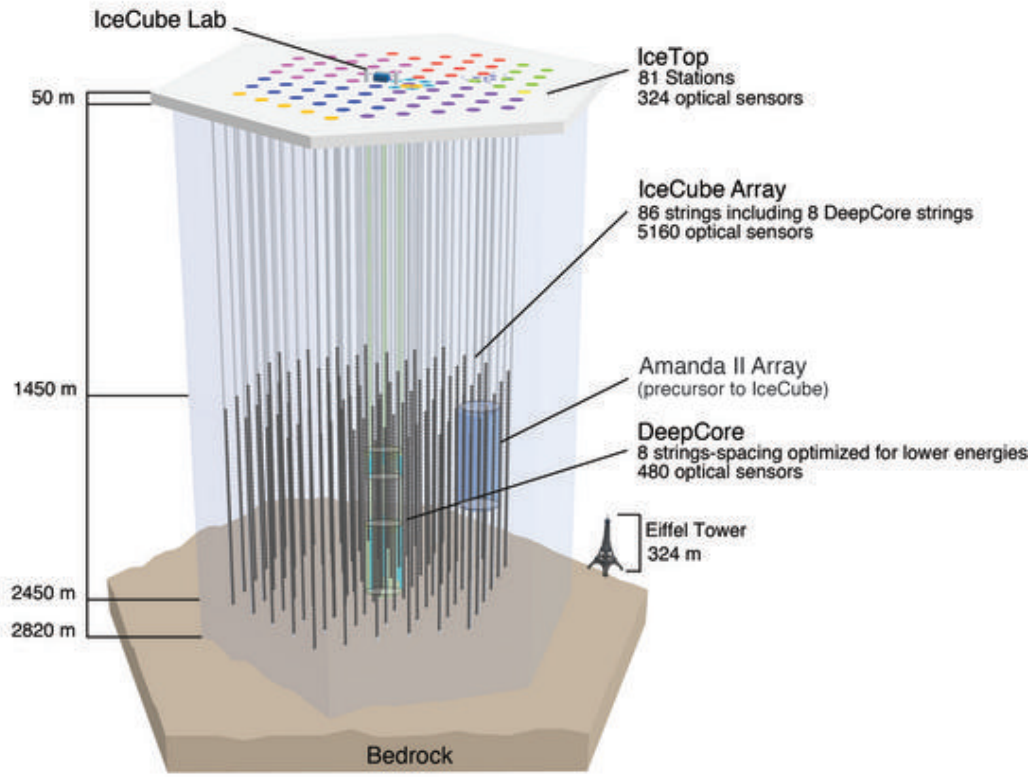

Figure 2.1: The IceCube detector instrumented between 1450 m and 2450 m in the ice at the South Pole, with the Eiffel Tower shown for size perspective. The observatory includes a densely instrumented subdetector, DeepCore, and a surface air shower array, IceTop. [Image via Felipe Pedreros, IceCube/NSF.]

about 35% higher than the rest of the PMTs in IceCube. This special feature along with the fact that the ice is extremely clear at those depths can increase the sensitivity of IceCube to all neutrinos. The denser geometry and higher efficiency result in a lower energy threshold of about 10 GeV, compared to about 100 GeV for most IceCube analyses. This lower energy threshold that DeepCpre provides is important for the atmospheric neutrino oscillation studies, indirect searches for WIMP dark matter and the detection of Galactic supernovae[67]. Figure 2.2 shows the vertical strings and the spacing between the DOMs on each string. Note that unlike the strings in the so called InIce part of the detector where all the DOMs are positioned evenly and with a constant spacing, DOMs on the DeepCore strings are deployed in two separate depth ranges; one from 1750 m to 1860 m with 10 m spacing between each DOM, and one from 2107 m to 2450 m,that is the bottom of the detector, with 7 m DOM Spacing.

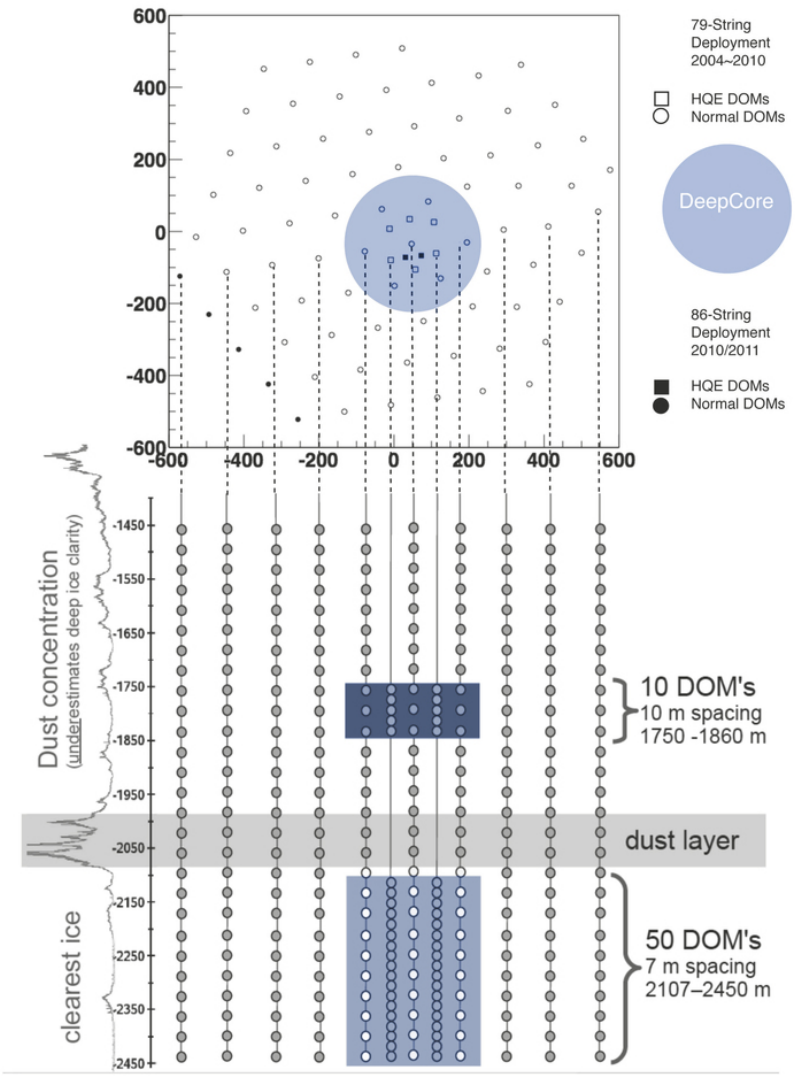

Figure 2.2: Geometry of the DeepCore Detector. The top part shows the surface projection of horizontal string positions and indicates the position of DeepCore. The bottom part indicates the depth of sensor positions. At the left the depth-profile of the optical transparency of the ice is shown. [Chang Hyon Ha, D. Jason Koskinen. "Observation of Atmospheric Neutrino-induced Cascades in IceCube with DeepCore", 2011

2.1.2 IceTop

IceTop is located on the surface of the ice at 2835 m above sea level. It consists of 81 stations situated above each string on top. Each station has two tanks so that the total number is 162. The horizontal distance between the two tanks at each surface station is approximately 10 m. Each tank is filled with ice to a height of

0.9 m and accommodates two DOMs which the detect Cherenkov radiation from air shower particles. One of the DOMs in each tank is a "high-gain" DOM with a PMT gain of 5×10^6 and the other DOM is a "low-gain" DOM that operates at a gain of 10^5 [69]. A denser infill array is formed by the eight stations in the center of IceTop, corresponding to the denser inter-string spacing in DeepCore. IceTop is sensitive to primary cosmic rays in the energy range of PeV to EeV with an energy resolution of 25% at 2 PeV, improving to 12% above 10 PeV [68]. The energy range of IceCube as a cosmic-ray detector fully covers the "knee" region of the spectrum and extends to the energies where a transition from Galactic cosmic rays to a population of extra-galactic particles may occur. By deriving the correlation between the energy measured in IceTop and the energy deposited in the deep ice we can explore the cosmic rays in the energy range from about 100 TeV to 1 EeV. In addition, using single tank hits IceTop can be used to distinguish between high energy cosmic neutrinos and low energy neutrinos. It is also useful for the calibration of the in-ice detector[70] as well as partial vetoing for the detection of downward-going neutrinos.The energy range of IceCube as a cosmic-ray detector fully covers the "knee" region of the spectrum and extends to the energies where a transition from Galactic cosmic rays to a population of extra-galactic particles may occur.

2.2 Digital Optical Module

The Digital Optical Module or DOM is the main IceCube detecter unit which detects light through its photomultiplier tube (PMT). A DOM consist of a spherical glass housing containing a downward-facing PMT, its associated circuit board, the DOM's mainboard and a flasher board. Figure 2.3 shows these components. The DOM is the fundamental data acquisition unit for IceCube, as well as being able to act as a calibration device. The main characteristics required for a DOM include its stability and reliability in the harsh deployment environment, the ability to record a wide range of PMT pulse widths and amplitudes with nanosecond time resolution, and its long-term life time. While 55 DOMs died during deployment mostly due to cable damage, water leaks or freeze-in damage, only 32 DOMs out of 5105 remaining DOMs have failed after deployment. This indicates that overall the DOMs used in IceCube meet the above key requirements.

The optical signals that are received by the PMTs are digitized and sent to the IceCube Laboratory (ICL) on the surface above the detector via twisted copper-pair wires . The Data AcQuisition system (DAQ) has been designed to digitize and merge the collected pulses from the PMT of each individual DOM. At the ICL basic

filtering steps are applied to the data before the data is transferred to the Northern Hemisphere data repository.

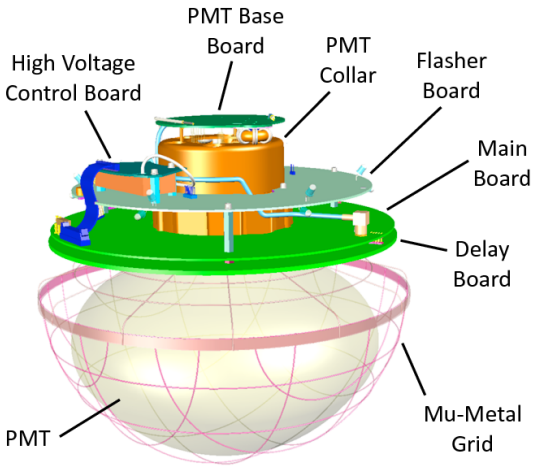

Figure 2.3: Schematic view of a DOM. [M. G. Aartsen et al. The IceCube Collaboration, "The IceCube Neutrino Observatory: Instrumentation and Online Systems", March (2017).]

A schematic view of a typical DOM as deployed inside the ice can be seen in figure 2.4 below. Both cable mechanical assembly as well as cable break-out can be seen in this figure.

Details for some of the key DOM elements are:

- **PMT, Gel and Magnetic Shield**

  Photomultiplier Tubes or PMTs are the detecting elements in the DOM. Through the electron avalanche process a PMT is able to eventually produce multiple electrons from the initial incident electron produced by the photo-electric effect of an incident photon. PMTs which are used in IceCube reach a gain factor of 10^6 meaning that one initial electron is multiplied to 10^6 final electrons at the end.

  The PMTs used in IceCube are $10-inch$ diameter $R7081-02$ produced by Hamamatsu Photonics, or the corresponding high quantum-efficiency (HQE) version, Hamamatsu $R7081-02MOD$, for DeepCore strings. The PMT is specified by Hamamatsu for the wavelength range 300 nm - 650 nm, with

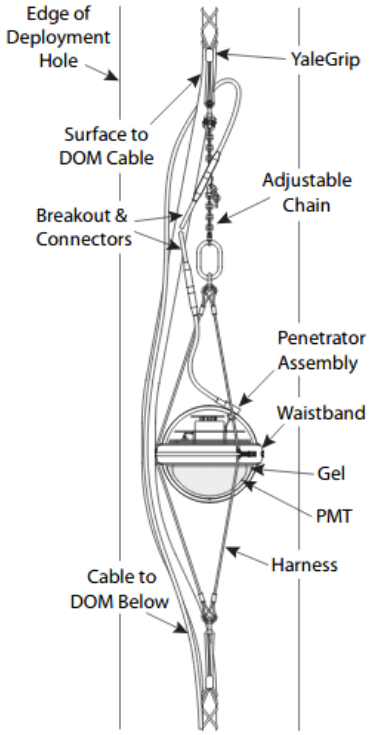

Figure 2.4: DOM cable assembly showing both the mechanical assembly as well as the cable break-out. [M. G. Aartsen et al. The IceCube Collaboration, "The IceCube Neutrino Observatory: Instrumentation and Online Systems", March (2017).]

peak quantum efficiency around 25% (34% for HQE) near 390 nm [71]. A quantum efficiency of ∼25% with nominal gain of 10^7 means that there is 25% probability for an incident photon to hit free an electron.

As it can be seen in figure 2.3, the PMT bulb faces downwards in the bottom of digital module. It is surrounded by a high-strength silicone gel with approximately 1 cm thickness that can provide both mechanical support for the PMT and good optical coupling. The main characteristics of this silicone gel are: first, its optical clarity with transmission of 97% at 400 nm, 91% at 340 nm, and 65% at 300 nm; second, its refractive index (i.e: ∼1.41) which result to less than 0.1% light reflection; and third its stability in the temperature range $-70°$C to $+45°$C.

In addition, a mu-metal cage surrounds the PMT bulb up to the neck to reduce the effects of the ambient South-Pole magnetic field (i.e: (550 mG, 17° from vertical). Although this mu-metal cage blocks about 4% of the incident light, it increases the collection efficiency by 5% to 10% in addition to enhancing the single photo-electron resolution [72]. While the PMT and its positioning in a typical DOM is shown in figure 2.3, a diagram of the functional connections

of PMT and other components of a DOM is depicted in figure 2.5.

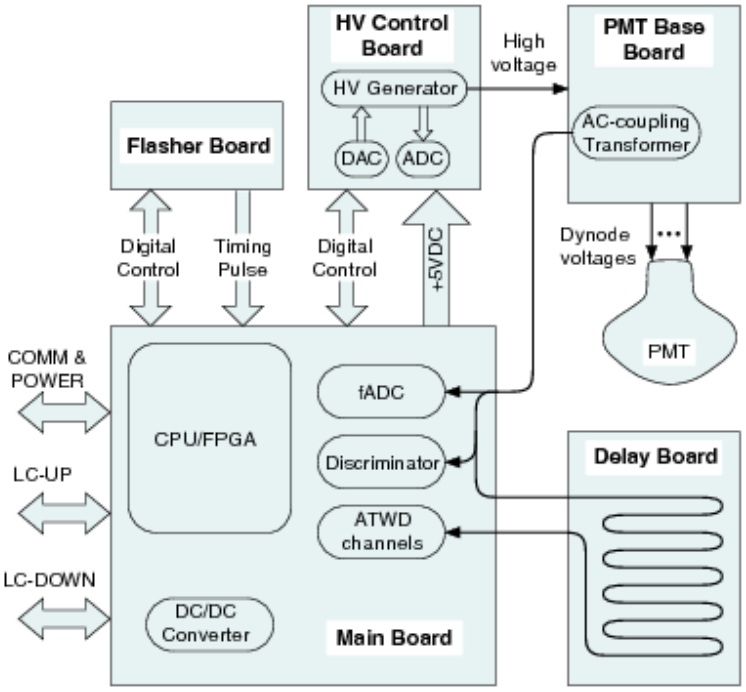

Figure 2.5: Diagram of the functional connections of PMT and other components of a DOM. [M. G. Aartsen et al. The IceCube Collaboration, "The IceCube Neutrino Observatory: Instrumentation and Online Systems", March (2017).]

- **Mainboard**

  The mainboard circuit is fitted around the neck of the PMT and integrates the data acquisition, control, calibration, communication, and low-voltage power conversion. The DOM mainboard contains all of the electronics to amplify and digitize the signals of the PMT. The DOM mainboard is connected to the surface by a single twisted pair cable which carries power, communications and timing signals. The mainboard provides many key functions for them, including:

  - **Control of all the devices inside the DOM;** This includes supplying high voltage power for the PMT, the flasher board, etc as well as providing necessary DC power to the sub-systems.
  - **Digitization of the PMT waveforms;** This is done by feeding the PMT output signal to an integrated circuit called *ATWD (Analog Transient Waveform Digitizer)* and then to a *Fast Analog to Digital Converter (FADC)* [73].

– **Providing computational functions;** This includes PMT gain calibration, compressing digitized waveforms, temporarily storing the data, and creating time-stamped data packets.

- **Flasherboard**

  The flasher board is used to generate in-situ light for several purposes like calibration, measuring the ice properties and the positions of DOMs in the ice. There are two types of flasher board in IceCube, the standard board, and the multi-wavelength board. Most of the flasher boards are standard and are fitted with 12 LEDs with the output wavelength of 405± 5nm.

  These LEDs are arranged in six pairs which are positioned on the flasher board with 60 degree separation between each pair. One LED in each pair is called the horizontal LED although it is actually pointed downward at an angle of 10.7°. However, the outgoing light emits horizontally from the DOM's sphere because of its refraction through the DOM glass. The other LED in each pair is tilted upward at an angle of 51.6° exiting light upward at an angle of 48°. This angle has been chosen because it is very close to the Cherenkov angle in ice[74].

  The energy range from neutrino interaction showers is between 7 GeV and 1 PeV, therefore it is required to have DOMs with the capability of generating flashes from 10^6 to 1.4×10^{11} photons. This can be achieved by adjusting the brightness and width setting of LEDs, in addition to the number of operating LEDs at a given time.

  Figure 2.6 shows the flasher light time profile. By using a programmable delay we can adjust the width of the light pulse between 5 ns and 70 ns. The intensity is controlled via a variable voltage between 4.5 V and 14 V. The width of the light pulse are deduced from in-situ simulation to flasher data comparisons to be $\sim 1.2 \times 10^{10}$ photons per LED, whereas the maximum integral photon output is obtained at maximum brightness. The relative integral flasher output depends on the brightness setting B and width setting W and can be expressed as follow:

$$L = (0.0006753 + 0.000055593.B).(W + 13.9 - \frac{57.5}{1 + B/34.4}. \tag{2.1}$$

  The flasher brightness test cycles through all 12 LEDs on the flasher-board and ramps up the brightness control (over 10 different settings) while monitoring the amplitude of the current through the LED, by reading it out in an ATWD channel.

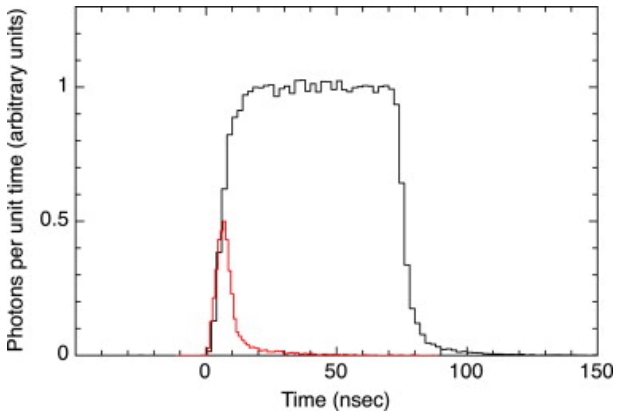

Figure 2.6: Flasher light output time profile for pulses of minimum and maximum width. The relative height of the short pulse has been scaled so the leading edges are comparable. This measurement was performed using a small PMT (Hamamatsu R1450) after optical attenuation of the pulses to facilitate counting of individual photons. [Aartsen et al., "Measurement of South Pole ice transparency with the IceCube LED calibration system".

2.3 Colour DOMs

In addition to the standard DOMs described above, IceCube also has 16 coloured DOMs or c-DOMS, each fitted with a multi-wavelength flasher board. Eight of them are deployed on string 79 which is in the centre of IceCube, and the remaining 8 are deployed on string 14 which is located on the edge of the detector. Just like a normal DOM, each colour DOM is also equipped with 12 LEDs which are arranged in six pairs. These LEDs which act as artificial in-situ light sources can be used for the calibration of the ice and the PMTs. Howeve, there are two main differences between normal DOMs and c-DOMs. First, unlike normal DOMs in which all LEDs have the same wavelength, each colour-DOM includes LEDs with four different wavelengths (505 nm, 450 nm, 370 nm, and 340 nm). Second, in c-DOM all LEDs point outward horizontally and unlike normal DOMs there is no tilted LED in cDOMs. The properties of the LEDs on the standard DOMs and the cDOMs are given in the table 2.1, including wavelength λ , emission FWHW σ in air, DOM polar angular emission FWHM in ice σ_θ , and DOM azimuthal angular emission FWHM in ice σ_ϕ.

The angular emission profile of each LED has a Gaussian component with a standard deviation of approximately 13°. About 10% of the light has been observed to be emitted outside the Gaussian beam. The light is refracted at the air-glass boundary as well as the ice-glass boundary, changing the emission angle and narrowing the

angular emission profile. In the case of standard LEDs which emit light at 405 nm the angular emission profile is narrowed to approximately 10°, whereas the angular emission profile for the other wavelength LEDs varies with wavelength. The angular emission profile for each wavelength LED can be seen in table 2.1. These profiles are used in the simulations described in Chapters 5 and 6.

A schematic view of a colour DOM's flasher board and the positions of LED pairs is displayed in figure 2.7.

LED	**nominal λ(nm)**	**measured λ(nm)**	**σ air**	σ_θ	σ_ϕ
ETG-5UV405-30	405	399	30.0	9.7(t)	9.8(t)
				9.2(h)	10.1(h)
UVTOP335-FW-TO39	340	338	51.0	36.1	42.9
NS370L_ 5RFS	370	371	55.2	39.1	42.9
LED450-01	450	447	6.8	4.8	5.3
B5-433-B505	505	494	6.4	4.5	4.9

Table 2.1: Properties of the standard IceCube flasher LED and the cDOM LEDs.

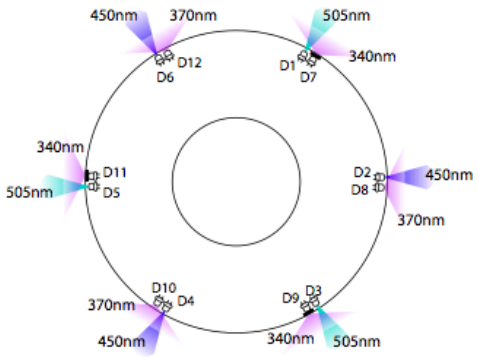

Figure 2.7: Positions of LED pairs on the flasher board of a colour DOM. [IceCube wiki page, "CDOM Info": `https://wiki.icecube.wisc.edu/index.php/CDOM_Info`, (2011).]

2.4 Calibration

In this section I will discuss some of the IceCube calibration procedures, particularly concentrating on those relevant to this thesis.

2.4.1 Geometry Calibration

Geometry calibration refers to determining the relative positions, and also orientation, of all DOMs accurately. The uncertainty in position is typically within one metre. The coordinate system which is used was developed when AMANDA first became operational. The origin of the AMANDA coordinate system, (0,0,0) was centered on the AMANDA array and was defined as the point in the ice where the physical location of DOM 70 (module 10 on string 4) was believed to be back in 1997. The origin of the IceCube coordinate system is located at $46500' E$, $52200' N$, at an elevation of 883.9 m. The x-axis is taken to be Grid East, the y-axis is Grid North (aligned with the Prime Meridian, pointing towards Greenwich), and the z axis is normal to the Earth's surface at the $x = 0, y = 0$ origin.

An overview of coordinates of important reference points of IceCube comparing to the global coordinates of those points can be seen in table 2.2 below.

	Global Coordinate	**IceCube coordinate**
Bedrock Depth	-2832 m	-830 m
IceCube String Depth	-2450 to -1450 m	500 to +500 m
DeepCore String Depth	-2450 to -2100 m	-500 to -150 m
Dust Layer Depth	-2100 to -2000 m	-150 to -50 m

Table 2.2: An overview of coordinates of important reference points.

Three different stages need to be done to obtain the x, y, z coordinates for all DOMs in the IceCube coordinate system. These stages are summarised below:

- Stage 1

  Unlike the collected data in IceCube which all are initiated from optical data received by PMTs of each DOM, the data that is used in stage one are non-optical data. These data sets are compiled during the string deployment and using a pre-deployment survey of the drill tower. The final product is a set of 3-dimensional coordinates for all DOMs (in-ice and IceTop) in the IceCube coordinate system. A schematic summary of the information which is used for this stage of geometry calibration is shown in figure 2.8.

- Stage 2

  At stage 2 we use optical data collected by each DOM to determine the relative depth offsets between the strings. The offsets between the strings that are

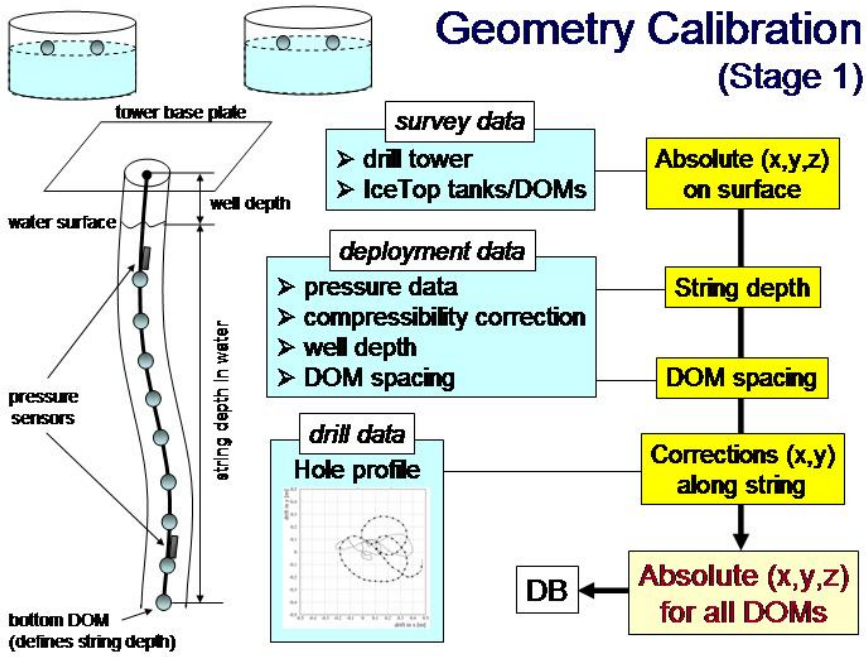

Figure 2.8: Summary of Stage 1 geometry techniques. [IceCube wiki page: "Stage 1 geometry", `https://wiki.icecube.wisc.edu/index.php/Stage_1_geometry`. (2011).]

determined at stage 2 are relative to the Stage 1 geometry. The optical data that is used in this stage is flasher-data taken using the flashers mentioned above. The flasher LEDs can be used as the in-situ light sources able to emit light at different wavelengths peaked at 5 specific wavelength numbers from 340 nm up to 505 nm. We can adjust these LEDs to either emit pulses individually, in a group or altogether at the same time depending on the objective of each study. PMTs in other DOMs receive the emitted pulses, digitize them and send them to the ICL at the surface of the IceCube.

For the stage 2 geometry calibration purposes, on a given flasher, only the six horizontal LEDs are flashed, and photon travel times are recorded at all receiving DOMs on adjacent strings. An example of a travel time distribution for a certain flasher-receiver combination is shown in figure 2.9. For each receiver DOM, a distribution of travel times (from the flasher to the receiver). More details including some examples are presented in section 4.1.

- Stage 3

  The Stage 3 geometry calibration uses muon tomography to track deformations of the array over time due to ice shear. It uses downgoing muons to determine the three dimensional position of each DOM. For the calibration of a given

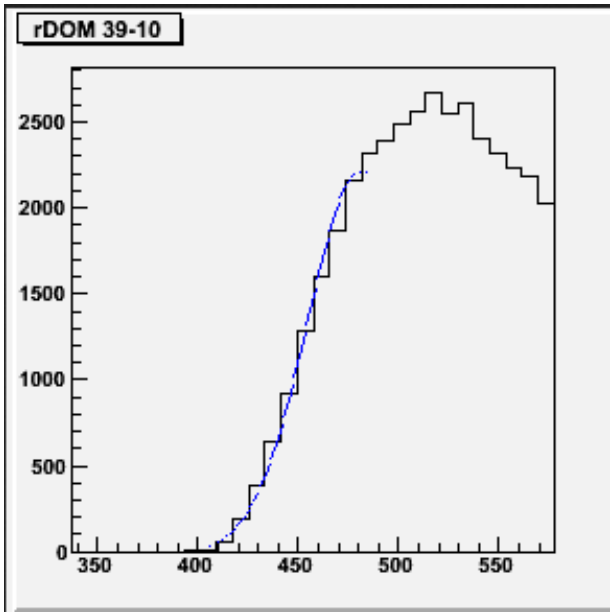

Figure 2.9: Time distribution at DOM 39-10 for the first photons coming from the all horizontal LEDs on DOM 39-15. [IceCube wiki page: "Stage 2 geometry", `https://wiki.icecube.wisc.edu/index.php/Stage_2_geometry`. (2011).]

DOM, high quality tracks are selected after reconstruction that excludes the DOM, but for events in which there is data from the DOM. A 3-dimensional map is then made of the DOM's contribution to the track likelihood as a function of (x, y, z). The point with the likelihood maximum is then the best-fit position of the DOM. Although there are a large statistics of high quality tracks available due to the massive number of downgoing muons, since the muon tomography depends on the track reconstruction, the output products always include some systematic errors.

Determining the orientations of all DOMs is also a part of *Geometry Calibration*. It is typically done by reconstructing the relative pointing of *LED* 7 on all DOMs. As a part of my research, I have used flasher data to determine the orientations of some DOMs on string 79. Those DOMs include a number of normal DOMs as well as all colour-DOMs on that string. The details of the method along with the analysis and the final results are presented in chapter 4.

2.4.2 Waveform Calibration and DOM calibration

Waveform calibration, which can also be referred to as charge calibration, consists of several steps taken to convert the raw digital waveform data to the number of photo-electrons *(nPE)* recorded by PMTs. Ideally, the nPE is given by the product

of the number of photons that hit the PMT times and the probability that a photon generates a pulse above threshold (which includes the PMT quantum efficiency and other effects).

The overall objective of the DOM Calibration is to have a consistent meaning for every measurement of a photo-electron as well as producing pulses that have similar relative time frames. This calibration which is basically a DOM-by-DOM calibration is done via a calibration software called "DOMCal". The PMT outputs are translated into voltage and time, where the PMT outputs are the digitized samples of the recorded waveforms, and the gain of the PMT into account. Since there are more than 5600 digitial modules deployed in the ice having a consistent and comprehensive calibration method is essential to the operation of IceCube. The main board of a DOM has all the necessary components needed for its calibration including a pulser circuit, a DC bias generator and a LED on the mainboard. Fortunately, since the operating conditions in the ice are close to stable, this calibration needs to be done only once per year. However, many calibration values are constantly being monitored during multiple runs over the year.

Further details for these calibration processes can be found in [75]

2.5 Neutrino detection with IceCube

IceCube detects neutrinos through the light produced by the products of a neutrino interacting in the ice or bedrock. Neutrino interactions were discussed in section 1.2.1 where NC and CC interactions were introduced. We recall that the products of a NC interaction are a neutrino and hadronic shower while in a CC interaction the charged lepton partner of the interacting neutrino is produced along with the hardronic shower. In this section I will discuss the event signatures which are seen in the IceCube detector for these interactions.

In a CC interaction there is Cherenkov light produced by the charged lepton. Different event topologies arise depending on the flavour of the neutrino. The CC event topologies are described below and shown in figure 2.10. In the event views shown in figure 2.10 each sphere is a single DOM; the coloured spheres show those that observed light from the event. The sizes show how many photons each module observed, while the colour gives some idea of the arrival time of the first photon, from red (earliest) to blue (latest).

– **Electron Neutrino CC Interaction**

  The outgoing electron from a CC interaction will produce an electromagnetic cascade containing electrons, positrons, and photons. Bremsstrahlung

and pair-production are the primary interactions within the electromagnetic cascade[76]. The total track length of this type of electromagnetic cascade is proportional to the energy of the cascade and consequently to the resulted electron neutrino from the CC interaction, for instance the corresponding length of a 100 TeV EM-Cascade has been estimated to be around 8.5 m[77].

– **Muon Neutrino CC Interaction**

In addition to the bremsstrahlung and pair-production energy loss processes which electrons undergo, muons also lose energy through ionization and multiple scattering. Moreover, a muon has a significantly smaller interaction cross-section than an electron due to its larger mass which means that a muon loses energy at a lower rate in comparison to the electron. For example, a 1 TeV muon travels approximately 3 km [77]. The muon energy loss rate as a function of path length can be expressed as

$$-\frac{dE}{dx} = a(E) + b(E)E, \tag{2.2}$$

where $a(E)$ is the energy loss from ionization, and $b(E)$ is the combined energy loss due to the radiative processes [77]. To the approximation that these slowly varying functions are constant the mean range of a muon x_0 with initial energy E_0 is

$$x_0 = \frac{1}{b}\, ln\left(1 + \frac{E_0}{E_{\mu c}}\right), \tag{2.3}$$

where $E_{\mu c} = a/b$ is the critical energy at which the ionization loss equals the energy loss due to other processes [76]. In ice a and b are largely independent of energy with $a = 0.2$ GeVm^{-1} and $b = 3.4 \times 10^{-4}$ m^{-1} [76]. Since a muon loses energy along its path, small local cascades can be produced along the track and such processes can slightly deflect the muon during its propagation until it loses all its kinetic energy.

– **Tau Neutrino CC Interaction**

In a CC ν_τ interaction, the outgoing tau will itself decay. Therefore, two cascades will be produced. The separation of the two cascades is determined by distance travelled by the tau which, in turn, is determined by the time dilation experienced by the tau and hence the energy of the tau. A sufficiently high energy tau can travel a short distance before decaying and consequently produce two distinguishable cascades with a faint track signature in between the two cascade. This distinguishable two cascade signatures can only happen

when the separation length, which can be expressed as $\sim$ 50 m per PeV, exceeds the experimental cascade vertex resolution. A 1 PeV tau, for instance, can travel around 50 metres before undergoing decay [77]. These two cascades of this type of event can either both contained within the detector or one within the detector and the other outside, which is called the double-bang event and the lollipop event respectively. For lower energies, it is difficult to distinguish the second cascade from the initial hadronic cascade and thus the tau is indistinguishable from a NC or ν_e CC signature.

In a NC interaction, as the outgoing lepton is a neutrino, the only observable product is the hadronic shower. The event topology for a neutral current event is a cascade type and is indistinguishable from that shown for the CC electron neutrino, and labelled as cascade, in 2.10.

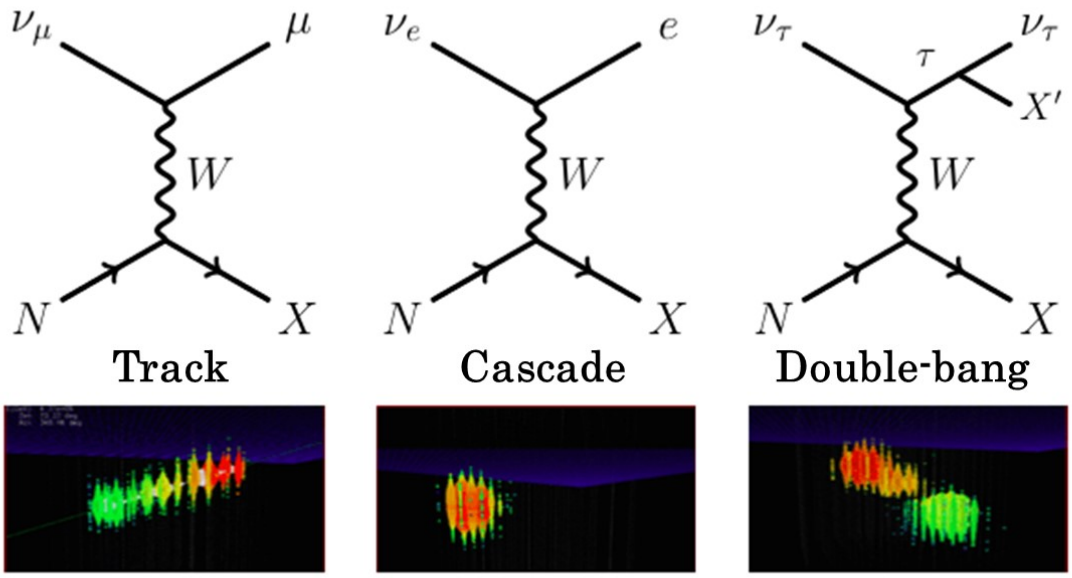

Figure 2.10: Topologies of neutrino interactions from simulated events.

Events are typically categorised by their topology and classified as either track or cascade, as labelled in 2.10 and different analysis procedures are applied to each type of event. While track events can be associated with muon neutrinos cascade events can be any neutrino flavour. Flavour ratio studies in IceCube typically use the ratio of cascade and track signatures to determine the most likely flavour ratio of the event sample.

In terms of determining physical properties of the neutrino, such as its direction

and energy, there are advantages and disadvantages associated with both cascade and track events.

For instance, cascades deposit their energy within a small spatial region while muons deposit energy over their entire track length. As a consequence cascade events typically have superior energy resolution which is one of the advantages of a cascade study compared with a muon study. It is not currently possible to distinguish hadronic and electromagnetic cascades. In the case of hadronic cascade for the same deposited energy there are about 20% fewer photons produced[78] which leads to an unavoidable uncertainty in the energy estimation. The typical energy resolution for cascade events is around 15%.

The length of the cascade is less than 5 m for energies below 10 PeV. Comparing this length with, particularly, the separation of strings in IceCube, but even the vertical separation of DOMs on a string, it can be seen that a cascade event is essentially a point-like source of light. Initially the light is emitted along the Cherenkov angle relative to the particle trajectories in the shower. However scattering in the ice largely isotropises the emitted light distribution. It is possible to get some direction reconstruction due to the initial anisotropy in the light emission however but the direction resolution is limited. For energies greater than 100 TeV a direction resolution of 10° can be achieved[79, 81]. Figure 2.11 is another example of an event display for a cascade event.

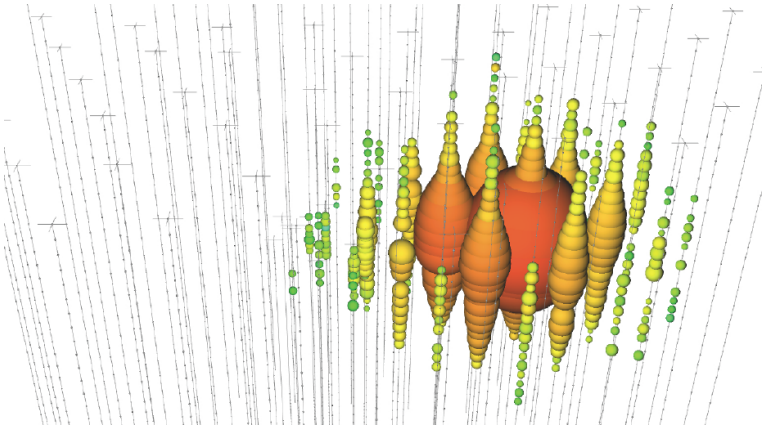

Figure 2.11: Visual pattern of a cascade event.[Marek Kowalski and IceCube Collaboration, "Neutrino astronomy with IceCube and beyond", J. Phys.: Conf. Ser. 888 012007, (2017).]

On the other hand, the track like events have a more precise directional pointing resolution which is a key advantage of track analyses. The angular resolution for muon tracks and consequently the direction of its initial neutrino is about 0.6. This has been confirmed by the analysis of the Moon and Sun in cosmic-rays [80]. An-

other advantage of muon studies is the improvement of the effective area, because a neutrino can interact outside the detector and still (via the muon's range) makes light in the detector. While a disadvantage for track events is that it is harder to tell apart a neutrino-induced muon from the dominant atmospheric muon and muon bundle background which is discussed below.

This motivates and shapes the so-called event analyses which traditionally have been divided into cascade analysis and muon neutrino analysis. Recently there have been analyses which seek to include both cascade and track type events. The aim of all analysis procedures is to remove or reduce as much as possible, the background events, which as explained earlier are primarily muons from the interactions of cosmic rays. It is believed that only neutrinos can propagate through the Earth and hence arrive from below. Thus the upgoing neutrinos are more likely to be signal events and consequently, high-energy neutrinos which come from below are of our interest. However, it is worth noting that the upgoing data is dominated by atmospheric neutrinos, and it took us longer to confirm astrophysical neutrinos in the upgoing data than in the downgoing data where we saw it first. The important point is that a cascade sample takes advantage of both upgoing and downgoing, and is generally better at seeing downgoing events. It tells apart signal events from the muon background by looking at the shape, and then separates atmospheric neutrinos and remaining muon background that happens to occasionally make cascade-like events from astrophysical neutrinos by fitting the diering energy and zenith profiles. In uncontained cascade analyses, the remaining muon background can be as dominant as the atmospheric neutrinos [82].

2.5.1 Background rejection

Although IceCube aims to detect neutrinos the vast majority of events detected are muons created by cosmic rays interacting in the Earth's atmosphere. The event rate in IceCube is around 3000 Hz with around 10^6 more atmospheric muons than muons from neutrino interactions. These events are background in the search for neutrinos. Atmospheric neutrinos are also a background for astrophysical neutrino searches.

Different strategies are used to isolate signal from background and usually involve multi-stage filtering processes with selection criteria optimised to select signal events. The filtering is usually done in stages so that more sophisticated routines can be run at later stages whereas the length of time these routines take to run makes them prohibitive to use on all events detected by IceCube.

Some of the strategies employed are:

Cascade search IceCube cascade analyses isolate events with a cascade topology in the event sample. In theory this should allow a pure sample of neutrino events, however atmospheric muons can appear like cascades if, for example, their path crosses a corner of the detector. Another case when a muon can produce a light pattern which looks like a cascade, is when the Cherenkov light from the muon itself is not well detected and the muon has a large stochastic energy loss which itself initiates a particle shower. Cascade event samples will have contributions from both atmospheric and astrophysical neutrinos. However the self-veto nature of contained event strategies means that the number of downgoing atmospheric neutrinos is reduced. The self-veto concept is described further in the High Energy Starting Event description below. As explained above, cascade events have good energy reconstruction which means that cascade analyses are good for studying the neutrino energy spectrum.

Upgoing track search The upgoing track search exploits the fact that the Earth acts as a shield for atmospheric muons. An upward going track can only have been produced by a neutrino as muons cannot penetrate the Earth. The upgoing track event sample contains both atmospheric and astrophysical neutrinos.

High energy Starting Event selection (HESE) The HESE search selects high-energy events and events where there is no light detected in the upper or outer parts of the detector. The event sample is a mixture of tracks and cascades but is dominated by cascade events. The strategy of using the upper and outer DOMs to identify and veto incoming muons, also removes down-going atmospheric neutrinos. This is due to the so-called self-veto effect and is because an atmospheric neutrino will be produced in an atmospheric air shower and have a high probability of being accompanied by a muon from this air shower. The muon, could be the muon, produced with a muon neutrino in the decay of a pion for example, or a merely a muon also present in the shower. The HESE search was the search strategy which gave the first strong evidence for astrophysical neutrinos as described in section 1.3.1.

Point source searches Searches for astrophysical points sources seek clustering in a sample of events with well-reconstructed directions. Usually track events are used in point source searches but there have been analyses which use cascade event selections. Well reconstructed down-going events can also be used in point source searches, as even though the sample is dominated by atmospheric muons, this background distribution is isotropic.

2.5.2 Importance of ice property characterisation

In order to determine the physical properties of the detected neutrinos, algorithms called reconstruction routines are employed. These are developed using a simulation of the whole detector process from neutrino propagation and interaction, to light propagation in the ice and simulation of the detector elements. For the simulation process to be an accurate model, the optical properties of the ice need to be well characterised. The ice characterisation has an impact for the determination of the direction and energy of the neutrinos, and also for the success of the background filtering strategies. In the next chapter I will discuss the modelling of the ice and in the later chapters I present my research in calibrating the ice and the DOM positions.

2.6 IceCube - Gen2

The IceCube collaboration is currently working on the construction of a new generation of IceCube detector, referred to as IceCube-Gen2. This prospective extension of IceCube will be ten times larger in volume than the current IceCube telescope. The aim of the Gen2 telescope is to gain a higher sensitivity to astrophysical neutrinos with energies greater than 100 TeV. Based on the information gained by the studies conducted with IceCube about the properties of the Antarctic glacier, the spacing between light sensors will be around 250 metres in IceCube-Gen2, instead of the current 125 metres. The deployment of sensors in strings with larger spacings will enable the IceCube-Gen2 instrumented volume to grow sufficiently. The larger spacing means a higher threshold in neutrino energy, however the current IceCube detector is able to already investigate the lower energy flux of neutrinos. IceCube-Gen2 will benefit from the successful designs of the hot water drill systems. By roughly doubling the instrumentation already deployed, the telescope will achieve a tenfold increase in volume to about 10 cubic kilometres, aiming at an order of magnitude increase in neutrino detection rates.

3 Ice Properties and Ice Models

A good understanding and characterisation of the ice, in which the IceCube detector is embedded, is essential for obtaining reliable results with the detector. While the Antarctic ice is remarkably clear there are some impurities. As the ice has accumulated over tens of thousands of years, it has a stratified impurity profile which results in the ice possessing depth-dependent optical properties. In this chapter I will describe some of the properties of the ice, the instrumentation used to study these properties and models developed to describe them. In the following chapters I will present my research contribution to our calibration of the ice.

3.1 Ice Calibration

Ice Calibration refers to determining the characterisation of the ice which provides the best fit between simulated and measurements taken with calibration devices.

3.1.1 Calibration Devices

Some of the devices used for calibration are described below:

Dust Loggers A dust logger is an approximately 1 metre long compact optical device. Figure 3.1 shows a schematic of the dust-logger and its method of operation. The two main components of a dust loggers are a photomultiplier tube (PMT) on one end and a light source on the other end. In addition, to the light emitter and receiver, another important component of a dust logger are the brushes. Several brushes are required to place in between the light source and the PMT to block the emitted light reaching the PMT directly through the water. These brushes are used to assure that the recorded signal by the PMT is only correlated with the scattering property in the ice [83].

Two types of dust loggers have been used in IceCube in two operational modes:

- **Disposable Dust Logger:** A disposable dust logger is a type of dust logger that can be deployed together with a DOM string. It is usually attached to the main cable between the bottom DOM - DOM number

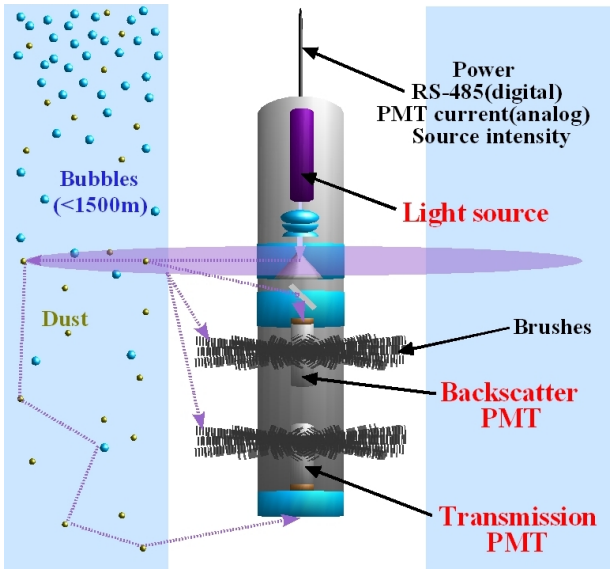

Figure 3.1: Dust logger schematic. [IceCube wiki page: "Dust logger", `https://wiki.icecube.wisc.edu/index.php/Dust_logger`].

60- and the weight stack, and an extension cable runs between the dust logger and the bottom breakout, just above DOM number 59. This type of dust logger usually uses data from the string to assess the pressure in order to determine the depth. It can however, carries its own pressure sensor.

- **Reusable Dust Logger:** There are some differences between disposable dust loggers and reusable ones; first, a reusable dust logger is used to log a hole before the deployment, whereas as it is mentioned above the disposable dust logger is being used as a part of deployment process; second, reusable dust loggers produce two logs for the hole: a downhole log and an uphole log. These two logs can be used for reciprocal calibration; third, unlike disposable dust loggers, a reusable dust logger always has its own pressure sensor for depth determination.

Standard Candles Standard Candles are used to calibrate the energy and vertex reconstruction for cascades. A standard candle is an in-ice 337 nm pulsed Nitrogen laser module with a well-known location [84]. The Standard Candle uses a reflective cone to simulate the Cherenkov light from an electron-neutrino induced cascade propagating through the ice. The light output of a standard candle is precisely calibrated which should enables us to use it as a credible tool for verification of our Monte Carlo simulation of cascades[1]. A schematic

[1]Systematic uncertainties in the output of the standard candles when in the ice has limited

of the location of Standard Candle Mark I in the IceCube array is shown in figure 3.2.

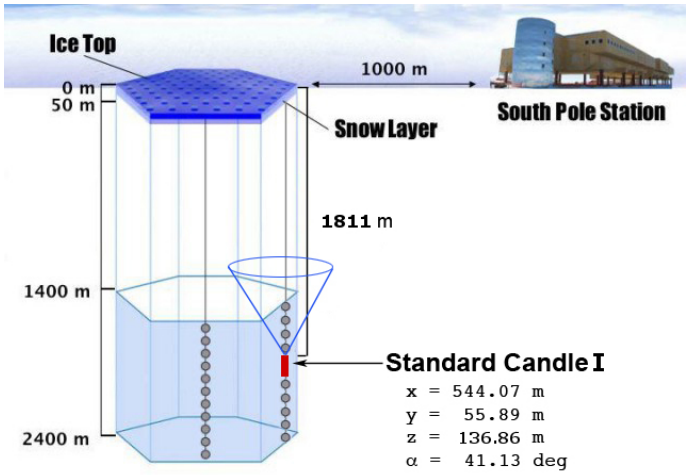

Figure 3.2: Schematic of the location of Standard Candle Mark I in the IceCube array.[IceCube wiki page: "Standard Candle", `https://wiki.icecube.wisc.edu/index.php/Standard_Candle`].

Bubble Cameras The bubble camera is used to study the air-bubbles in the hole ice, their formation and their properties. As described in section 3.5.1, it is believed that the abundance as well as the scattering pattern of the air bubbles in the hole-ice is different from the bulk ice. For example, it is hypothesized that the formation of air-bubbles in the hole-ice around the DOMs, causes an increase to the scattering of the light from above into the DOM. Studying the formation of the air-bubbles as the water freezes in the hole as well as determining the time constant for conversion to a non-scattering clathrate phase are the main motivations for designing and deploying bubble cameras as one of the calibration devices.

A bubble camera consists of two standard glass spheres which are mounted a few meters apart from each other, below the end of the string. Each of those glass spheres has its own camera along with six bundles of white LEDs. The camera in the upper sphere is looking up at DOM 60 and the camera in the lower sphere is looking down the hole below the string [85]. See figure 3.3.

Laser Rangers Laser rangers are used to measure the distance to any given object by sending a laser pulse to that object and recording the time it takes for the pulse to reflect off the object and return to the device. Laser rangers were

their effectiveness unfortunately

Figure 3.3: The Bubble Camera assembly goes down hole 57. The picture shows the two spheres.[IceCube wiki page: "Bubble Camera", `https://wiki.icecube.wisc.edu/index.php/Bubble_Camera`].

used during deployment to measure the well depth in the hole and to verify DOM spacings [75].

Inclinometers An inclinometer, also known as a tilt meter, is used to measure the slope angle, elevation or inclination of an object with respect to gravity. Several inclinometers have been deployed deep in the ice in order to measure the ice-flow.

A few more devices are also used for calibration purposes, such as *Thermistors* which are used to measure the temperature profile of the ice; *Pressure Sensors* which were used during deployment to monitor its progress (and detect a stuck string) and to determine the depth of the string and also *Muon Taggers* which are solely used for IceTop tank calibration.

3.2 Ice Properties

The optical properties of the ice are closely related to its physical properties, such as the impurity distribution. These properties are described below.

3.2.1 Physical Properties of the Ice

Dust Particulates : Glacial ice contains some impurities brought in by the wind. The presence of these particulates greatly affects the propagation of light. During stadials, periods of colder than average climate, it is generally drier and windier. This means that impurities from different parts of the globe are less likely to be taken out of the atmosphere by precipitation and can reach

Antarctica. The dust particulates in the South Pole consist of different elements, such as mineral grains, sea salt crystals, liquid acid drops and volcanic soot. Each of these elements has different contributions in the optical properties of ice as described in table 3.1. Note that in this table a ✓ indicates that there is a high level of dependency, whereas a ✗ indicates that either there is no dependency or this dependency is negligible.

	Air Bubbles (>= 1300m)	Air Hydrates (>1300m)	Temperature	Mineral Grains	Sea Salt Crystals	Liquid Acid Drops	Soot
Absorption	✓	✓	✓	✓	✗	✗	✓
Scattering	✓	✗	✗	✓	✓	✓	✗

Table 3.1: Effective factors on absorption and scattering properties of the ice.

The dust in the ice of the detecting region of IceCube was deposited in the late Pleistocene era[79]. The variation in climate results in four distinctive depths where the concentration of these particles is significantly higher than other depths. These four peaks can be seen in figure 3.4, showing the dependence of scattering with depth, and are labeled *A, B, C,* and *D*. The highest peak, *D*, is known as the "dust peak".

Air Bubbles & Air Hydrate : One of the characteristic features of polar ice is the existence of pockets of air called air bubbles. Since the pressure increases with increasing depth the size of these air-bubbles decreases as a result. At sufficiently low depths in the ice, the pressure exceeds the required formation pressure and most of the bubbles are converted to crystals called air hydrate crystal and consequently the number of air-bubbles decreases. The refractive index of these hydrate crystals is only 0.4% larger than that of pure ice [86], which makes scattering on these crystals negligible.

Since the rate of transformation of the air-bubbles to air-hydrate is slow, these two coexist down to almost 1500 m depth [87]. It was first predicted based on AMANDA scattering results in 1997 that all air-bubbles should be transformed into air-hydrate crystals at 1500 m [88]. It was later confirmed in measurements conducted in 2000. This indicates that at greater depths the major dependence of the optical properties is on the concentration of dust particles in the ice [89]. The fact that at depths below 1350 m no air-bubbles exist, was one of the main motivations for locating the IceCube below this depth.

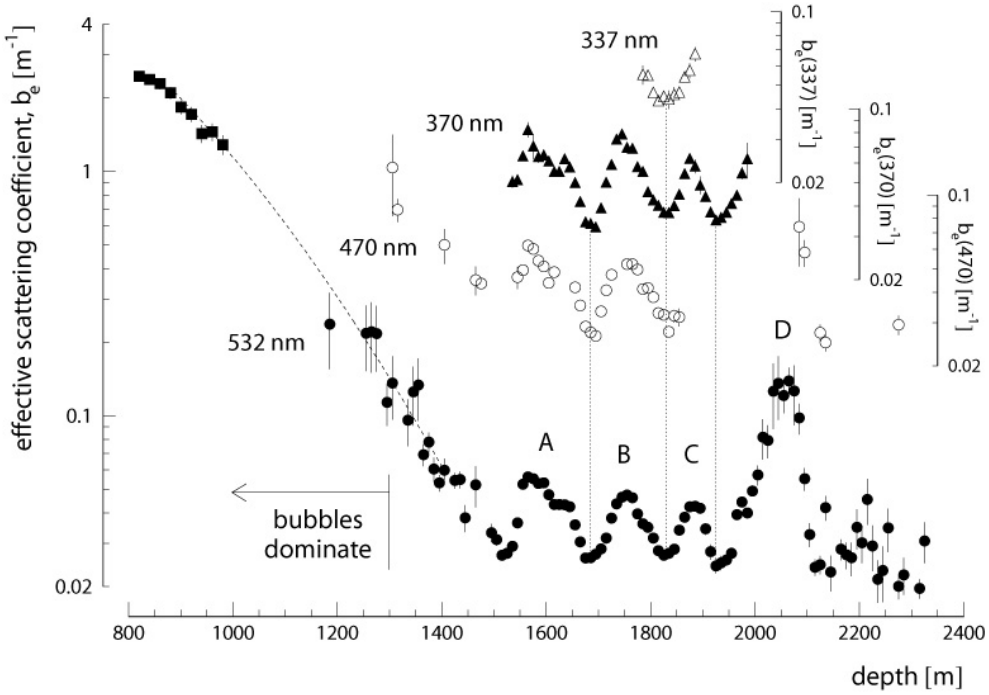

Figure 3.4: Depth dependence of the effective scattering coefficient measured with pulsed sources at four wavelengths. The four peaks labeled A through D correspond to stadials in the last glacial period. A broad dust peak due to the Last Glacial Maximum, expected at ∼1300 m, is masked by bubble scattering. Between 800 and 1000 m scattering is dominated by bubbles and does not depend on wavelength. [Ackermann et al. "Optical properties of deep glacial ice at the south pole". Journal of Geophysical Research, 111:126, (2006).]

Temperature : There is a relation between absorption and temperature[90]. In 2001 in a study conducted by Woschnagg and Price a significant temperature dependence of the molecular absorption at the wavelengths greater than 500 nm was observed [91]. The same study along with some others later proved that for the shorter wavelengths, ice absorption is negligible compared with dust absorption mainly because the temperature effect is not detectable. However, since both in-situ light and Cherenkov light are emitted in a range of wavelengths that includes the wavelength greater than 500 nm the temperature should be accounted for in any absorptivity measurement. The temperature increases as the depth increases in South Pole ice as can seen in figure 3.5[92]. Different measurements have been done over the last years. AMANDA was the first which measured the temperature of the ice at the bottom to be approximately -9° C. The latest extrapolation, however, indicates that the ice at is 3° C warmer at bedrock than previously estimated, but this is still sufficiently cold to be well below the melting point.

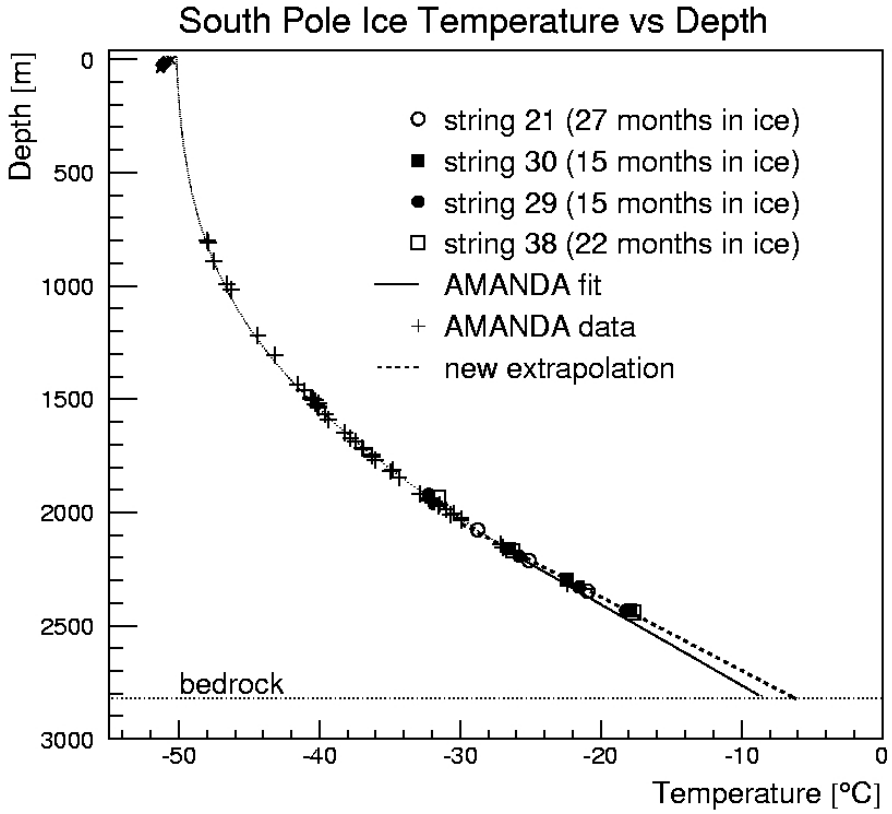

Figure 3.5: Ice temperature profile measured with thermistors in AMANDA. [P. Buford Price et al. "Temperature profile for glacial ice at the South Pole:Implications for life in a nearby subglacial lake", PNAS June 11, (2002).]

3.2.2 Optical Properties of the Ice

The important parameters to describe photon propagation in a transparent medium are: the average distance to absorption, the average distance between successive scatters of photons, and the angular distribution of the new direction of a photon at each given scattering point. These properties are the optical properties of the ice.

3.2.2.1 Absorption

The absorption length is defined as the distance a photon travels before the survival probability decreases to $1/e$. The absorption coefficient which is the inverse of the absorption length is the term which is used more often. The absorption length is depth and wavelength dependent. The parameterisation used in IceCube is given in section 3.3.

The depth and wavelength dependence of the absorption coefficient is shown in figure 3.6. The dashed line at 2300 m shows the sum of two components for

the wavelength dependence of the absorption: a power law due to dust and an exponential due to the ice.

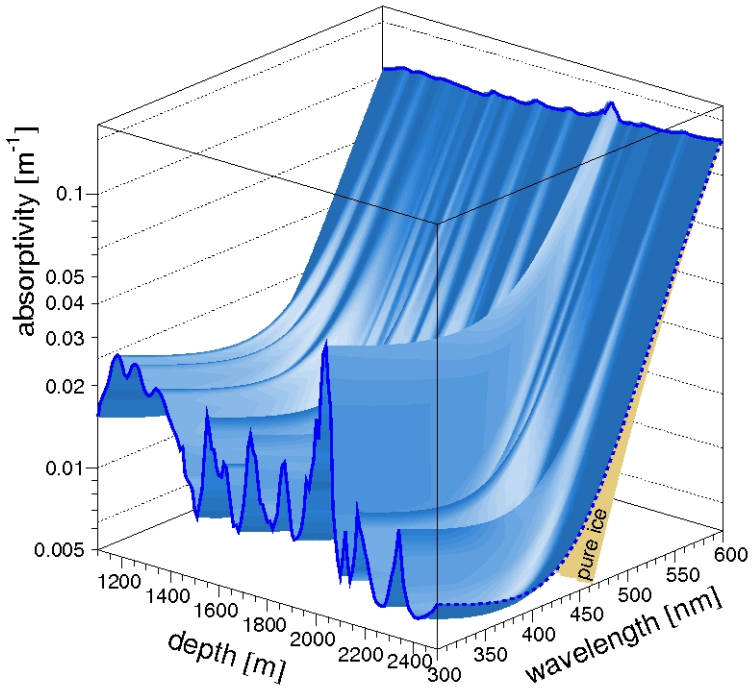

Figure 3.6: Maps of the absorption for deep South Pole ice. [Ackermann et al. "Optical properties of deep glacial ice at the south pole". Journal of Geophysical Research, 111:126, (2006).]

In figure 3.7 we can compare the measurements of absorptivity derived from three different studies: one shows the measurements in South Pole ice at three depths greater than 1500 m, two shows the same measurements on laboratory-grown ice, as reviewed by Warren [1984] and the third one represents the absorptivity in South Pole ice measured between 800 and 1000 m.

In South Pole ice, depths below 1500 m correspond to ages in the late Pleistocene while depths between 800 and 1000 m correspond to the relatively warmer Holocene time period after the Last Glacial Maximum. During the Holocene, dust concentrations in the atmosphere were significantly lower than during earlier periods[93]. At longer wavelengths, ice absorptivity displays spectral structure corresponding to modes of molecular stretching and bending.

3.2.2.2 Scattering

The scattering length is defined as the mean free path between scatters in the medium which is due to deflection of photons as they interact with the dust par-

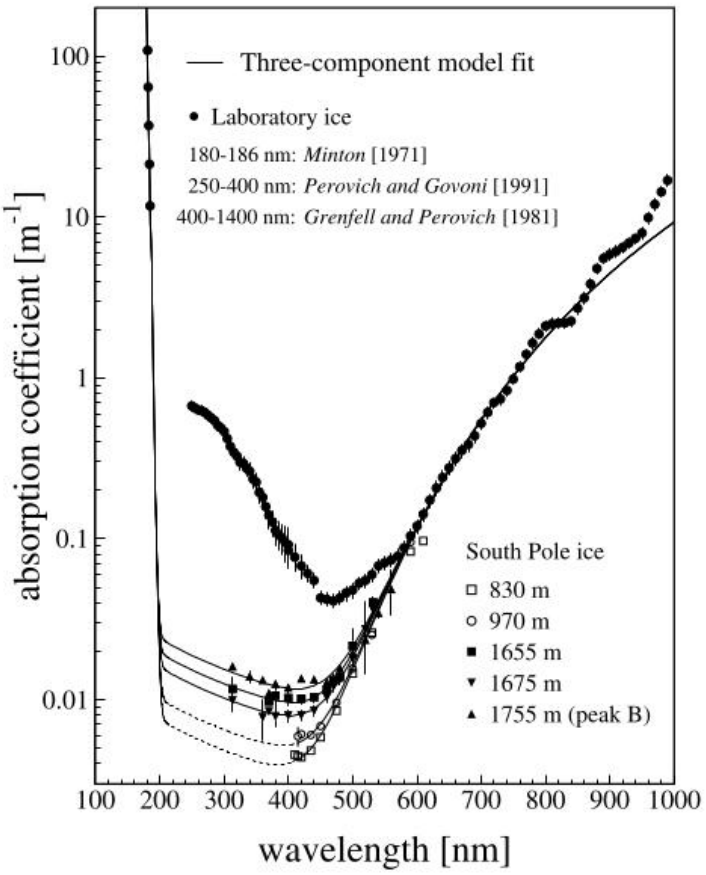

Figure 3.7: Wavelength dependence of absorption from ultraviolet to infrared, for deep South Pole ice and for laboratory-grown ice. [Ackermann et al. "Optical properties of deep glacial ice at the south pole". Journal of Geophysical Research, 111:126, (2006).]

ticulates and air bubbles (described above) in the ice. In the shallow ice scattering is mostly because of the presence of air-bubbles, but as explained above, at depths below 1350 m, these bubbles are converted into air-hydrate due to the increased pressure [79] and since air-hydrates have the same refractive index as ice they are non-scattering.

The average scattering angle is also an important quantity for characterising the scattering in the ice. The average scattering angle probability $<\cos(\theta)>$ is estimated to be 0.94 in the South Pole ice for the dust component. Since one cannot measure the scattering length (λ_s) and the average scattering angle independently, the effective scattering length is defined

$$\lambda_e = \frac{\lambda_s}{(1 - <\cos(\theta)>)}. \tag{3.1}$$

This can be interpreted as the distance after which the photon scattering distance becomes isotropic.

Like absorption, it is more convenient to use the reciprocal of the effective scattering length, the effective scattering coefficient (b_e).

The depth and wavelength dependence of the absorption coefficient is shown in figure 3.8. The dashed line at 2300 m shows the wavelength dependence which is a power law due to dust for scattering.

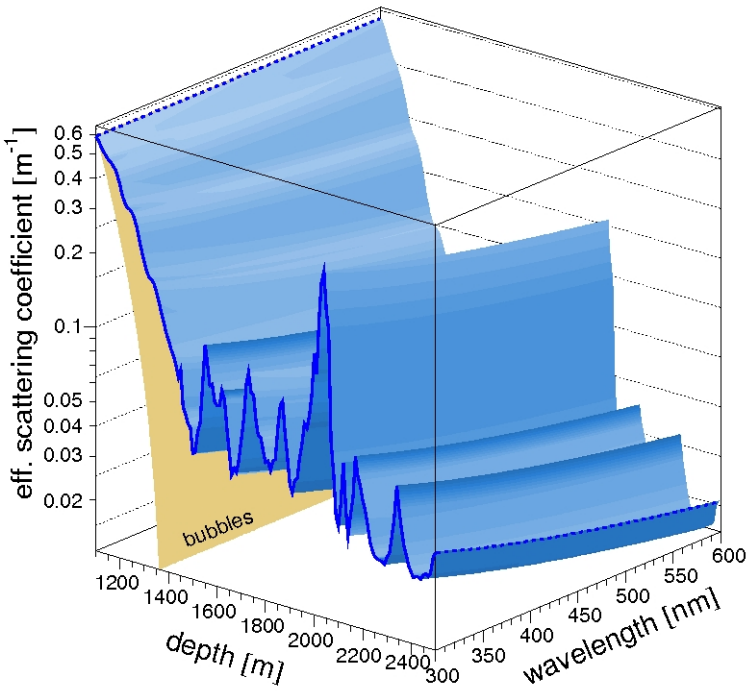

Figure 3.8: Maps of optical scattering for deep South Pole ice. [Ackermann et al. "Optical properties of deep glacial ice at the south pole". Journal of Geophysical Research, 111:126, (2006).]

Mie theory can describe the scattering in the ice because the size of the wavelengths which are relevant are similar to the size of spherical particles. As the light is moving, it is scattered in the forward direction along its path and thus the Henyey-Greenstein function is the most appropriate function for describing the distribution of the scattering angle [94]. The Henyey-Greenstein scattering angle function is:

$$p(\cos\theta) = \frac{1}{2}\frac{1- < \cos\theta >^2}{(1+ < \cos\theta >^2 -2 < \cos\theta > \cos\theta)^{3/2}}. \tag{3.2}$$

For values where $<\cos\theta> = 1$, the light is mostly scattered forward but for values where $<\cos\theta> = 0$ the scattering is isotropic and when $<\cos\theta> = -1$, the scattering is backwards [94]. In the IceCube detector, the values between 0.8 and 0.94 are used for the average scattering angle [95].

In a study conducted by Price and Bergstrom in 1997, in-situ light sources capable of emitting light at four different wavelengths were used [96]. Those light-sources

were deployed in depth range between 1530 m and 2000 m. The extracted data enabled them to fit the wavelength dependence. As it can be seen in figure 3.9 a power law, $b_e(\lambda) \propto \lambda^{-\alpha}$, was introduced, with $\alpha = 0.9 \pm 0.03$. The error includes a 5% systematic uncertainty that was added to the statistical error of each data point. I will discuss the systematic and statistical errors with more details in the next chapters.

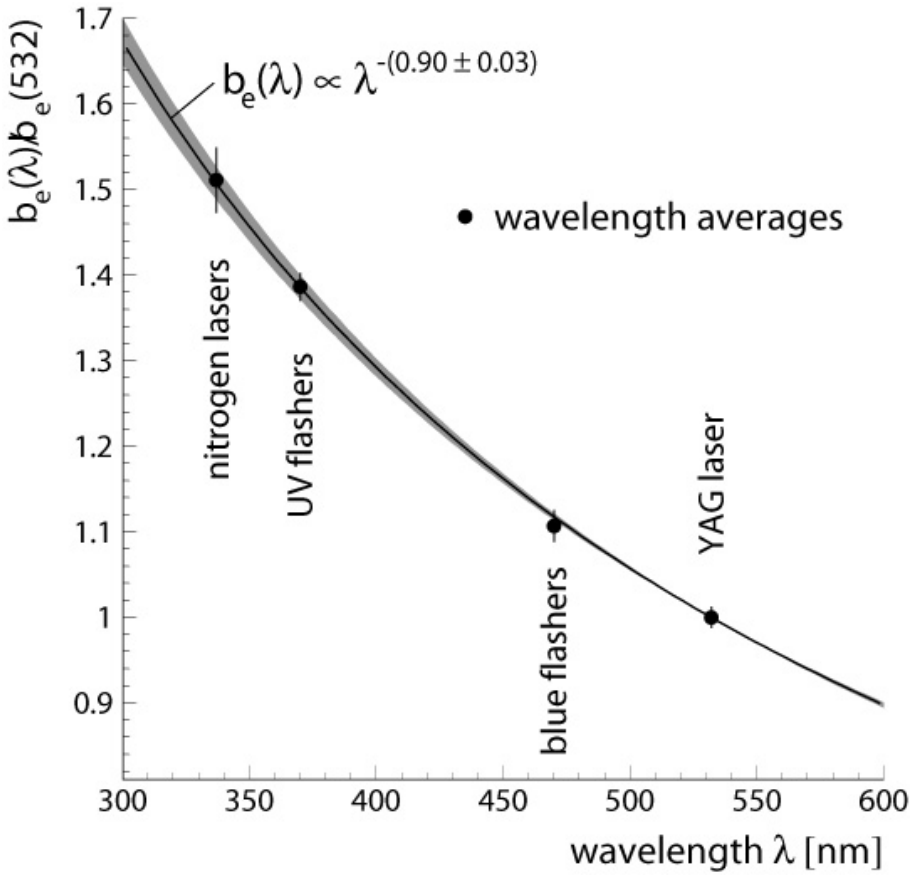

Figure 3.9: Wavelength dependence of scattering. The data points are wavelength averages and are normalized with $b_e(532)$. [Ackermann et al. "Optical properties of deep glacial ice at the south pole". Journal of Geophysical Research, 111:126, (2006).]

3.3 Six parameter ice description

The wavelength dependency of the absorption can be expressed by:

$$a(\lambda) = A_U e^{-B_U \lambda} + C_{dust} \lambda^{-\kappa} + A_{IR} d^{\frac{-\lambda_o}{\lambda}}, \tag{3.3}$$

where, λ is the wavelength, C_{dust} characterises the amount of dust. κ in this expression represents the size and composition of the dust grain. A_{IR} is the molecular

absorption factor which is seen in far infrared wavelengths. The first and third term refer to absorption effect of the ice. The first term represents the effects on ultraviolet wavelengths, while the third term characterises the absorption at the far infrared end of the electromagnetic spectrum. Since IceCube is only sensitive to wavelengths greater than 300 nm, the first term can be neglected[79] for IceCube purposes. With this assumption, a six parameter description of the ice is used to describe the scattering and absorption properties:

$$b_e(\lambda) = \left(\frac{\lambda}{400}\right)^{-\alpha} b_e(400) \tag{3.4}$$

$$a(\lambda) = \left(\frac{\lambda}{400}\right)^{-\kappa} a_{dust}(400) + A_{IR}^{\frac{-\lambda_o}{\lambda}} . \tag{3.5}$$

Absorption and scattering coefficients at wavelength ($\sim$ 400 nm), $a_{dust}(400)$ and $b_e(400)$ are two of the six parameters. The remaining four variables α, κ, $\mathrm{A_{IR}}$ and $\mathrm{a_{dust}}$ allow the scattering and absorption coefficient at other wavelengths to be calculated from those at 400 nm.

As mentioned earlier, it is believed that absorption has temperature dependence. Equation 3.6 is the latest modified expression for the absorption coefficient

$$a(\lambda) = a_{dust}(\lambda) + Ae^{-B/\lambda}(1 + 0.01.\delta\tau), \tag{3.6}$$

with

$$a_{dust}(\lambda) = a_{dust}(400)\left(\frac{\lambda}{400}\right)^{-\kappa} . \tag{3.7}$$

Here, $\delta\tau$ is the temperature difference relative to the depth 1730 m (centre of AMANDA): $\delta\tau = T(d) - T(1730)$. As in equation 3.5, the wavelength of 400 nm is used as the reference wavelength

3.4 Ice Models- A Summary

The ice models are used for simulations of the detector for physics purposes, for example for developing filtering strategies to isolate the signal from background, and for developing reconstruction routines for characterising the neutrino signal events.The modeling of the IceCube ice is being continuously refined. Models are released and named so that simulations can be well documented in terms of the assumptions and inputs used.

In general each ice model will consist of the best fit values of the parameters in the six parameter function described in section 3.3. The parameters $a_{dust}(400)$ and

$b_e(400)$ are tabulated as a function of depth in 10 m depth intervals. A scattering function is also associated with an ice model.

Various codes have been developed for simulating the photon propagation through the ice. These codes take as input an ice model description of the ice and the details of a light source such as its position in the detector and the angular and wavelength profile of light emission. The output of the code is the light distribution that is predicted to be detected by each DOM. The code currently in use is the Photon Propagation Code (PPC), developed by Dmitry Chirkin[97]. Further details on PPC are given in section 4.3.

Ice model development began in the 1990s for AMANDA. The first models were "bulk ice" models where the same scattering and absorption coefficients were used at all depths. These models were superseded by models in which the coefficients were tabulated in 10m depths. Some of the most influential models used prior to 2012 were the Millenium, AHA (Additionally Heterogeneous Absorption model) and WHAM (Water Hardened Antarctic Measurement) models[79].

The ice models currently in use are the Spice (South Pole ice) models introduced by Dmitry Chirkin in late 2009[98]. Like previous models the Spice models are based on the six parameter description of scattering and absorption as introduced in section 3.3.

A feature of the Spice models as compared to the previous models is that the best fit of the model to the data is determined by a log-likelihood function. The likelihood expression which is used, was developed by Dmitry Chirkin and is described in sections 4.4 and 6.1. The likelihood method facilitates the systematics to be fitted along with the model parameters. In addition, for Spice models, the coefficients of absorption and scattering are allowed to vary independently for each 10 m depth interval until the best fit is found which was not the case for earlier ice models. Treatment of the hole-ice was included for the first time in Spice models, through a variation of the angular acceptance curve of the DOMs.

In the first of the models, Spice-1, the first guess in the procedure of iterative fitting was seeded by the AHA fit, while in subsequent models a uniform seed was used. Spice-1, and other Spice models developed before 2013, used the Henyey-Greenstein scattering function. In 2013 the Spice-Mie model was introduced. The main difference between Spice-Mie and Spice-1 was the scattering function. In Spice-Mie a combination of Henyey-Greenstein(55%) and Simplified Liu(45%) for a total scattering coefficient of $<\cos(\theta)>= 0.9$ is used. Below $<\cos(\theta)>= 0.8$ the Henyey-Greenstein and Mie scattering are the same [99], but above this value the Simplified

Liu is a better phase function:

$$\text{Liu phase function} = \ \mathrm{K}\,(1 + \epsilon\cos < \theta >)^{\mathrm{n_p}}\,, \tag{3.8}$$

where K is the normalization constant, ϵ is the characteristic factor and n_p is the anisotropic index. Setting $\epsilon = 1$ further simplifies the equation. It has been shown that at higher values of $<\cos(\theta)>$, the Simplified Liu phase function is the best approximation with Mie theory. This fit is shown in figure 3.10) [99].

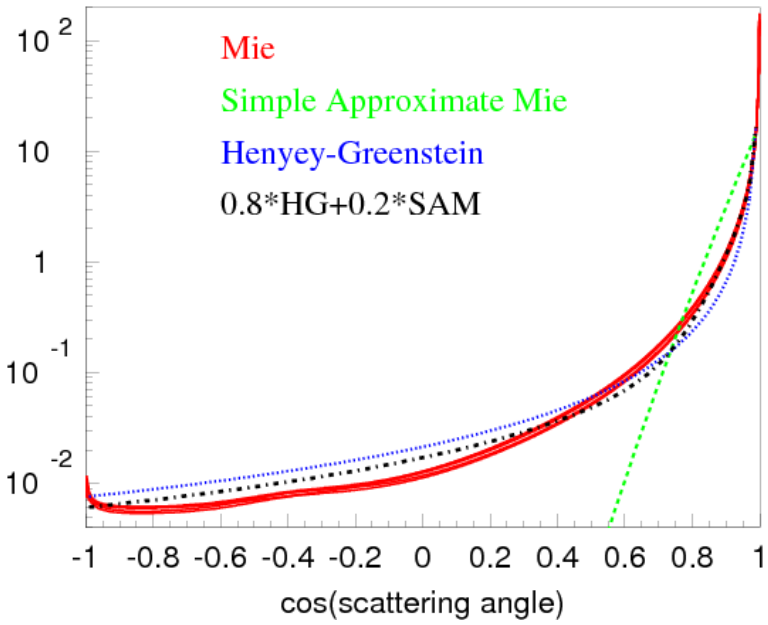

Figure 3.10: Comparison of the Mie scattering profiles calculated at several depths of the South Pole ice with the Henyey-Greenstein (HG) and simplified Liu (SL) scattering functions. In each, $g = 0.943$. [M. G. Aartsen et al. "Measurement of South Pole ice transparency with the IceCube LED calibration system", 2013).]

Spice-Mie also used data from both the ice-core and the dust logger [100], and by combining them, showed that the ice layers are not perfectly horizontal and exhibit a slight horizontal tilt [101].

The latest iteration of the Spice ice models are numbered as 3.X.Y. These models have updated tilt maps using dust logger data, as well as DOM sensitivity fits and flasher LED pattern unfolding.

In addition, the anisotropy as discussed in section 3.5.5 is included in Spice 3.X.Y ice models. The most recent Spice 3 ice model is called Spice 3.2.2 where 10.6% anisotropy is considered. The model error associated with the ice model has been also reduced from 29% in Spice-Mie to 9.8% in Spice 3.2.2.

Currently a new ice model called "ice model BFRv1" is being developed, in which the birefringent effect of the poly-crystals of the glacial ice is taken into account.

The birefringence is believed to be the main cause of the observed anisotropy of the ice. This phenomena is briefly introduced in 3.5.5 but has not been further used in the analyses presented in this thesis.

3.5 Ice Model Challenges

The ice modelling has been refined over the detector lifetime with a continued improvement in the fit between simulation and measurements of flasher events. However challenges remain. Some of these are described in this section.

3.5.1 Hole Ice

The hole ice is the refrozen column of ice within the drilled holes in which the strings are embedded. In order to deploy the strings that hold the optical sensors inside the glacial ice, a hot-water drilling technique was used. About 48 hours of continuous drilling was required for each column and while the deployment process was conducting the drilled hole was filled with water [75]. It then took a while for the water inside the drilled hole to freeze again. This process means that the properties of the hole ice differ from those of the surrounding bulk ice.

For instance, hole ice contains residual air-bubbles that may increase the scattering property of the ice. The stronger scattering near the DOMs isotropizes their angular sensitivity by increasing the probability for downgoing light which would otherwise have passed by the DOM to scatter into the PMT and be recorded. In the simulation this effect is quantified by applying an angular sensitivity curve which is modified from the angular DOM sensitivity measured in the laboratory.

3.5.2 DOM Efficiency

DOM efficiency (DE) is the efficiency with which a DOM detects photons. We can define the absolute DOM efficiency as the ratio of the detected photons by a DOM to the photons incident on that DOM. But since the number of incident photons are unknown we cannot deduce the absolute efficiency. Therefore, instead of absolute efficiency the Relative DOM Efficiency (RDE) is used and is the ratio of the Individual DOM Efficiency and the Average DOM Efficiency. The main components of the measured RDE are assumed to be quantum efficiency of the PMT (See figure 3.11), transparency of the optical gel and glass pressure housing, and the hole ice.

The efficiency is determined both with laboratory measurements and also with the measurement of the Cherenkov light emitted from muon interactions in the ice.

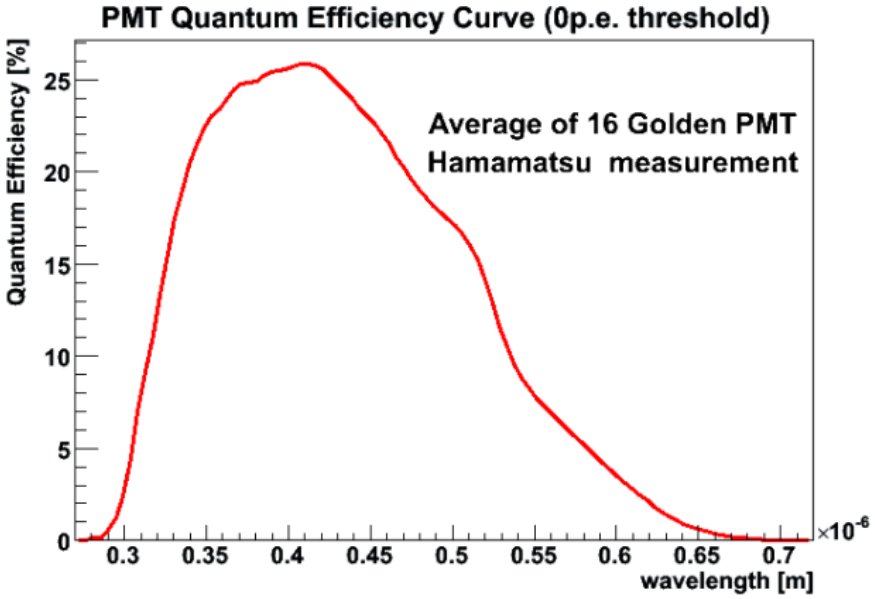

Figure 3.11: Average quantum efficiency of 16 IceCube PMTs as measured by Hamamatsu. [Hamamatsu Photonics, "Large Photocathode Area Photo-multiplier Tubes", (2016).]

Although the same principles are used in both measurements the in-situ one is more realistic because it includes the effects of actual parameters such as cable shadowing and hole-ice.

Typically in order to derive the quantitative value for the DOM efficiency a low-energy muon with well-understood light emission is selected. The number of photons registered by the DOM then will be compared to the predictions of the simulation model. In one study, for instance, in which a low-energy muons with median energy of 82 GeV was selected the central value for the efficiency was adjusted upward by 10% in the simulation, compared to the baseline [102].

3.5.3 Saturation

The dependence of the output currents of a PMT relative to the rate of incident photons is defined as the linearity of the PMT. Two factors can limit the linearity of a PMT: one is space charge effects and the other is the resistivity of the photocathode. Decoupling capacitors can be added, specially to the last dynodes where the largest current is required to decrease the space charge effect [103].

Figure 3.12 shows the linearity of an example IceCube PMT measured at gains between 10^5 and 10^7. LEDs emited light with 200 ns, 410 nm pulses of different intensities. The peak current at the base is calculated from the maximum of the

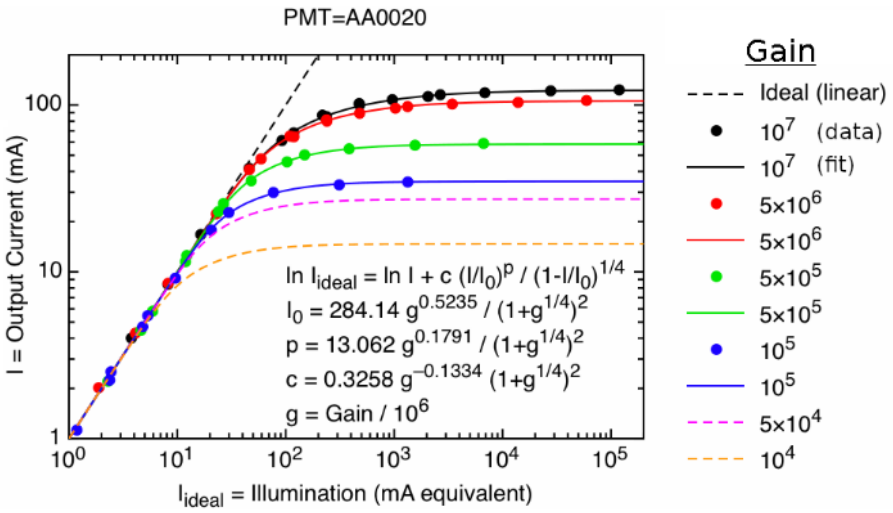

Figure 3.12: PMT saturation characteristics measured as the resulting instantaneous current versus the expected current at different gains. [Chris Wendt and Dahai Liu, "PMT Saturation Lab, In-Ice, FAT", (2006).]

resulting voltage pulse. It was shown that PMTs that are operated at a reduced gain will saturate at larger intensities. At a gain of 10^7 the saturation level is equivalent to roughly 80 PE/ns.

3.5.4 Ice Layer Tilt

As discussed above the ice models assume that the inhomogeneity of the ice can be characterised with horizontal layers. However, studies showed that the ice surface flows 10 m per year along the 40° west meridian which leads to a tilt. Figure 3.13 shows extension of ice layers along the average gradient direction. It can be seen that the lowest layer shows the largest shift of 56 meters between its shallowest and deepest points.

Measurements of the temperature gradient with AMANDA led to a shear model, according to which the top 2000 m moves like a rigid body, the deeper ice slowly lags behind, and the bottom is either stuck or moves very slowly. This velocity profile is shown in figure 3.14. This shear effect causes the so called ice-layers not to be perfectly horizontal, but they are all tilted with respect to vertical.

3.5.5 Anisotropy

Studies conducted using in-situ light sources shows a clear evidence of ice anisotropy at macroscopic scales whereby the absorption and scattering depend on the direction

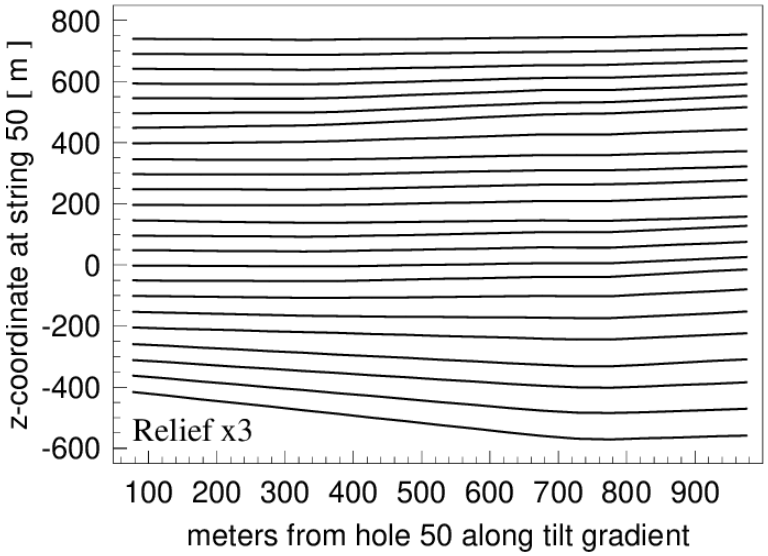

Figure 3.13: Extension of ice layers along the average gradient direction. [M. G. Aartsen et al. "Measurement of South Pole ice transparency with the IceCube LED calibration system", 2013).]

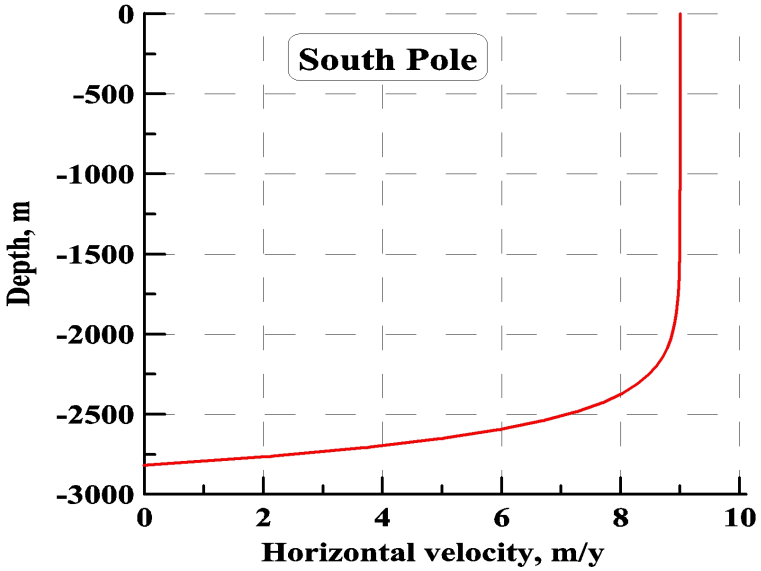

Figure 3.14: Ice velocity vs depth calculated from temperature profile under the assumption that the glacier is stuck at bedrock. [M. G. Aartsen et al. "Measurement of South Pole ice transparency with the IceCube LED calibration system", 2013).]

of photon propagation. This anisotropy seems to correlate with the flow direction of the ice. For example, in one measurement where the receivers were almost 125 metre away from the in-situ light emitter, the DOMs on the flow axis received two times more light than those DOMs which were on the orthogonal tilt axis[104]. This difference was observed while all DOMs regardless of their positions registered the same arrival time for the propagated light. The anisotropy as a function of azimuth

angle is shown in figure 3.15.

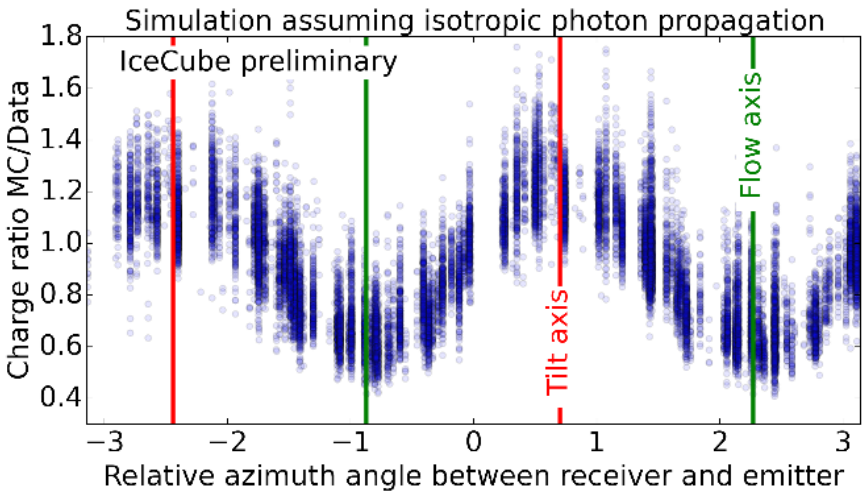

Figure 3.15: Optical ice anisotropy seen as azimuth dependent charge excess in flasher data. [Dmitry Chirkiny, Martin Rongen. "Light diffusion in birefringent polycrystals and the IceCube ice anisotropy", 2019.]

It was first suggested that the hole-ice (the column of ice that was refrozen after the string deployment) or even the supporting cable that hold the DOMs are the sources of the present effect. However, more studies shows that regardless of the DOMs that are being used in the study they always exhibits the same anisotropy effect. Since the properties of the hole-ice as well as the orientations of the supporting cables are not the same for all DOMs such a consistent directional behaviour cannot be explained by these factors only.

3.5.6 Birefringence Anisotropy

Historically, the impurities such as dust particulates presented in the glacial ice were considered to be the only cause for light diffusion in the ice. However, recent studies suggest a new phenomena called *"birefringence"* as the main cause of the anisotropy descibed in section 3.5.5 . Birefringence attributes the ice anisotropy to the properties of polycrystals of the glacial ice, mainly its refractive index. This phenomena and its effects are still under investigation as the best potential explanation for the large scale anisotropy.

It is known that glacial ice is a birefringent polycrystal with a girdle c-axis distribution. This might explain the observed deflection phenomena where the microstructure of ice affects the propagation of light in the ice.

In a homogeneous, transparent, non-magnetic medium the relation between the electric field and the displacement field as well as the magnetic fields is given as

[105]

$$\vec{B} = \vec{H} \tag{3.9}$$

$$\vec{D} = \epsilon \vec{E}, \tag{3.10}$$

where ϵ is the dielectric tensor.

It is known that the dielectric tensor is a symmetric tensor, hence we can always identify a coordinate system in which this tensor is orthogonal

$$M = \begin{pmatrix} n_x^2 & 0 & 0 \\ 0 & n_y^2 & 0 \\ 0 & 0 & n_z^2 \end{pmatrix}$$

with n_i being the refractive indices along the given axes.

Ice, like any other Uniaxial crystals, has two distinct refractive indices: $n_x = n_y \equiv n_\circ \neq n_z \equiv n_e$, where the axis with the unique refractive index defines the optical axis / c-axis.

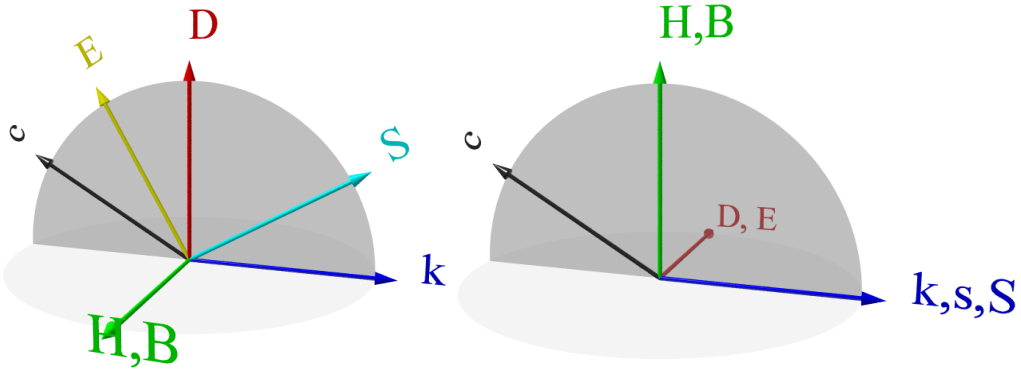

Figure 3.16: Orientation of all electromagnetic-vectors for the ordinary (right) and extraordinary (left) ray with respect to the c-axis [Christoph U. Keller (n.d.). "Crystal Optics." Lecture Notes, Leiden University.]

When light propagates in a uniaxial crystal such as ice, it splits into two waves with orthogonal polarizations, these two waves are called ordinary wave and extraordinary wave.

For the ordinary wave, the electric field vector $\vec{E}$ and the displacement vector $\vec{D}$ are always perpendicular to both the propagation vector $\vec{S}$ as well as the optical axis of the crystal which is denoted by vector $\vec{k}$. The optical axis of the crystal ice and the propagation vectors are themselves parallel.

On the other hand, unlike the ordinary wave, the electric field $\vec{E}$ for the extraordinary wave is not necessarily perpendicular to the propagation vector but it lies in the plane formed by the propagation vector and the displacement vector. However, the electric field vectors of extraordinary waves are mutually orthogonal [106].

While the ordinary ray always propagates with the ordinary refractive index $n_\circ$, the refractive index of the extraordinary ray depends on the opening angle θ between the optical axis $\overrightarrow{c}$ and the wave vector $\overrightarrow{k}$ and can be derived by the following equation:

$$\frac{1}{n^2} = \frac{1}{n_e^2} + \left(\frac{1}{n_\circ^2} - \frac{1}{n_e^2}\right) . \cos(\theta)^2 \tag{3.11}$$

In general, the birefringence strength can be expressed as:

$$\beta = \left(\frac{n_e}{n_\circ}\right)^2 - 1, \tag{3.12}$$

which for ice is $\beta \approx 2 \times 10^{-3}$.

Although many improvements with respect to the anisotropy description have been achieved, the IceCube calibration group are still trying to implement these improvements to the current ice models through introducing a new version of ice model that covers the birefringence effect. However, a fully new ice model can only be released following the completion of the fit of the birefringence based anisotropy model which is still ongoing. While this effect is not included into the analyses related to this thesis, the major anisotropy was considered.

4 DOM Calibration Studies

In this chapter I present two calibration studies which I performed as part of my thesis research. The first study was using flasher data to determine the unscattered light travel time between DOMs. This time is used to determine the relative positions of the DOMs. The second study was to determine the relative orientation of a number of normal and coloured DOMs.

Before describing these studies, I first present some details of the flasher data set and introduce the Photon Propagation Code (PPC) used for generating simulated data and the likelihood function used for determining the best fit simulation. The flasher data set is used for most of my calibration studies.

4.1 All-Purpose Flasher Data set

The all-purpose flasher data set is the set of data which is commonly used to fit the ice properties. The flasher data is taken by flashing 12 LEDs on the flasher board of each DOM. The number of operational LEDs at a single time can be adjusted and also the brightness of each DOM.

In order to build a flasher data set, LEDs are typically flashed at 1.2 Hz in a sequence, using a 70 ns pulse with maximum brightness. In addition to a single LED flashing or all LEDs flashing at the same time, either the six horizontal LEDs or the six titled LEDs on each flasher board can also be operated simultaneously to create a pattern of light with approximate azimuthal symmetry around the flasher string. The choice between having a single LED flashing or a combination of some flasher LEDs are decided according to the purpose of the study.

The emitted photons from the flasher LED(s) are recorded by the PMTs of other DOMs[107]. The signal is communicated to the IceCube Lab after being digitized through ATWD channels. The pulses corresponding to the arriving photons, that are extracted from the digitized waveforms, are binned in 25 ns bins, from 0 to 5000 ns from the start of the flasher pulse. The final flasher-data set is then transferred via satellite to the Northern Hemisphere. This recorded data set includes the total charge as well as the photon arrival times. Figure 4.1 illustrates a pair of emitter-

receiver DOMs on the left and shows an example of the photon time distribution on the right.

A data set that covers all detector depths needs to be produced to determine the scattering and absorption parameters of the bulk ice by performing a global fit of those data. These fits require data taken at very low light levels, to avoid multi-photon pileup detector effects. Most of the flasher data sets used in this thesis, were collected in 2013 and include all DOMs as emitters. In addition, another data set containing events for all individual LEDs, both horizontal and tilted, was recorded in 2017-2018 . This data set was taken to measure the cable position with respect to every DOM. However, it can also be used for other purposes and is used in this thesis in chapter 6 to investigate potential biases introduced by only fitting to the horizontal LEDs and to further investigate directional dependencies.

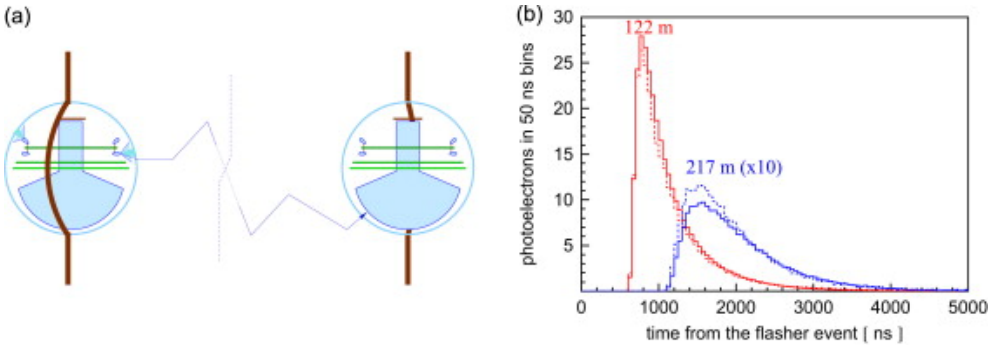

Figure 4.1: Left (a): simplified schematics of the experimental setup: the flashing sensor on the left emits photons, which propagate through ice and are detected by a receiving sensor on the right. Right (b): example photon arrival time distributions at a sensor on one of the nearest strings (122 m away) and on one of the next-to-nearest strings (217 m away; histogram values are multiplied by a factor of 10 for clarity). Dashed lines show data and solid lines show simulation based on the model of this work (with best fit parameters). [M. G. Aartsen et al. "Measurement of South Pole ice transparency with the IceCubeLED calibration system", 2013).]

4.2 Timing for DOM Relative Position Studies

The photons which arrive at each receiving DOM are distributed in time due to the scattering in the ice, with the first photon to arrive being that which was scattered least. The time that an unscattered photon would reach the receiver is called the prompt time. This time can be used, with the speed of light in the ice, to determine the distance between emitting and receiving DOMs.

In this study flashers on string 19 were used as emitters and the waveforms received by the DOMs on the six adjacent strings were examined to determine the prompt time. Figure 4.2 shows the string numbers and from this, it can be seen that strings 11, 12, 18, 20, 27, 28 are the adjacent strings of string 19. Simulations were not required in this study for the prompt time given that the photon is assumed to travel directly.

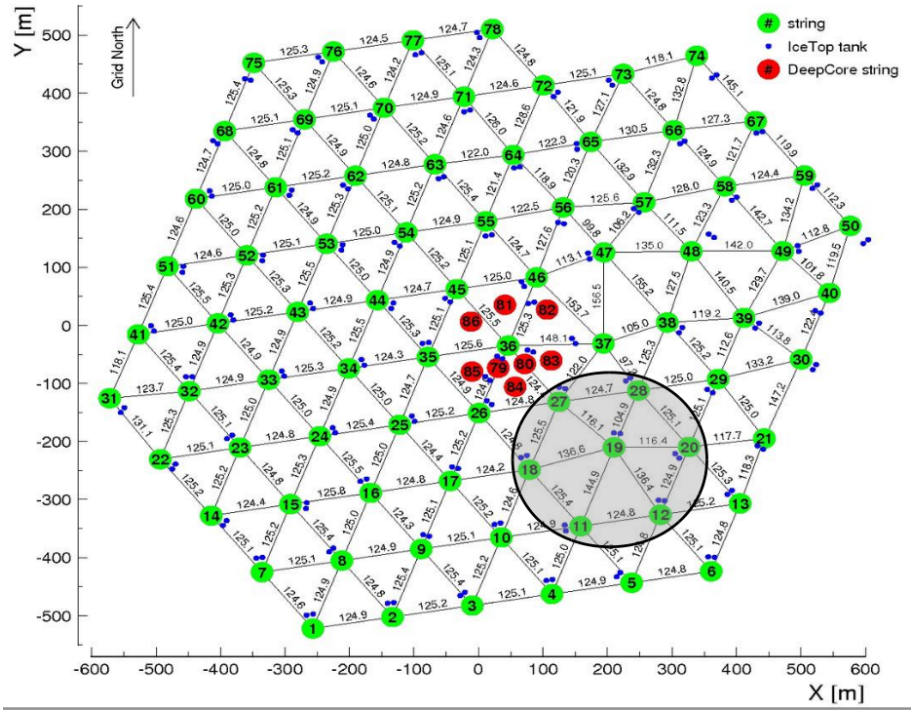

Figure 4.2: IceCube-86 (78+8) inter-string surface. Total number of 162 IceTop tanks are positioned on the surface. Green circles shows the positions of strings with DeepCore strings marked in red. Black circle enclosed string 19 and its adjacent strings (i.e. strings 11, 12, 18, 20, 27, 28) which were examined to determine the prompt time. [IceCube wiki page, "Surface coordinates": `https://wiki.icecube.wisc.edu/index.php/Surface_coordinates`. (2011).]

The arrival photon distribution is binned as a 25 ns histogram. An example for a flasher-receiver combination is shown in figure 4.3. Only the tilted LEDs have been used as flashers.

The estimate for the prompt time is found by fitting a Gaussian to the leading edge of the light distribution and taking the prompt time as the time when the amplitude is 1% of its maximum. The prompt time t_0, is determined through

$$t_0 = \mu - \alpha.\sigma, \tag{4.1}$$

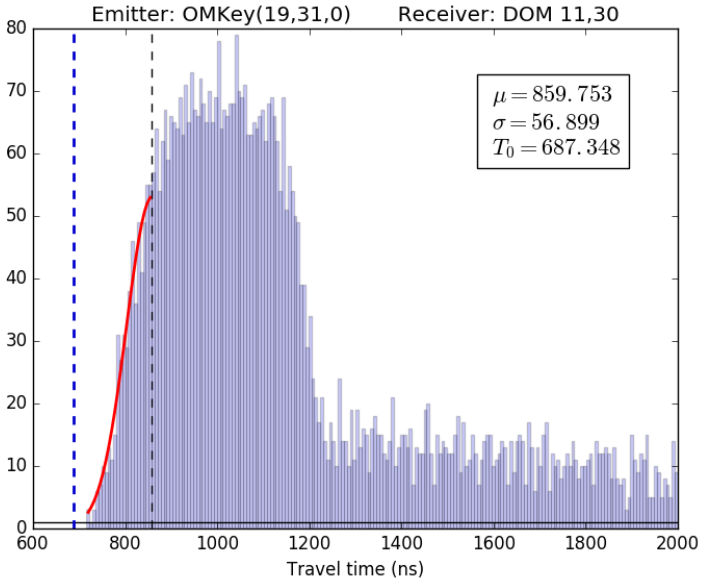

Figure 4.3: The histogram shows the photon arrival time distribution for the emitter, DOM 31 on string 19 and the receiver DOM 30 on string 11. The red curve is a Gaussian fitted to the leading edge as described in the text. The threshold of the leading edge where the red curve ends is shown by the dashed black line. The vertical dashed blue line indicates the prompt time determined from the Gaussian fit.

where μ and σ are the mean and the sigma of the Gaussian, and α is chosen as

$$\alpha = \sqrt{2\ln(100)} = 3.03, \tag{4.2}$$

which corresponds to 1% of the peak value of the Gaussian.

Some of the results are shown in figures 4.4 where the emitter DOMs are all on string 19 and the receiver DOMs are positioned on one of its 6 adjacent strings. In the pairs of plots which are shown side-by-side the receiving DOMs are the DOMs position above and below the emitting DOM on adjacent strings. It can be seen that the times obtained are different with the lower DOM (right hand plots) having longer times in each case. This is a consequence of the PMT detecting surface being in the lower part of the DOM and thus requires light scatter (probably in the hole ice) to receive light from a higher emitting DOM.

It can also be seen that the first actual hit photon always arrives after the prompt time determined from the Gaussian suggesting that there are no photons which arrive completely unscattered. This is not unexpected especially given the fact that hole is more scattering.

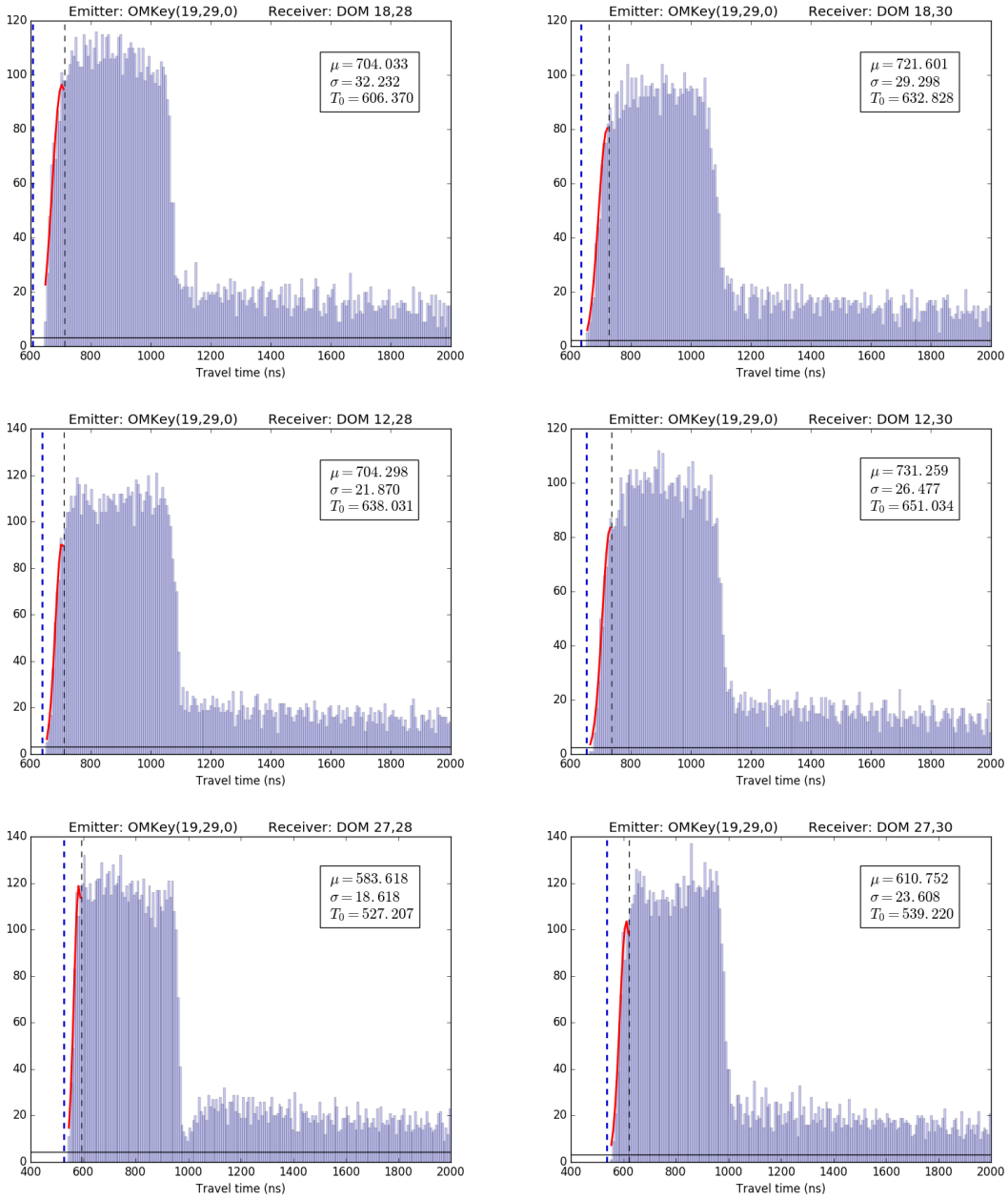

Figure 4.4: Light distribution of emitter-receiver pairs with fitted prompt time for these six pairs.The plots shown side-by-side are for receiver DOMs positioned above and below the emitter DOM. On each plot, the red curve represents the Gaussian fit to the leading edge of the photon distribution and the vertical dashed blue line indicates the calculated prompt time.

4.3 Photon Propagation Code (PPC)

In order to to use the flasher data set for calibration purposes we need to be able to compare simulation data with flasher data. The process is that the properties which are required to be determined, can be varied in the simulations until the best

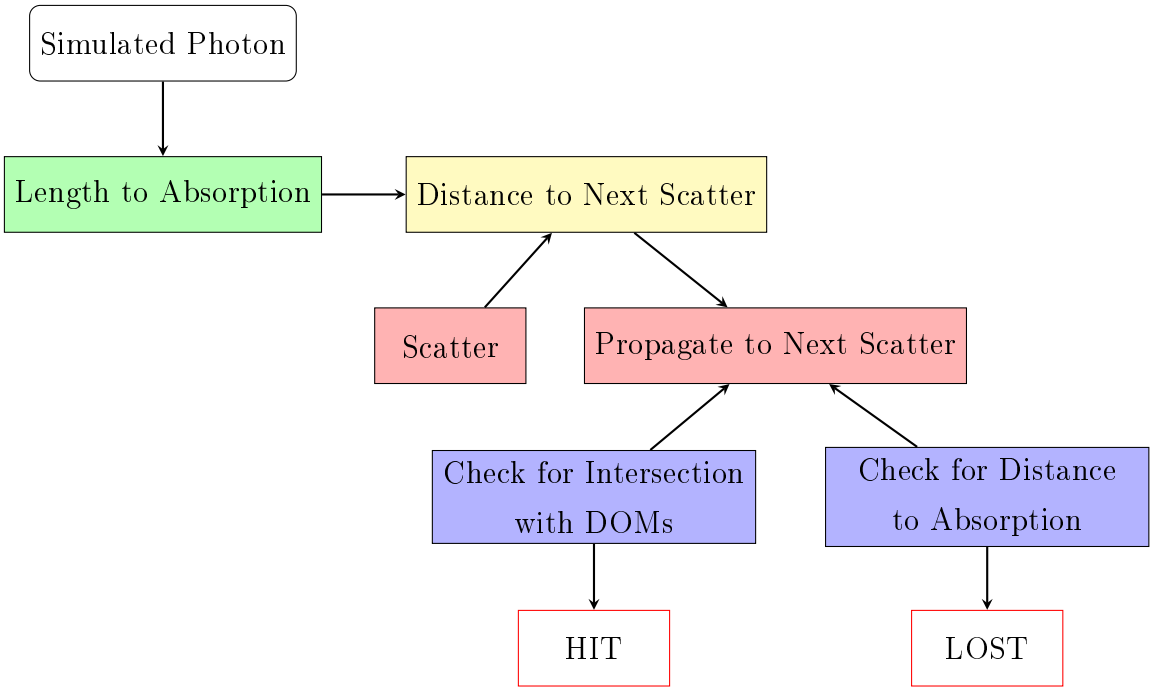

Figure 4.5: Photon life cycle as implemented for the photon propagation.

fit with the data is identified.

The central part of the simulation process for determining ice properties is the simulation of the photon propagation through the ice. The Photon Propagation Code(PPC) is the standard code used by IceCube for this purpose and is the code employed in this thesis. The PPC software was written by Dmitry Chirkin[97].

The PPC software is based on full first principle simulation which means that it tracks each photon individually. The propagation of the photon is simulated by considering absorption and scattering coefficients for whichever layer the photon is currently in. First the total absorption weight for a given photon is sampled from an exponential distribution with unity scale. The absorption weight determines the travel distance after which the photon will be deemed to have been absorbed. The same approach is used to determine the distance to the next scatter. Using the current photon direction, the photon is moved this distance to the next scattering point. For each layer, the length times the local absorption or scattering coefficient is subtracted from the current absorption or scattering weight. The photon is assumed to be deflected when the scattering weight reaches zero. The whole process is then repeated until the photon is either absorbed or the photon hits a receiver DOM. Figure 4.5 illustrates the life cycle of a photon as implemented for the *PPC*.

Scattering is simulated in *PPC* based on Mie scattering distributions through the superposition of analytic approximations of the Henyey-Greenstein (HG) [108] function as it is defined in 3.2.2.1 and Simplified-Liu (SL) parametrizations which

is defined as [109]

$$p(\cos\theta) \ \propto \ (1+\cos\theta)^{\alpha}, \tag{4.3}$$

where $\alpha = \frac{2g}{1-g}$ and g is the average scattering angle $g = <\cos\theta>$.

The superposition is given by a mixing parameter f_{SL} , which is fitted as part of the ice modeling, to be

$$p(\cos\theta) \ = \ (1-f_{SL}).HG(\cos\theta) + f_{SL}.SL(\cos\theta). \tag{4.4}$$

The ice anisotropy introduced in 3.5.5, and the tilted layers, discussed in 3.5.4, can also be taken into account using PPC.

Each individual photon can be tracked independently mainly because the trajectories of the photons are independent of each other. However, tracking all the emitted photons individually makes the computation a highly time extensive process. To tackle this problem and in order to achieve a higher speed computation an implementation of PPC is created that can be used on the GPU of a graphics card instead of CPU. That increases the calculations done by the code up to a factor of 250. In addition, an approximation called DOM oversizing has been also implemented where the DOMs are simulated to be up to 16 times as larger than their actual size. Oversizing, however, comes with a small timing bias. Moreover, to avoid unphysical shadowing effects the detected photons by a DOM should not be deleted from the simulation process.

Another software package that is also used to propagate photons is called Photonics. The principles of photonics are very similar however instead of being used in real-time with other simulation modules the light output is recorded in multidimensional tables which can be looked up in the simulation chain. PPC is now more widely used in simulation by IceCube but the photonics tables are still used for reconstruction purposes. The output from PPC and Photonics show good agreement which provides a verification check for the both codes.

4.4 Likelihood Statistic

As mentioned in the previous section, for most ice calibration purposes a comparison is done between flasher data and simulation data. A statistical criteria needs to be decided for defining the best fit between the simulation and flasher data. Dmitri Chirkin has developed a likelihood function for this purpose[110] which we briefly introduce here. Further details are given in section 6.1.

If total photon count in data is d obtained in n_d flasher events and the total photon count in simulation is s obtained in n_s simulated events then the expected rate of counts μ for data and simulation are

$$\mu_d = d/n_d, and \;\; \mu_s = s/n_s. \tag{4.5}$$

The likelihood function proposed by Dmitry Chrikin in [110] is given by

$$-\ln \mathcal{L} \;=\; \sum_i \left(s_i \ln \frac{s_i/n_s}{\mu_s^i} + d_i \ln \frac{d_i/n_d}{\mu_d^i} + \frac{1}{2\sigma^2} \ln^2 \frac{\mu_d^i}{\mu_s^i} \right), \tag{4.6}$$

where i represents the current bin of the light curve.
The light distribution of each emitter-receiver pair in both flasher data set and simulation events which are used in this thesis are binned using a Bayesian Blocking algorithm, where each bin is multiples of 25 ns long and contains approximately the same statistics as any other bin. This algorithm aggregates bins with small statistics and preserves details especially during rapid changes of the light distribution [111].

4.5 Determination of the DOM Orientation

In this section I present a study to determine the DOM orientation, or more specifically the azimuthal angle of a particular LED flasher on the flasher board in the DOM. If the azimuthal angle is known for one of the LEDs, then the angular position of all of the LEDs are known as their relative position on the board is known. The angle for the LED position is important for being able to use the flashers in ice calibration studies. This DOM orientation study was performed for string 79 as it carries 8 colour DOMs which are the DOMs in wavelength dependency studies, such as those presented in the next two chapters.

The data set which is used for the purpose of this study is the all purpose flasher set which was collected in early 2017. The operational flasher LEDs in this data set are all of the DOMs which are embedded on DeepCore Strings (ie: strings 36, 79, 80, 83, 85 and 85). The runs used were 129073, 129078, 129079, 129083 and 129084 as these were those relevant for string 79.

To determine the orientation of a DOM, the azimuth angle of the LED 7 on that DOM is fitted using the likelihood statistic introduced in the previous section. This was done by processing the raw data file which are in **.gz** format. A sequence of codes are applied, starting with the raw data file and an initial angle hypothesis as input, and eventually providing as output a single value that represents the likelihood value associated with the angle. The summary of the whole process, from the raw data to the final likelihood value is given in Appendix A. The basic process is that

simulation data is produced for the inputed angle, and the likelihood statistic is evaluated comparing the simulation data with the flasher data. The calculated final likelihood value is determined from the likelihood values for a number of different receivers.

For the likelihood evaluation an additional DOM noise rate of 500 Hz is also added to the function to include the plausible inaccuracy of the simulated detector response. Also to avoid having saturated PMTs, DOMs with a total charge larger than a threshold of 1000 PE are excluded from the likelihood calculation. In addition, after deriving the peak of light distribution curve of an emitter-receiver pair we only keep the bins within -500 ns to 1000 ns around the peak and the rest of the bins are being excluded from the likelihood calculation. The exclusion of the bins outside that range can decreases the effect of noise, muons and other physics events.

The flasher data set that is used was built upon multiple runs, however, each individual LED is associated to a unique sub-run. An example of a typical data table and the information that is stored in its cells is presented in table 4.1 for colour-DOM number 1 on string 79.

Run-ID	**Run**	**Sub-Run**	**Str**	**DOM**	**Brighness**	**Width (ns)**	**Delay (ns)**	**Mask**	**Rate (Hz)**
80496	129073	121	79	1	40	20	0	0040	10
80499	129073	123	79	1	40	20	0	0080	10
80502	129073	125	79	1	40	20	0	0100	10
80505	129073	127	79	1	40	20	0	0200	10
80508	129073	129	79	1	40	20	0	0400	10
80511	129073	131	79	1	40	20	0	0800	10
80514	129073	133	79	1	40	20	0	0fc0	10

Table 4.1: All-Purpose Flasher Data Set. Data table of the cDOM 01 on String 79.

The first column of table 4.1 simply contains an ID number that the run is labeled with. The second and third columns contain run and sub-run numbers as previously introduced, while the fourth and fifth column hold the string number and the DOM number respectively. The sixth column is the brightness, with all of these runs having a brightness of 40. The relationship between this number and the flasher output was given in equation 2.1. Width that can be seen in the seventh column refers to the window time between pulses which is 10 ns for all sub-runs here. The next column (ie: delay) indicates the amount of time between the LED

flash and the current pulse. It is assumed that there is no delay between the flash and the pulse but it was later realized that there is always a delay that needs to be taken into account for more sensitive analyses. This delay time is categorized under a term called "nuisance parameters" which is discussed with further details in section 5.3.

The last column in table 4.1, contains the information about the flasher LED. It is from this column that we can identify which LEDs are flashing. To interpret the "mask" variable we should know that the first 6 LEDs on a normal DOM are the tilted LEDs whereas the last 6 LEDs are the horizontal ones. In addition, the tilted and horizontal LEDs are paired in azimuth and the numbers increase in the clockwise direction with the flasher board viewed from above. When a flasher is configured for a run the individual LEDs are enabled with a 12-bit binary mask, where LED n is enabled with bit number $n-1$. The mask is typically expressed as a hexadecimal number, i.e. with a base of 16 and written with the symbols 0-9 and A-F. Therefore, we can easily identify the flashing LEDs by looking at its "mask" variable. Table 4.2 summarises the way the "mask" variable should be interpreted.

Mask (Hex)	**Mask Binary**	**Mask Decimal**	**Flasher LED(s)**
FFF	111111111111	4095	All 12 LEDs
FC0	111111000000	4032	The 6 horizontal LEDs
03F	000000111111	63	The 6 tilted LEDs
001	000000000001	1	LED 1
002	000000000010	2	LED 2
004	000000000100	4	LED 3
008	000000001000	8	LED 4
010	000000010000	16	LED 5
020	000000100000	32	LED 6
040	000001000000	64	LED 7
080	000010000000	128	LED 8
100	000100000000	256	LED 9
200	001000000000	512	LED 10
400	010000000000	1024	LED 11
800	100000000000	2048	LED 12
208	001000001000	520	LEDs 4 and 10

Table 4.2: Flasher LED mask indicates which LEDs are flashing.

Given that the aim is to determine the orientation of LED 7 the main mask which is used is that which corresponds to this LED flashing which is mask 0040. Some other masks have been also used as a cross-check to our final results.

The iterative fitting procedure is to start with an angle and then iterate over an entire circle of 360° with a constant step and register the calculated likelihood value for each step. This produces a set of numerical results from which the smallest value represents the best fit and corresponds to the best fit angle. The initial angle and the steps are chosen arbitrarily but by considering the systematic errors the whole process is repeated until the point where the difference between the minimum likelihood and the next smallest value is less than the standard deviation.

Figure 4.6 shows the initial results where angles between 0° and 360° with 15° increment is scanned through to determine the minimum likelihood. As it can be seen, the best angle based on this plot is around 75°. C-DOM number 1 on string 79 is one of the eight colour-DOMs on this string with their LED 7 emitting photons with 340 nm wavelength.

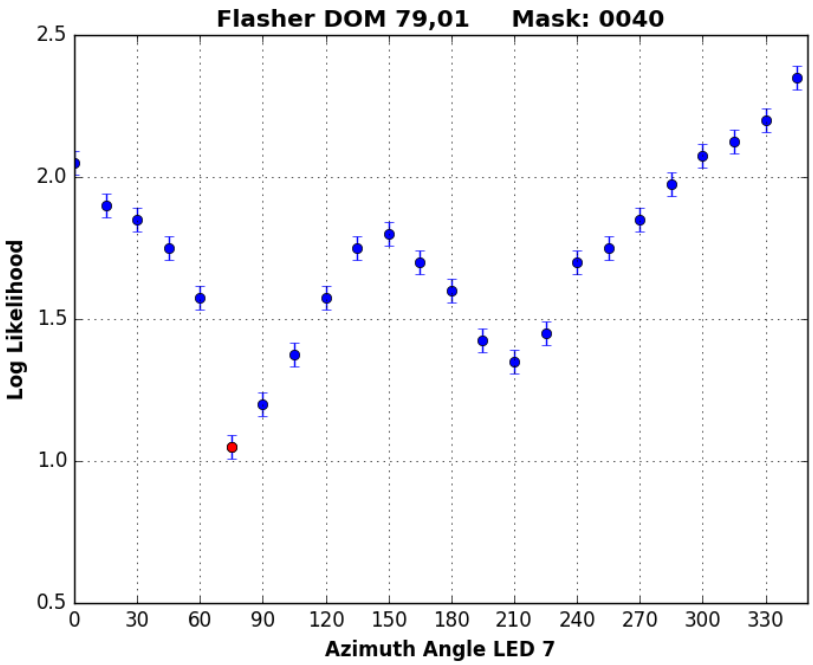

Figure 4.6: Likelihood as a function of angle for DOM 01 on String 79.

Figure 4.7 shows a finer scan for c-DOM 1 on string 79 with 5° azimuth angle interval. As it can be seen the best azimuth angle should lay around 72°. Finer scanning using the same method resulted to a value of 72.4° with the uncertainty of ±0.2 to be the best azimuth angle for LED 7 on DOM 79,01. As it was mentioned above, the reason for picking this uncertainty is that the difference between the

likelihood value associated with the angle of 72.4° and the one for the angle of 72.6° is less than the standard deviation of ≈ 0.0435. For a given angle, close to the best angle, the whole likelihood process was repeated several times and the standard deviation of all the output likelihood values was calculated. This is assumed to be a good representation of the systematic errors involved in this study. Final results for the azimuth angle of LED 7 for all colour-DOMs on string 79 are summarized in table 4.3.

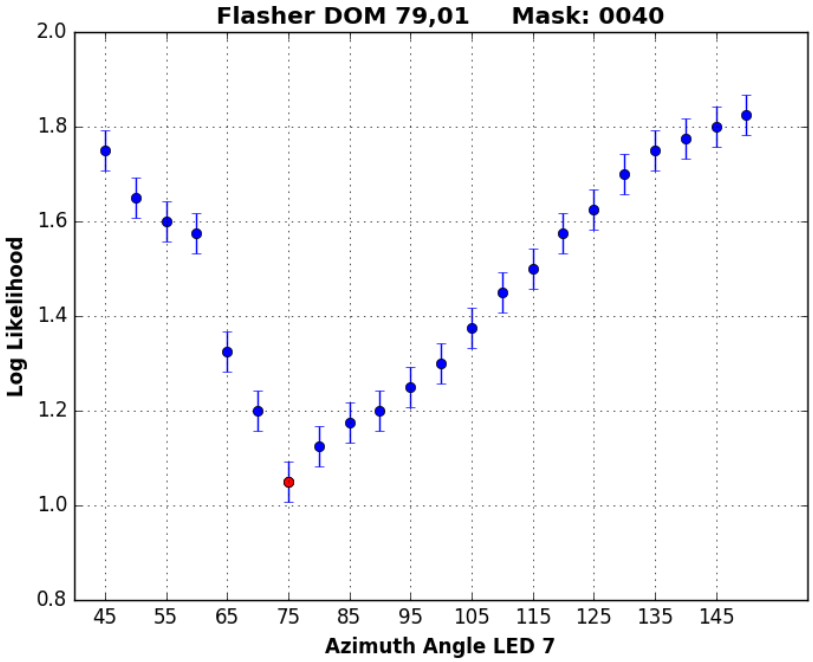

Figure 4.7: Likelihood as a function of angle for DOM 01 on String 79- 5° steps

DOM	X	Y	Z	Angle	Uncertainty
1	31.25	-72.93	188.29	72.4	±0.2
8	31.25	-72.93	118.21	76.5	±0.4
13	31.25	-72.93	-173.15	4.8	±0.9
22	31.25	-72.93	-236.22	257.0	±0.7
32	31.25	-72.93	-306.31	110.5	±0.8
41	31.25	-72.93	-369.39	191.4	±0.6
53	31.25	-72.93	-453.49	354.3	±0.8
60	31.25	-72.93	-503.42	0.5	±0.6

Table 4.3: Azimuth angle of LED 7 of all Colour-DOMs on String 79.

In addition to the rest of colour-DOMs, a number of normal DOMs on the same string have been also studied. The results of both type of DOMs will be used in determining the wavelength dependency of the ice parameters in chapter 6. The plot shown in figure 4.8 shows that the best angle for the LED 7 of the normal DOM 14 on string 79 with the 405 nm wavelength lays somewhere between 75° and 90°.

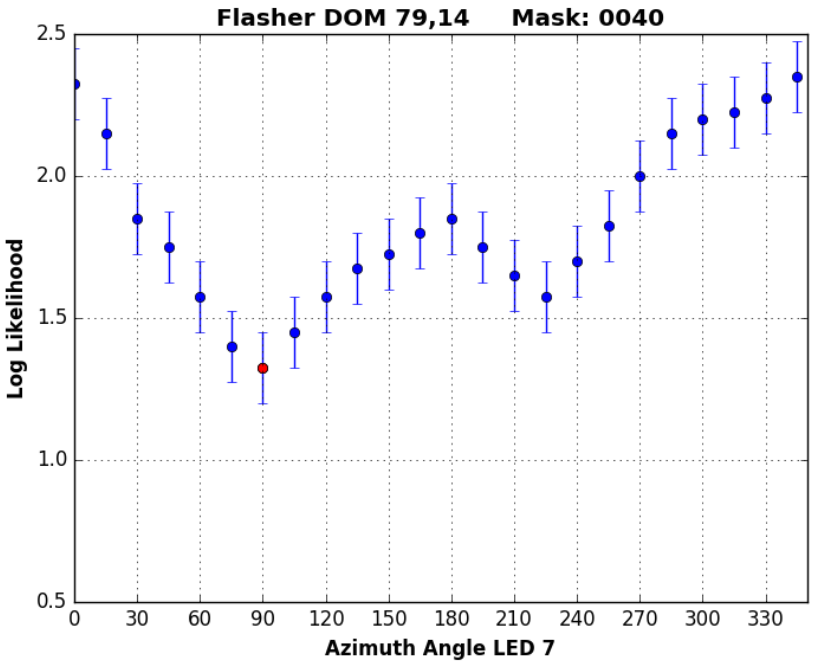

Figure 4.8: Likelihood as a function of angle for DOM 14 on String 79.

A total of eight standard DOMs on string 79 were also selected and the azimuth angle of their LED 7 determined through the same approach. The standard DOM analysis was performed as well as that for the colour DOMs as the standard DOMs were also needed for the studies presented in chapters 5 and 6. The standard DOMs were used as a cross-check to the extracted information from the colour-DOMs, and also in order to find the scattering and absorption coefficients at the standard wavelength of 405 nm.

DOM	X	Y	Z	Angle	Uncertainty
2	31.25	-72.93	178.28	16.6	±0.4
7	31.25	-72.93	128.22	304.5	±0.6
14	31.25	-72.93	-180.16	83.0	±0.8
21	31.25	-72.93	-229.22	305.0	±0.4
33	31.25	-72.93	-313.32	10.4	±0.7
40	31.25	-72.93	-362.38	340.0	±0.6
54	31.25	-72.93	-460.5	131.3	±0.8
59	31.25	-72.93	-495.54	80.5	±0.8

Table 4.4: Azimuth angle of LED 7 of 8 selected Normal-DOMs on String 79.

5 Wavelength Dependence of the Ice Optical Properties – Pilot Study

In this, and the next chapter, an investigation into the wavelength dependency of the ice absorption and scattering coefficients is described. As introduced in section 3.3, the optical properties of the ice are characterised by a six parameter model, where the wavelength dependency of scattering of the ice is given by

$$b_e(\lambda) = \left(\frac{\lambda}{400}\right)^{-\alpha} b_e(400), \tag{5.1}$$

while this dependency for the absorption can be expressed as

$$a(\lambda) = a_{dust}(\lambda) + Ae^{-B/\lambda}.(1 + 0.01.\delta\tau), \tag{5.2}$$

with

$$a_{dust}(\lambda) = a_{dust}(400).\left(\frac{\lambda}{400}\right)^{-\kappa}, \tag{5.3}$$

where the wavelength dependence is expressed through the exponents α and κ and 400 nm chosen as the reference wavelength. While α and κ are fixed to be depth *independent* in the ice modelling, the absorption and scattering coefficients values at 400 nm, $a_{dust}(400)$ and $b(400)$ are strongly depth dependent. In our study we used the most recent calibration data taken using the coloured flashers, to determine whether the current α and κ model values are optimal.

5.1 Analysis method

Our basic investigation method is that illustrated in figure 4.1 where we compare the photon arrival time distributions of the flasher data with those obtained with simulations, varying the parameters used in the simulation to determine the best-fitting parameters. For each of the four wavelengths available we sought the best fit pair of absorption and scattering coefficients. As our focus is on the wavelength dependence, we kept the depth dependency profile of these coefficients[1] fixed and scaled the $a(400)$ and $b(400)$ values at all depths by the same amount.

[1]See figures 3.8 and 3.6 to see the depth dependency profile of these coefficients

To determine the best-fit parameters, a test statistic quantity is needed which quantifies the goodness of fit of the simulation arrival time distribution to the flasher data distribution. In the DOM orientation study described in the previous chapter, we used the likelihood method developed by Dima Chirkin, which uses the quantity given by 4.6 to evaluate the goodness of fit. For our final determination of the wavelength dependence of the optical properties, which is described in the next chapter, we use this same function and the full likelihood machinery developed by Chirkin. However, before undertaking that study we performed a pilot study using a least-squares comparison where we performed the optimisation steps by hand. This allowed us to investigate the various issues involved in an IceCube flasher-simulation comparison. While the least-squares comparison was eventually abandoned, we describe this study in this chapter for completeness and because it allows us to discuss and illustrate the issues which need to be accounted for.

5.1.1 Data set and PPC settings

The flasher data set used for the wavelength dependency studies was taken in 2017 and 2018. There were 93733 flasher events recorded in this flasher set. Data was taken from several runs with brightness of 127 and width of 127 ns. Delay time was assumed to be zero and the rate of the runs was 3 Hz. Brightness, width, delay and rate are defined in the flasherboard description in section 2.2.

For our investigation, the PPC software was used to generate the simulation data for different ice model settings. In PPC there are two descriptions of angular acceptance, "nominal" and "hole-ice". The hole-ice setting increases the angular acceptance for the DOMs to account for the effect of the increased scattering that is expected to occur in the refrozen ice in the holes, without actually changing the ice properties themselves [112]. DOM oversizing was also implemented into the simulation which increases the surface area which in return decreases the total number of simulated photons. The number of simulated photons was kept constant at 1×10^{10}. The ice layer tilt, LEDs angular emission profile, major anisotropy, and wavelength of the flasher LED all were adjusted using the appropriate PPC settings.

The mean scattering angle $< \cos\theta >$ value of 0.95 was selected and the azimuth orientation of the flasher LED was set as an additional input to the *PPC*. Below the general format of a typical executable *PPC* command is given:

PPCTABLESDIR = ../[ice-model] FLDR=[azimuth angle] WFLA=[wavelength] FWID=[Angular Emission Profile] ./ppc [string] [dom] [number of photons]

For instance for LED 1 on DOM 22 on string 79 which is a colour-LED emitting

light at 505 nm and the angular emission profile of 4.7 and the azimuth angle of 257°, the executable *PPC* is written:

PPCTABLESDIR = ../ice-sp3.2.2 FLDR=257.082 WFLA=505 FWID=3.7 ./ppc 79 22 1e10,

where Spice 3.2.2 ice model is used and total number of 1×10^{10} photons is simulated.

5.1.2 Least-Square Statistic Expressions

In this pilot study a least-square statistic was used to evaluate the goodness of fit between the simulation data and the flasher data. Throughout all of the simulation and data comparisons in this chapter, and the next chapter, the areas under the simulation and data, photon time distribution curves, are fixed to be the same. That is, the comparison is a shape comparison as opposed to a comparison which compares the total number of detected photons, as predicted by simulation, and the total number actually detected.

Two different least square statistics were used. The first is

$$\chi^2_{\mathrm{1LS}} = \sum_{i=0}^{N} \frac{(\frac{d_i}{N_d} - \frac{a_i}{N_a})^2}{\frac{d_i}{N_d} + \frac{a_i}{N_a}} \tag{5.4}$$

where d_i and a_i are the number of data counts and the number of simulation counts in the i^{th} bin respectively, N_d is the total number of data counts[2], and N_a is the total number of simulation counts. The division of the number of bin counts by the total number performs the shape comparison. However it can be seen this is statistic is not the normal χ^2 statistic – in the case that $N_d = N_s$ the value of the statistic above would be a factor of $1/N_d$ of the value of the χ^2 statistic which would be evaluated for this data comparison.

The second least-square statistic has the form

$$\chi^2_{\mathrm{2LS}} = \sum_{i=0}^{N} \frac{(d_i - a_i.N_d/N_a)^2}{d_i + a_i.N_d^2/N_a^2}. \tag{5.5}$$

This statistic is closer to the normal χ^2 statistic as can be seen from its form when $N_d = N_s$. To account for systematic errors (discussed in section 6.4) 15% data error is added to the denominator of the above expressions when calculating the χ^2_{LS} values.

[2]As explained in the text the data photon arrival time distribution is a waveform which is obtained through data processing routines and is not a true histogram of counts, meaning that N_d needs to be derived with a somewhat reverse engineered approach.

In neither case can the statistic be viewed as a true χ^2 as the data photon arrival time distribution is a waveform which is obtained through data processing routines, which account for PMT response artefacts and is not a true histogram of counts.

For the evaluation of the goodness of fit for a single emitter-receiver pair, it is clear that both statistics will identify the same best fit as one statistic is approximately a multiple of the other. However when evaluating the goodness of fit for many emitter-receiver pairs, by summing the values of the statistic for each pair, the result can be different for the two options. This is because a given pair can have a greater or smaller relative contribution to the total depending on its total number of counts.

The first statistic given in equation 5.4 is referred to as the *normalised* value in the plots in this chapter. Although we emphasise, again, that for both statistics, the distribution which are compared, are normalised to have the same area and that only shape comparison are done.

5.1.3 Ice Model Version Selection

Before performing the study to determine the wavelength dependency of the scattering and absorption coefficients, an investigation of the performance of the most recent ice models for the colour DOMs was undertaken. The two most recent Spice model[3] versions, Spice 3.2-t and Spice 3.2.2, were used in simulation. The difference between Spice 3.2-t and Spice 3.2.2 is that unlike Spice 3.2-t the major anisotropy explained in 3.5.5 is included in Spice 3.2.2. Furthermore for each of these two ice models we choose two different options for the angular emission profile of the Flasher LEDs. Our motivation is to check the variation in goodness of fit between these different ice models when used with Colour DOM flasher data as compared with standard flasher data.

The angular emission profile of each LED has a Gaussian component with a standard deviation of approximately 13° for a standard LED with a 405 nm wavelength [113] but as discussed in section 2.3 the standard deviation depends on the wavelengths of the emitted light. Table 5.1 summarises the values of the angular emission profile corresponding to each wavelength. To investigate the magnitude of the effect of the angular emission, simulations were performed with the tabulated standard deviation for a given wavelength and also using the 405 nm value of 13°.

[3]The Spice ice models were introduced in 3.4

Wavelength (nm)	Angular Emission Profile	LED Numbers
340	39.4	7, 9, 11
370	41.0	8, 10, 12
405	10.5	all horizontal LEDs
405	9.2	all tilted LEDs
450	5.0	2, 4, 6
505	4.7	1, 3, 5

Table 5.1: Angular emission profiles of all sets of LEDs with different wavelengths.

Figure 5.1 illustrates the light distribution for the emitter DOM 22 on string 79 where only its LED 1 was functional and the receiver DOM is on the adjacent string 80. The red curve shows the simulation distribution and the green curve represents the actual data distibution. As can be seen by eye the data and the simulations are normalised to have the same area facilitating, and only allowing, a shape comparison as discussed above.

The distance between the emitter-receiver pair is annotated on the plot, where the negative and positive values of the distance indicates whether the receiving DOM is below or above the emitter DOM respectively.

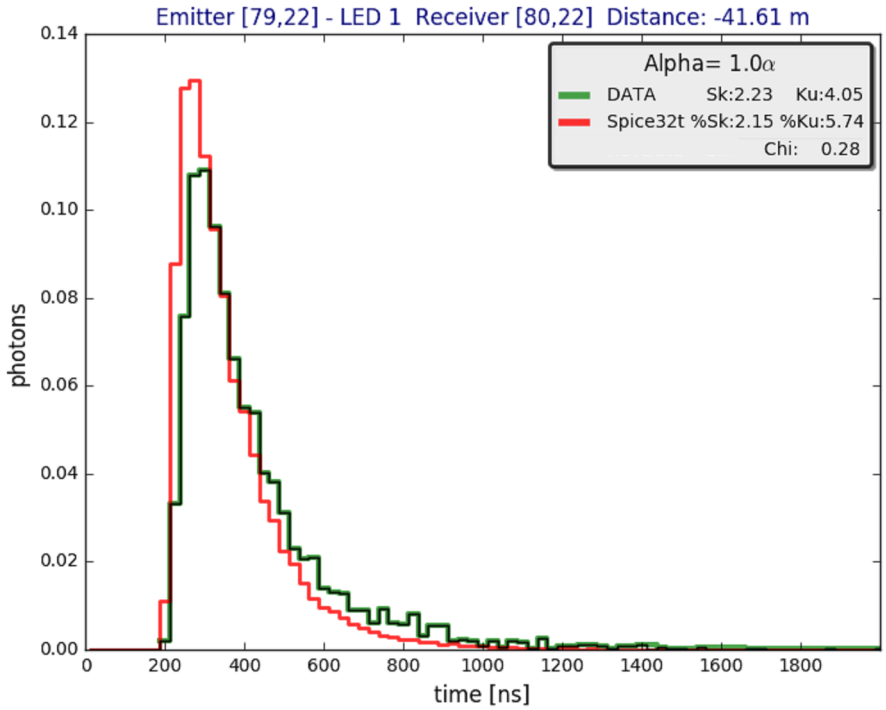

Figure 5.1: The light distribution of the LED 1 on c-DOM 79,22 emitting light peaked at 505 nm.

Figure 5.2 and 5.3 show the light distributions of LED 1 and LED 7 both on

DOM 22 of string 79. The receiver DOMs are chosen arbitrarily from the large number of possible receivers to be DOM 36, 43 and DOM 27, 46. These two are shown here merely as two examples of the final results that have been obtained by performing the least-square method. The χ^2_{1LS}/DOF and χ^2_{2LS}/DOF values are given (the former is referred to as *normalised*), along with the mutual distance of the emitter-receiver pairs as well as the amount of received light in photo-electron unit are shown next to their corresponding light distributions.

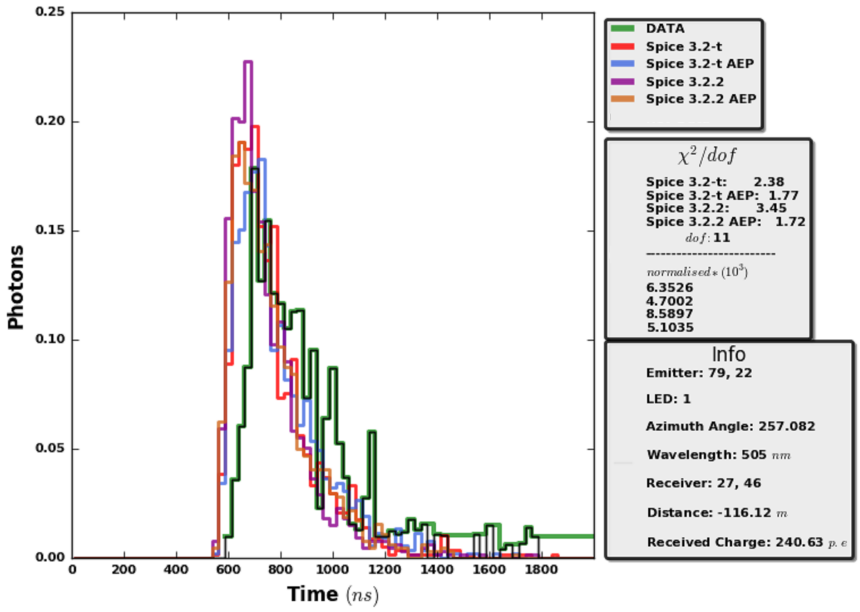

Figure 5.2: The photon arrival distribution for simulation and data for LED 1 on c-DOM 79,22, wavelength peak at 505 nm, and receiving DOM 36, 43. Various simulations are performed as described in the text and the corresponding colour of the curves are given in the legend. χ^2/dof values given in the adjacent box.

The same process which was performed to produce the figures 5.2 and 5.3 was performed again for all individual LEDs on c-DOM 22 on string 79. The mean value of all the calculated χ^2/dof for all of these DOMs was determined and is displayed for the alternative ice models in figure 5.4. As a reminder, LEDs 1,3 and 5 are the 505 nm peaked LEDs, 2,4 and 6 are the 470 nm peaked LEDs, 7,9, 11 are the 370 nm peaked LEDs and 8,10, 12 are the 340 nm peaked LEDs. LED n and LED $n+6$ are in the same position on the flasher board.

It can be seen that spice 3.2.2, in general, provides the best data-simulation fit for the various wavelength flashers. There are a few exceptions which can be seen in the bar-chart plots, where spice 3.2-t shows lower values of the fitting statistic. However, given the differences are not large and other verification studies, performed

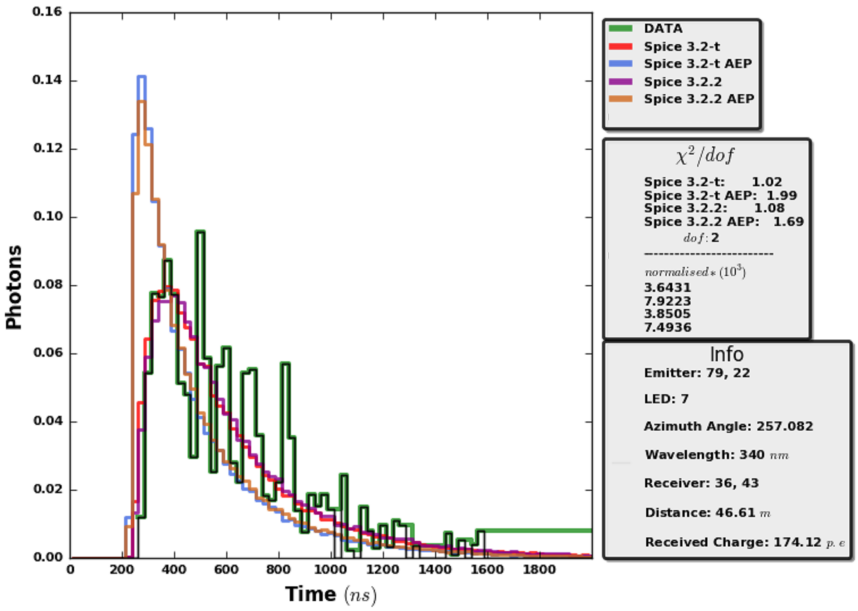

Figure 5.3: The photon arrival distribution for simulation and data for LED 7 on c-DOM 79,22 wavelength peak at 340 nm and receiving DOM 27, 46. Various simulations are performed as described in the text and the corresponding colour of the curves are given in the legend. χ^2/dof values given in the adjacent box.

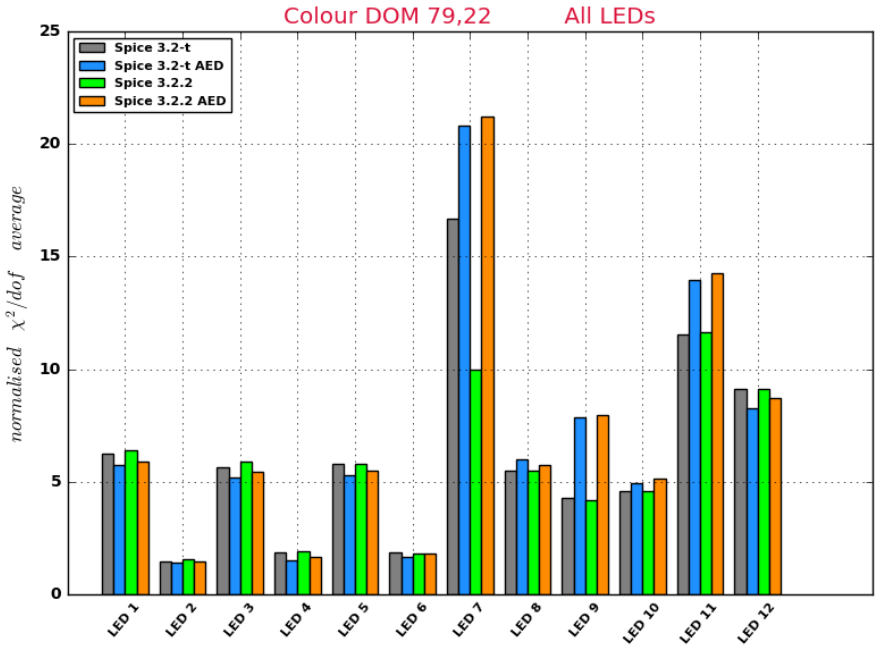

Figure 5.4: Average χ^2/dof using alternative ice models- all computed for emitter DOM 79,22, all LEDs.

within the IceCube collaboration, have shown the suitability of spice 3.2.2 it was decided there was no reason to doubt its suitability for the coloured wavelength investigations.

It can be seen from the bar graphs that the three LEDS with the same wavelength (1,3,5), (2,4,6), (7,9,11) and (8,10,12) have similar fits. It is somewhat noticeable that the shorter wavelength LEDS 7–12 have a somewhat worse fit. To look at this more figure 5.5 and figure 5.6 were produced. These show the same bar as in figure 5.4 but are split into LEDs 1–6 and LEDs 7–12. The difference between the derived χ_2/dof for the first six LEDs, where the wavelength peaks of the in-situ light are either at 450 nm or 505 nm, and the last six LEDs with wavelengths peaks of the at 370 nm and 340 nm, was found to be mainly due to the fact that the time offset (see next subsection) matched better for the longer wavelength LEDs.

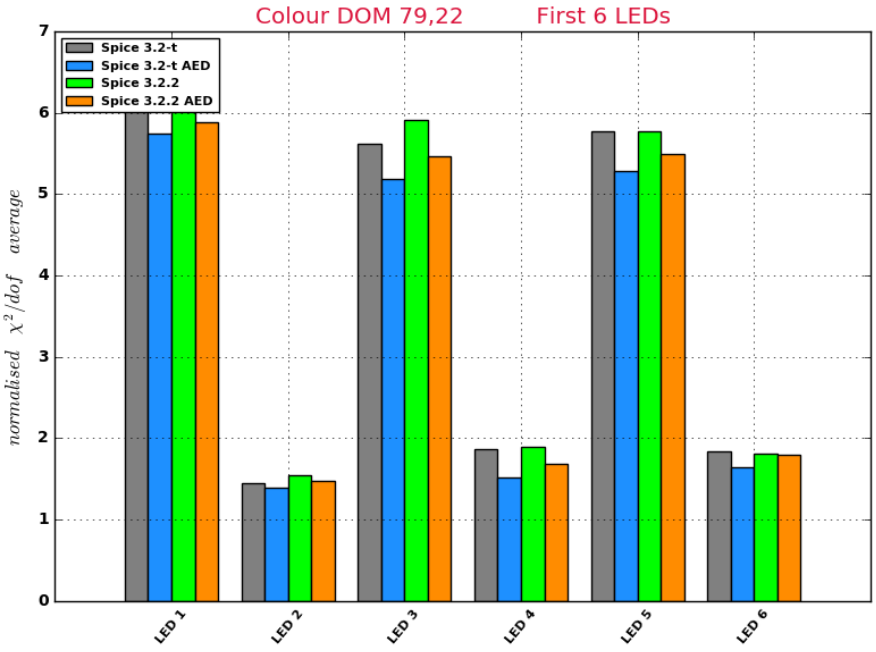

Figure 5.5: Average χ^2/dof using alternative ice models- all computed for emitter DOM 79,22, LEDs 1 to 6.

Moreover, the same study with other DOMs showed that although not exactly the same for each emitter DOM, the overall patterns remains the same thoroughly regardless of the emitter DOM or emitter LED. Table 5.2 summarises the average χ^2/dof values calculated for two more c-DOMs on string 79.

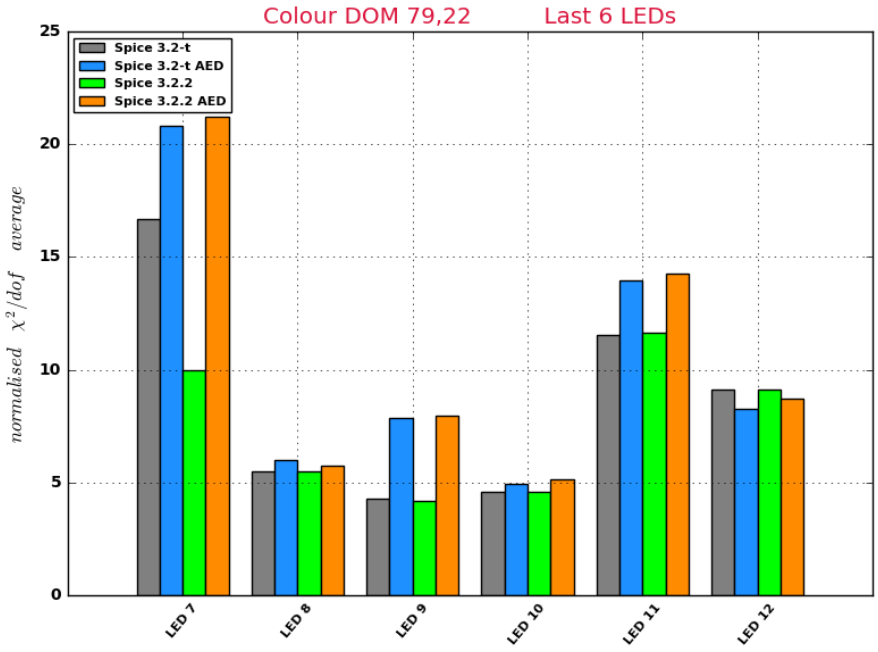

Figure 5.6: Average χ^2/dof using alternative ice models- all computed for emitter DOM 79,22, LEDs 7 to 12.

5.1.4 Time offset

At the outset of this investigation it was assumed that the flasher offset time was accounted for in the waveform data processing steps. If this was the case, the leading edge of the simulated and data waveforms should be aligned. However it became apparent that the offset for each flasher LED is different and this offset should be fitted as part of the iterative procedure to find the best fit ice properties. The fact that the machinery for doing this was available in the likelihood analysis package devloped by Dmitry Chrikin was one of the motivations for moving from the pilot study approach, to the likelihood approach described in the next chapter. Given that the timing offset has not been accounted for, the results presented in this chapter can only be taken as illustrative of the approach. While the results themselves can't be taken as definitive, this pilot study allowed an investigation and an understanding of the factors which need to be accounted for in ice calibration studies. An investigation into the flasher time offset is presented in section 5.3.1.

5.1.5 Iterative Procedure for Ice Property Analysis

As discussed Spice 3.2.2 is used for the ice property analysis. A file called *ice-model.dat* contains the main ice property parameters tabulated by depth layer, in four columns containg the depth of the centre of the layer, $b_e(400)$, $a_{dust}(400)$ and

LED	DOM 79,08				DOM 79,32			
	Spice 3.2-t	Spice 3.2-t AED	Spice 3.2.2	Spice 3.2.2 AED	Spice 3.2-t	Spice 3.2-t AED	Spice 3.2.2	Spice 3.2.2 AED
LED 7	12.4	11.7	11.7	11.4	23.3	22.0	17.4	15.8
LED 8	11.8	11.4	11.4	10.9	20.7	21.2	20.4	17.8
LED 9	12.9	12.7	12.2	12.2	21.4	21.0	17.6	17.2
LED 10	10.4	9.8	9.5	9.7	23.5	22.2	21.4	20.8
LED 11	14.2	14.1	12.4	11.7	22.0	17.4	14.7	12.6
LED 12	10.8	10.8	8.4	8.4	24.3	24.3	21.4	21.4
LED 1	8.2	8.2	6.4	6.4	13.2	12.1	9.4	9.2
LED 2	9.2	9.3	8.8	8.7	12.3	12.2	11.4	10.8
LED 3	8.4	8.4	7.2	7.2	12.8	12.0	11.8	11.8
LED 4	9.0	8.8	8.8	8.3	12.3	12.1	10.7	10.2
LED 5	8.4	8.4	6.4	6.0	10.2	10.0	8.3	8.3
LED 6	9.2	9.2	8.8	8.8	10.7	9.7	8.4	8.8

Table 5.2: The average χ^2/dof values calculated for two different DOMs on string 79.

$\delta\tau$ (as defined in section 3.3). This file may contain 2 additional optional columns: the major anisotropy coefficients $k1$ and $k2$ as discussed in section 3.5.5. These coefficients then can be calculated for other wavelengths by using equations 5.1 to and 5.3.

In addition to *icemodel.dat* file, each ice model directory contains several other files that are together called "the configuration files" [114]. The most important of these files which are used in almost all analyses are described in Appendix B.

For the purpose of this thesis, the tabulated values of the scattering and absorption coefficients are scaled separately by multiplying the currently used values by a constant for all rows in the *icemodel.dat* file. In other words, all the values of the scattering coefficients of the standard wavelength are either scaled up or down in every single ice layer.

PPC software was then used to generate the simulation files corresponding to these altered ice parameters. The least-square comparison test is performed to examine the goodness of fit by comparing the generated simulation to the flasher data. It was decided to alter the scattering coefficients from 20% to 300% of their current values meaning that all $b_e(400)$ are multiplied by a constant between 0.2 to 3.0 with a 0.2 interval between each step. The same alteration was performed on the absorption coefficients where all $a_{dust}(400)$ are multiplied by a constant in a range of 0.2 to 5.8 this time with 0.8 intervals. These range have been chosen arbitrarily aiming to cover a range of different values. Further scanning and fine tuning can be conducted based on the extracted results after performing the first scan.

5.2 Ice Property Analysis and Results

Figure 5.7 shows eight plots where in each plot the absorption coefficient is altered from 0.2 to 5.8 (starting from the top left) for the LED 1 on colour-DOM 79,22 emitting light at 505 nm while the scattering coefficient remained untouched. All 8 plots are of a single adjacent receiver DOM 84,14 which is approximately 68 m away from the emitter DOM. It can be seen that lower absorption coefficients result in smaller least-square values that might indicate that lower absorption coefficient needs to be considered at least for the wavelengths higher than the standard wavelength of 400 nm.

Figure 5.8 shows the plots of similar emitter-receiver pairs that are shown in 5.7 where in each plot the scattering coefficient is altered from 0.2 to 3.0 (starting from the top left) for the LED 1 on colour-DOM 79,22 emitting light at 505 nm while the absorption coefficient remained untouched. It can be seen that unlike the absorption plots, these plots show that as the scattering coefficient increases the least-square statistic value is getting smaller which may indicate that a larger scattering coefficient needs to be considered at least for the wavelengths higher than the standard wavelength of 400 nm.

These plots and their corresponding computed least-square statistic values are representing a single case where a single wavelength on a particular DOM was tested. In order to be able to draw more reliable conclusions, all emitter LEDs of that particular c-DOM 79,22 were studied. In addition, for any given emitter LED the least-square statistic values were computed for all receiver DOMs with sufficient observe charge to be able to do calculate a meaningful least-square statistic. The charge threshold is that at least 2000 p.e needed to be recorded for that emitter-receiver pair to be included in the study. This does mean that the receivers that are far from the emitter, will be removed, however it was noticed that there was always a number of further away receivers that did receive enough charge to be included in the study. This is advantageous because although by removing those emitters we avoid dealing with cases with low statistics it is advantageous for ice property studies to have some longer travel distances.

Figure 5.9 shows two dimensional histograms where the horizontal axis displays the factors that are used for scaling the scattering coefficient and the vertical axis those that are used for scaling the absorption coefficient. Each cell in this plot shows the average of all the computed chi-square values collected from all receiver DOMs that met the charge threshold criteria.

Once again it can be seen from this plot that larger scattering and smaller ab-

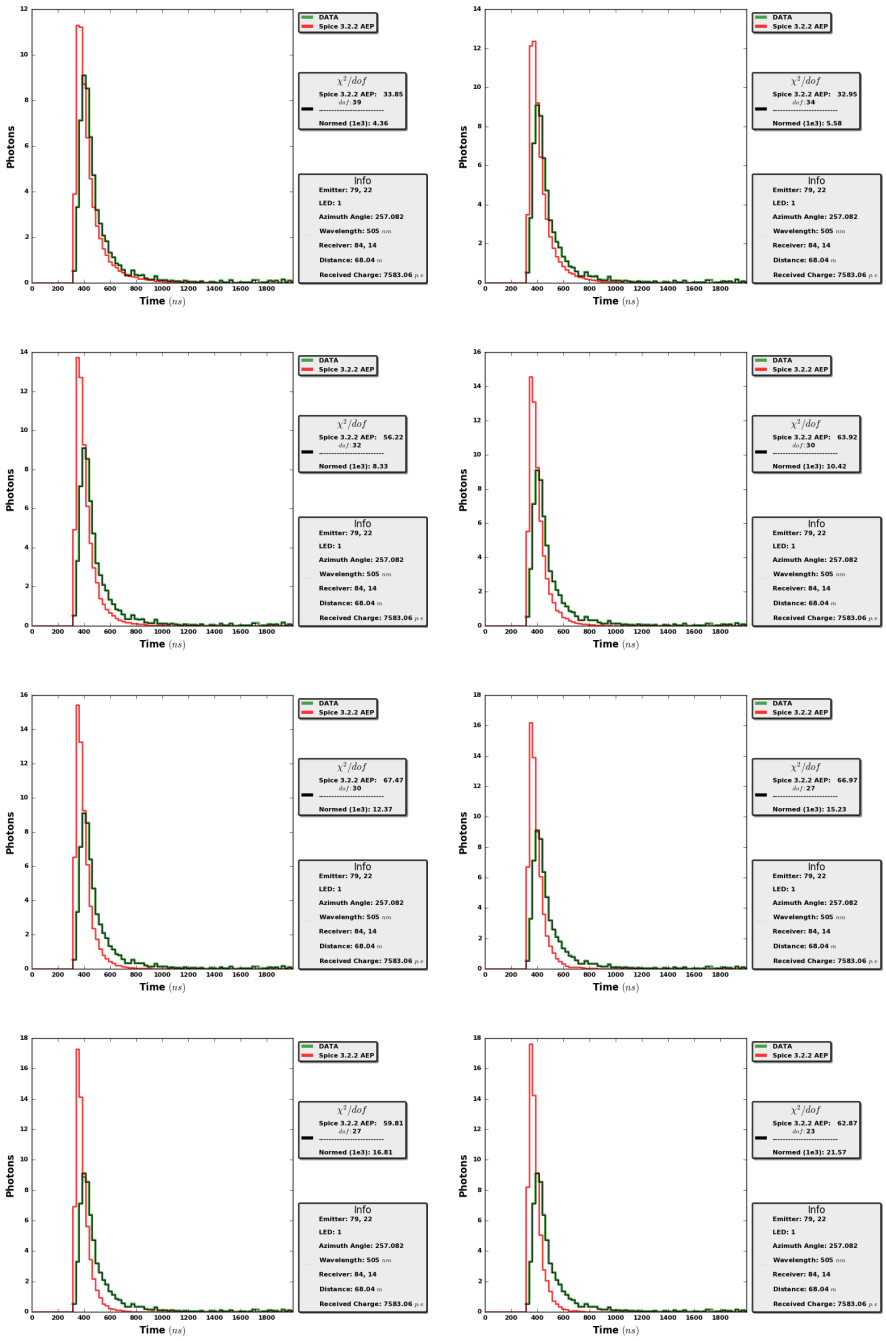

Figure 5.7: Light distribution of a given emitter-receiver pair with alternative absorption coefficients. Emitter is c-DOM 79,22 and Receiver is DOM 84,14

sorption coefficients are correlated to the smaller χ^2/dof value and consequently to the better fits.

The same scanning process was performed for the rest of LEDs on DOM 79,22 as well as all LEDs embedded on the rest of colour-DOMs on string 79. LEDs 1, 3 and 5 that have the same wavelength of 505 nm. Analysing the results obtained from all these LEDs indicates that in general a higher scattering and a lower (or equal to the standard one) absorption coefficient were required to reach the best fit.

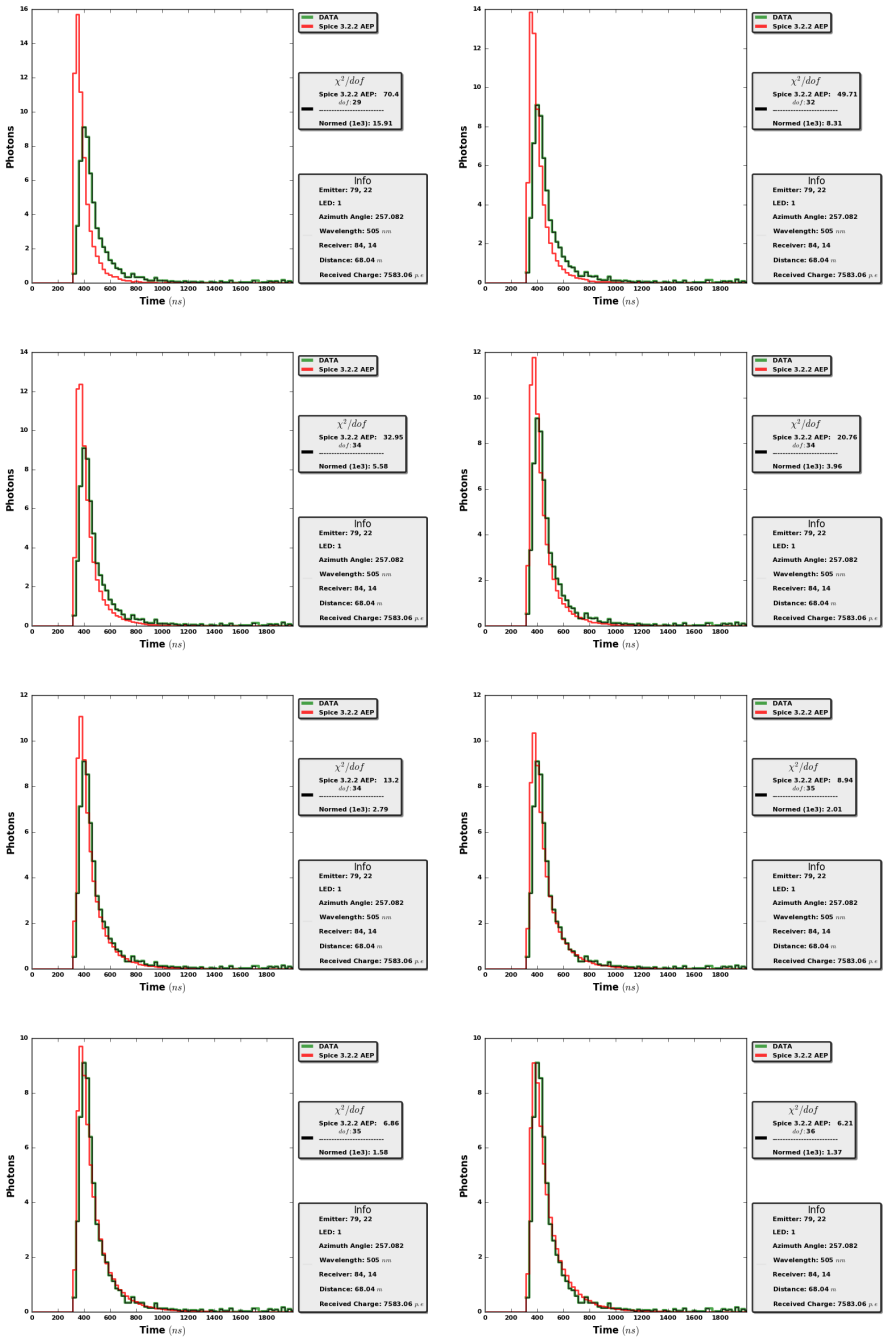

Figure 5.8: Light distribution of a given emitter-receiver pair with alternative scattering coefficients. Emitter is c-DOM 79,22 and Receiver is DOM 84,14

The same studies for other colour-DOMs on string 79 shows that regardless of the depth where the emitter DOM is deployed, larger scattering and smaller absorption coefficients always tend to result to the better fits. However, a small level of wavelength dependency is observed through examining LEDs with alternative wavelengths. Table 5.3 summarises the results of all LEDs for two colour-DOMs on string 79. However we once again comment that these results are really only indicative of the procedure as the time offset fitting needs to be included to obtain

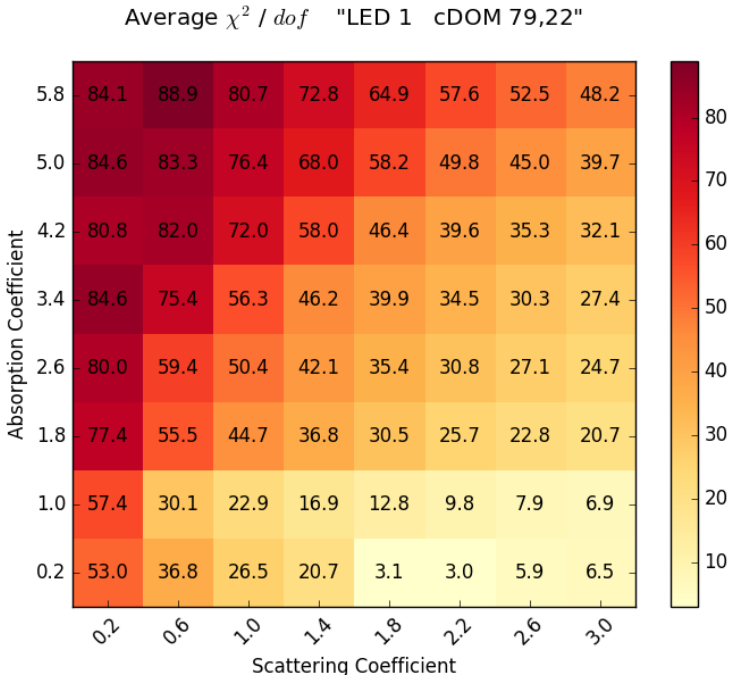

Figure 5.9: 2d histogram of mean χ^2/dof values. Emitter LED 1, DOM 7922, All receiver DOMs.

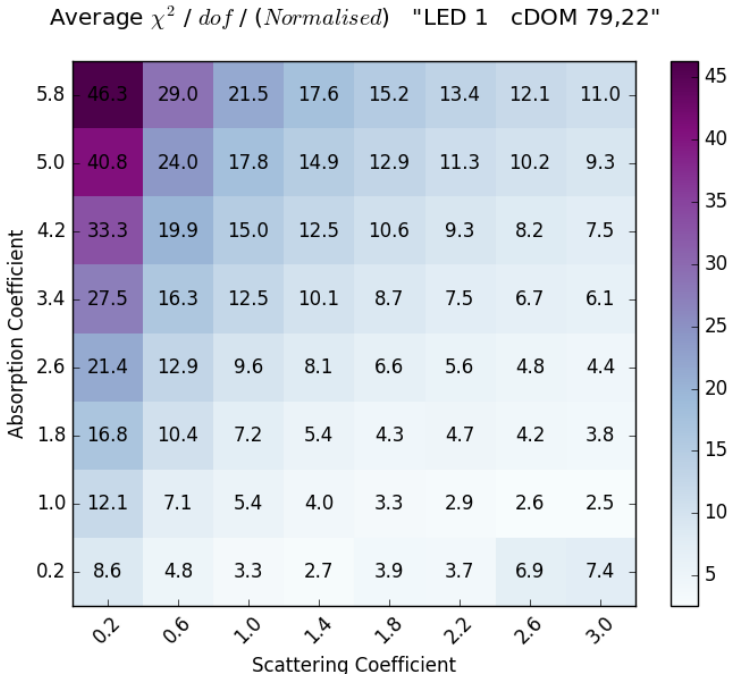

Figure 5.10: 2d histogram of mean χ^2 values. Emitter LED 1, DOM 7922, All receiver DOMs. All seeded histograms are normalised.

robust results.

The fact that in order for the least-square test to be applicable we need to remove the bins with low statistics leads to end up with many pairs in which the number of

		DOM 79,08		DOM 79,22	
Wavelength(λ)	**LED**	**Scattering Coefficient**	**Absorption Coefficient**	**Scattering Coefficient**	**Absorption Coefficient**
505 nm	LED 1	1.8-3.0	0.2-1.0	1.8-3.0	0.2-1.0
	LED 3	1.8-3.0	0.2-1.0	1.8-3.0	0.2-1.0
	LED 5	1.8-3.0	0.2-1.0	1.8-3.0	0.2-1.0
450 nm	LED 2	1.4-3.0	1.0	1.4-3.0	1.0
	LED 4	1.4-3.0	1.0	1.4-3.0	1.0
	LED 6	1.4-3.0	1.0	1.4-3.0	0.2-1.0
370 nm	LED 8	1.4-3.0	1.0	1.4-3.0	1.0
	LED 10	1.8-3.0	1.0	1.8-3.0	1.0
	LED 12	1.8-3.0	1.0	1.8-3.0	1.0
340 nm	LED 7	1.8-3.0	0.2-1.0	1.8-3.0	0.2-1.0
	LED 9	1.8-3.0	0.2-1.0	1.8-3.0	0.2-1.0
	LED 11	1.8-3.0	0.2-1.0	1.8-3.0	0.2-1.0

Table 5.3: Best scattering and absorption factors for two colour-DOMs- Multiple wavelengths.

remaining bins (i.e: degrees of freedom) is too small, consequently puts a negative constraint on our final results hence the overall conclusion that can be made upon that will be biased. For instance, in figure 5.11 where a typical light distribution plot of LED 1 emitting light at 505 nm is shown, the number of bins that is taken into account for computing the least-squares statistic value is 9 where the total number of bins is 200 meaning that less than 5% of the actual bins are accounted for. In figure 5.11 for instance the black rectangle shows the bins that our calculation was limited to. A better approach is the Bayesian blocking algorithm which combines bins with low counts. An investigation into using this method with the least square analysis but it was decided that using the likelihood framework developed by Chirkin would be the best option. The motivation for using the likelihood approach are discussed in the next section.

5.3 Motivation for Using Chirkin's Likelihood Machinery

In performing the pilot study, a number of issues were identified. These will be recapped in this section. Routines for addressing these issues have been developed and incorporated into a set of routines by Dima Chirkin. A central part of Chirkin's machinery is a likelihood statistic developed by Chrikin and argued to be more appropriate than the least-square type statistics. Although, the likelihood statistic

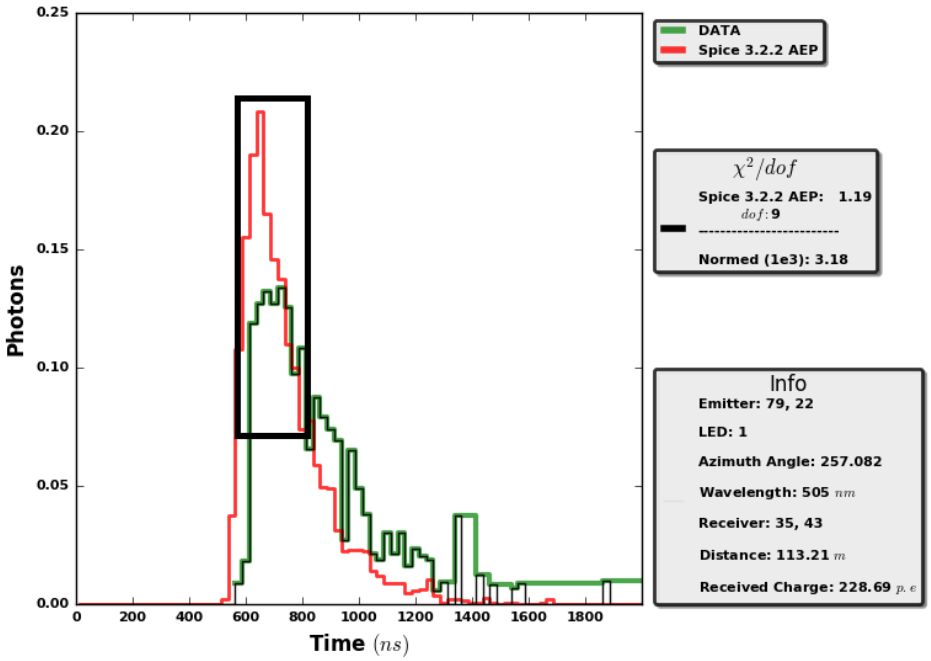

Figure 5.11: A cut is shown for a low statistics light distribution where the number of bins with enough counts is 9.

is a key aspect of Chirkin's approach, many of the advantageous features incorporated into the machinery are somewhat independent of the statistic used to evaluate goodness of fit.

A least-square type statistic requires bins with high statistics to be useful, however, as dicussed above, removing the bins with low statistics from the sample can lead to only the central part of the photon distibution being used in the comparison. Bayesian blocking is an alternative method used in statistics to optimize the number and size of bins used. Bayesian blocking is particularly useful when there are a large number of bins with low statistics [115]. The Bayesian blocking method implements bin aggregation where neighbouring are merged to produce a new histogram with each bin having similar statistics. In Chirkin's implementation of Bayesian blocking the binning is fixed based on the experimental data and then the same binning is applied to the simulation data.

Nuisance parameters also need to be accounted for. These are DOM or LED specific qualities which need to be determined for each DOM individually. Examples include the global time offset, the total photon yield, the LED's angular emission profile and the azimuthal position of the flasher LEDs.

Both LED azimuth orientation and LED angular emission profiles are accounted for in our analyses in this thesis. The LED azimuth orientation was unknown prior

to 2018 but this parameter was invesigated thoroughly in this research project, as described in section 4.5. In addition, the angular emission profile, as discussed in 2.3, should be also taken into account. This is because although the LED flashers emit light that is almost isotropic at large distances the effect of angular emission profile remains visible at smaller distances. The angular emission profile was incorporated in the simulation for this work.

The LED intensities are not well known. To overcome this problem and make the fit independent of the total LED intensities, the simulation should be repeated with variation of input photon numbers until the total number of photons matches the same number measured in data. This is implemented in the Chirkin approach. DOM specific nuisance parameters are the relative detection efficiencies and the hole ice modified angular acceptance as discussed in 3.5.2 and 3.5.1 respectively [116].

As mentioned above one of the nuisance parameters which is essential to determine is the time offset. An investigation of the time offset was undertaken within the least-squares analysis which made clear that this quantitiy should be fitted as part of the location of the minimisation of the fit comparison statistic. Again a procedure for doing this for any nuisance parameters is built into the Chirkin machinery. A description of the time offset invesitgation is given below.

5.3.1 Time Offset investigation

The global time offset is defined as the time between the instance of light emission and the current pulse. This offset can be measured by DOM calibration procedures which is done by aligning the leading edges of ATWD and FADC. The DOM calibrator reads in this value and applies the shift to FADC wave-forms [117]. The offset that is observed is assumed to be connected to differences between the DOMcal procedure and the way real data is handled. It is apparent from our analysis that the time-offsets used in simulation are not accurate enough and each LED on each individual DOM has its unique offset that needs to be carefully accounted for.

Figure 5.12 shows a given emitter-receiver pair with 4 different time-offsets applied to the all-purpose flasher data. It can be seen that by changing the time-offset the data curve is shifting either to the right or left as expected. In this case the time offset of 15 ns should be selected as it results in the lowest χ^2/dof value. We can see from figure 5.8 that altering of the scattering coefficient also causes the simulation curve to shift. It is therefore clear that best time-offset should be extracted in parallel with determining the best-fit scattering coefficient factor. Figure 5.13 demonstrates the results of an attempt to scan through the time-offset and scattering coefficient factors for LED 1 on c-DOM 79,22. The best time-offset is 15 ns

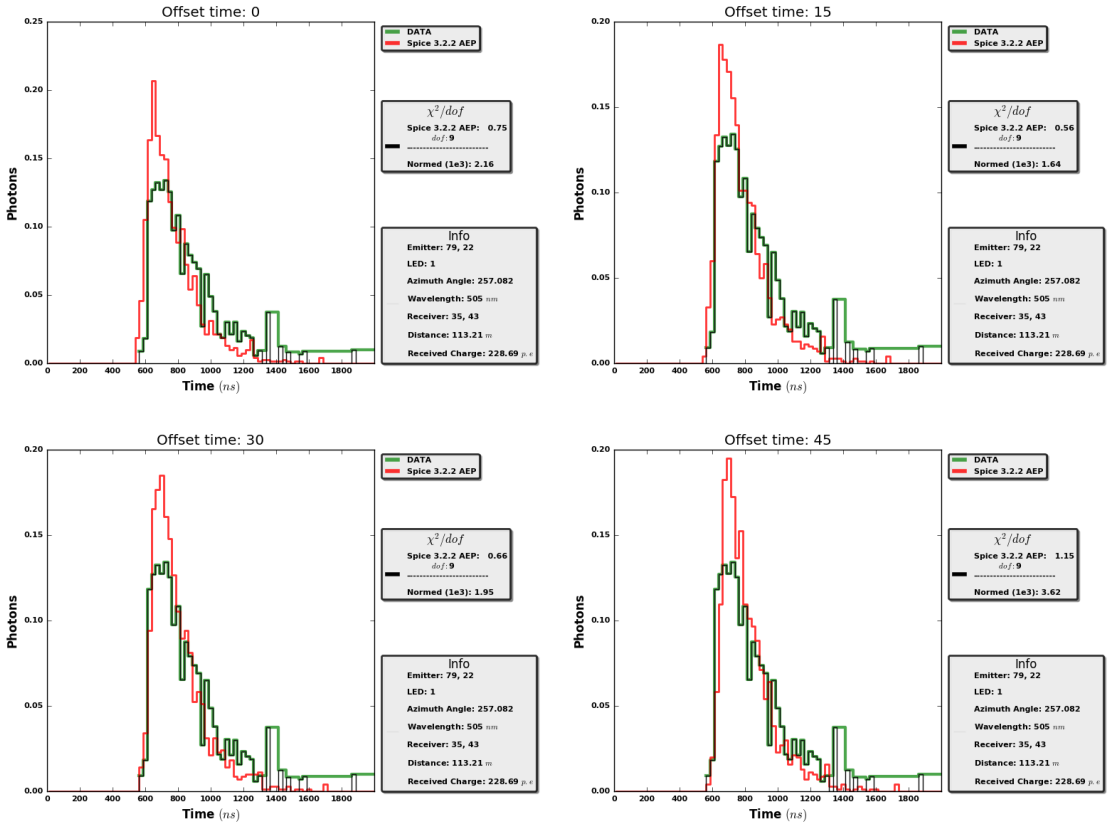

Figure 5.12: χ^2 values for emitter c-DOM 79,22 and receiver DOM 35,43 with four different time-offsets. LED 1 is flashing with λ= 505nm.

when the scattering coefficients are 40% scaled up.

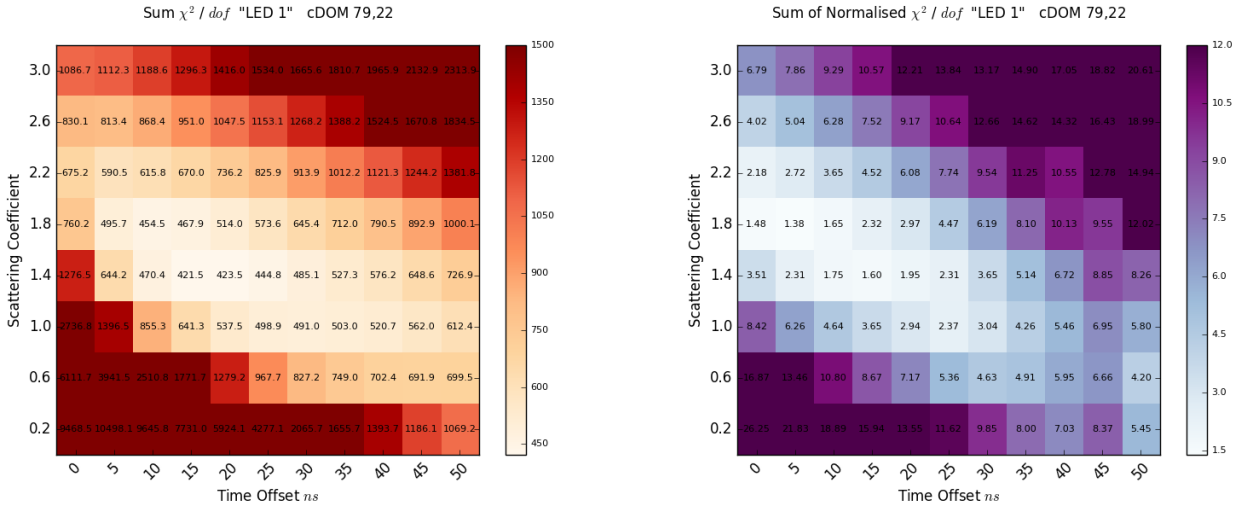

Figure 5.13: Two dimensional scanning of time-offset vs. scattering coefficient factors. LED 1 on DOM 79,22.

6 Determination of the Wavelength Dependence of the Ice Optical Properties

---

In this chapter we present the final study performed for determining the wavelength dependency of the optical properties of the ice in which IceCube is embedded. The goal of our study is determination of the α and κ values, which parameterise the wavelength dependence of the absorption and scattering, as described in section 3.3. The study presented in this chapter builds on the pilot study presented in the previous chapter, but uses the likelihood machinery developed by Dmitry Chirkin. As mentioned in the previous chapter, Chirkin's routines include capacity to implement Bayesian blocking and to determine nuisance parameters such as the time offset. The best fit statistic used is a likelihood ratio developed by Chirkin and often referred to as the Dima Likelihood. This likelihood function was briefly introduced in section 4.4 and more details are provided in section 6.1 below.

6.1 Dima's Likelihood statistic

In this section we present the likelihood statistic introduced by Dima Chirkin. Chirkin developed the statistic particularly for comparison of the light distribution curves encountered in studies, such as the ones undertaken for this thesis research. However it can be applied more generally. The presentation given here follows Chirkin's paper[110].

We desire a statistic which quantifies the goodness of fit comparing a distribution of binned simulation and measurement data. Chirkin considers a repeatable experiment that is performed n_d times to collect a total of d counts with a per-event expectation of μ_d. The result of the experiment can be predicted by simulation which collects s counts in n_s simulated events and a per-event expectation of μ_s.

Given the total count is $s + d$ the conditional probability distribution function

of observing s simulation and d data counts is given by

$$P(\mu_s, \mu_d; s, d|s+d) = \frac{(s+d)!}{s!.d!}.\left(\frac{n_s\mu_s}{s+d}\right)^s.\left(\frac{n_d\mu_d}{s+d}\right)^d. \tag{6.1}$$

If the data and simulation are completely unrelated to each other and by considering the normalisation requirement (i.e: $n_s\mu_s + n_d\mu_d = s + d$), we can use maximization of the probability function to estimate μ_d and μ_s:

$$\mu_d = \frac{d}{n_d} \;\; and \;\; \mu_s = \frac{s}{n_s}. \tag{6.2}$$

The alternate hypothesis which could be considered is that data and simulation counts have the same mean (i.e: $\mu = \mu_d = \mu_s$). This equality with the constraint $n_s\mu_s + n_d\mu_d = s + d$ uniquely determined the values of

$$\mu = \mu_d = \mu_s = \frac{s+d}{n_s+n_d}. \tag{6.3}$$

The probabilities of the two above hypotheses can be compared by using their likelihood ratio

$$\frac{P(\text{same process})}{P(\text{independent processes})} = \left(\frac{n_d}{n_s+n_d}/\frac{d}{s+d}\right)^d \left(\frac{n_s}{n_s+n_d}/\frac{s}{s+d}\right)^s = \left(\frac{\mu}{d/n_d}\right)^d.\left(\frac{\mu}{s/n_s}\right)^s. \tag{6.4}$$

This expression is proposed in [110] for comparison of different simulation sets with data. This expression can be generalised further to cases where we want to compare simulation and data counts in several bins i rather than a single bin. The general expression is derived in [110] and is given by:

$$\frac{P(\text{same process})}{P(\text{independent processes})} = \prod_i \left(\frac{\mu^i}{d_i/n_d}\right)^{d_i} . \prod_i \left(\frac{\mu^i}{s_i/n_s}\right)^{s_i}, \tag{6.5}$$

where d_i is the number of data counts in the i^{th} bin, s_i is the number of simulation counts in the i^{th} bin and the mean of the i^{th} bin is given by:

$$\mu^i = \frac{s_i + d_i}{n_s + n_d}. \tag{6.6}$$

The error in describing data with simulation is often non-zero (i.e: describing μ_d with μ_s) . The amount of disagreement between data and simulation can be quantified by

$$\chi^2 = \frac{(\ln\mu_d - \ln\mu_s)^2}{\sigma^2}. \tag{6.7}$$

The main cause of having a difference between μ_d and μ_s is due to systematic errors, discussed in the next section (Section 6.4) and this can be modeled with a likelihood penalty term:

$$\exp \frac{\ln^2(\mu_d/\mu_s)}{-2\sigma^2}. \tag{6.8}$$

Adding this penalty term to the likelihood ratio expression yields the likelihood ratio for a single bin to be given by:

$$\frac{P(\text{same process})}{P(\text{independent processes})} = \left(\frac{\mu}{d/n_d}\right)^d . \left(\frac{\mu}{s/n_s}\right)^s . \exp \frac{\ln^2(\mu_d/\mu_s)}{-2\sigma^2}, \tag{6.9}$$

where the μ_d and μ_s are determined by maximizing

$$P(\mu_d, \mu_s; d, s|d+s) = \frac{(s+d)!}{s!.d!}. \left(\frac{\mu}{d/n_d}\right)^d . \left(\frac{\mu}{s/n_s}\right)^s . \exp \frac{\ln^2(\mu_d/\mu_s)}{-2\sigma^2}, \tag{6.10}$$

with the constraint $n_d\mu_d + n_s\mu_s = s + d$.

Taking the negative logarithm yields the expression to be minimized[110]

$$-\ln \mathcal{L} \;=\; \sum_i \left(s_i \ln \frac{s_i/n_s}{\mu_s^i} + d_i \ln \frac{d_i/n_d}{\mu_d^i} + \frac{1}{2\sigma^2} \ln^2 \frac{\mu_d^i}{\mu_s^i} \right). \tag{6.11}$$

This likelihood expression which is often called "Dima's likelihood" [110] is the function that was used for the analysis in chapter 4 and also is used for the goodness of fit statistic in this chapter.

6.2 Method

The machinery developed by Chirkin was used to determine the best fit scattering and absorption coefficients for each of the different wavelength flashers. The PPC software, introduced in section 4.3 has the facility to do the likelihood comparison between data and simulation. The PPC code, as described in section 4.3, is primarily a photon propagation code and thus has the functionality to perform the necessary simulations. Routines are available with the PPC machinery to apply the Bayesian blocking algorithm to the data photon histograms, and apply the binning, determined by the blocking algorithm, to the simulation data as well. Thus, taking the data as input, the routines determine the d_i and s_i to be compared with the Dima likelihood expression.

An iterative procedure is used to determine a unique time-offset for each emitter-receiver pair, hence reducing the uncertainties associated to time-offset. The likelihood value is output for a given pair of candidate absorption and scattering coefficients.

In general an executable PPC command line that can be used for likelihood computation purposes is of the following form

PPCTABLESDIR=../[ice-model] SREP=[..] FAIL=[..] FAST=[..] MLPD=[..] CYLR=[..] FLOR=[..] FSEP=[..] FWID=[..] DREP=[..] FLSH=[..] FLDR=[..] GSL_RNG_SEED=[..]

The first option to specify is the ice model. As discussed, and checked in the previous chapter, Spice 3.2.2 is the most suitable ice model to use as the base model. It is one of the most recent ice models that includes the major anisotropy factors. In addition to the string and DOM number that can be assigned with FLSH in the command line, several other factors such as the number of simulations, effect of cable, azimuthal angle of the emitting DOM can be also specified for the designated emitter LED [114].

The wavelength of the emitter LED can be specified in the PPC command line by using *WFLA* factor as we did in the previous chapter which simulates a monochromatic light source. Alternatively, a file called *wv.dat* can be included in the command line. This file is stored in the ice model directory and allows the implementation of a wavelength distribution for the emitter. The *wv.dat* file used in this project produce an input spectrum with a Gaussian profile around the peak target wavelength.

As the colour LEDs are a non-standard light emitter each of the command line options needs to carefully selected to ensure that the simulation is following the experimental set up. These various options, most of which are shown in the PPC command line above, are introduced in Appendix C.

As an example, by using the relevant factors, the PPC command line that is used for the purpose of likelihood evaluation for LED 7 on c-DOM 22 of string 79 can be written as:

PPCTABLESDIR=../spice3.2.2 SREP=10 FAIL=1 FAST=0 MLPD=-1 CYLR=1 FLOR=0 FSEP=1 FWID=39.4 DREP=250 FLSH=79,22 FLDR=257.082 GSL_RNG_SEED=$RANDOM

With the optimized binning algorithm and time-offset in place, the two main ice optical properties, the scattering and the absorption coefficients are refined in a 2-D LLH scan using string 79 flasher data that was already employed in the last chapter. This is achieved by performing LED LLH-scans of data comparison with PPC simulations for each emitter with a range of different factors of scattering and absorption coefficients. The scattering and absorption coefficients were scaled as they were in the previous chapter. That is by multiplying all the scattering and absorption coefficients of the standard wavelength ($b_e(400)$ and $a(400)$) that are stored in the *icemodel.dat* file. This file was introduced in 5.1.2 and has the values of $b_e(400)$ and $a(400)$ tabulated by depth, in 10m intervals. $b_e(400)$'s in all depth layers

were multiplied by a constant between 0.6 and 2.0 with 0.2 steps whereas $a(400)$'s were multiplied by a constant between 0.4 and 2.0 with the same steps of 0.2. In this way, as in the previous chapter, the depth dependence is kept fixed as it is in Spice 3.2.2 with all depth values scaled by the same amount. The ranges and the step choices for the variation of $b_e(400)$ and $a(400)$ were based on the results obtained from the study conducted in previous chapter using the least square statistic. The scanning range and the selected steps can be iteratively fine tuned based on the initial outcome of the first iteration.

Each single LED within a single DOM flashing at maximum brightness and width and the number of simulated photons were adjusted after accounting for the effective DOM acceptance and by considering the DOM size scaling factor of 16 which was implemented in this model.

As discussed previously, DOM oversizing allows for fewer photons needing to be simulated. For instance by using a scale factor of 16 the required number of photons to be simulated will be 256 times fewer reducing the computational time considerably.

6.3 Analysis and Results

6.3.1 Wavelength dependent scattering and absorption coefficients

The likelihood value for each realisation of the ice parameters due to alteration of the scattering and absorption coefficients are computed for every single emitter LED of all colour-DOMs embedded on string 79. There are a total number of 8 colour-DOMs on string 79 each equipped with 12 multi-wavelength LEDs capable of emitting light at different wavelengths between 340 nm and 505 nm as discussed in section 2.3 that results to total number of 96 individual LEDs. Colour LEDs can emit light at four distinguished wavelength; LED 1, 3 and 5 emit light at 505 nm; LED 2, 4 and 8 emit light at 450 nm; LED 8, 10, 12 emit light at 370 nm; and LED 7, 9 and 11 emit light at 340 nm.

Figure 6.1 shows a two dimensional likelihood scan where the x-axis represents the factors that are used for scaling the scattering coefficient and y-axis represents the factors that are used for scaling the absorption coefficient. Each cell in this plot shows the minimum computed likelihood value to two decimal places. In order to compute the likelihood values presented in this plot, an iterative procedure within the PPC code, repeats the simulation for a fixed number of times and the llh is

calculated based on the simulation which shows the best match to data. The output *llh* value is the overall result obtained based on all the receiving light distributions of all receiver DOMs. The minimum computed likelihood value represents the best fit where in the case of LED 1 on c-DOM 79,22 is ∼1.23 indicating that while the standard scattering coefficient can remain untouched a lower absorption coefficient is required to get the best fit (i.e: $a(400) \sim 0.8 \times a(400)_{standard}$). However, by considering the computed standard deviation to be approximately ∼0.03, as annotated on the plot, a range of combinations of scattering and absorption coefficient factors around the minimum can be considered to be equally well fitting. The standard deviation and relevant uncertainties are discussed further in the relevant section of this chapter.

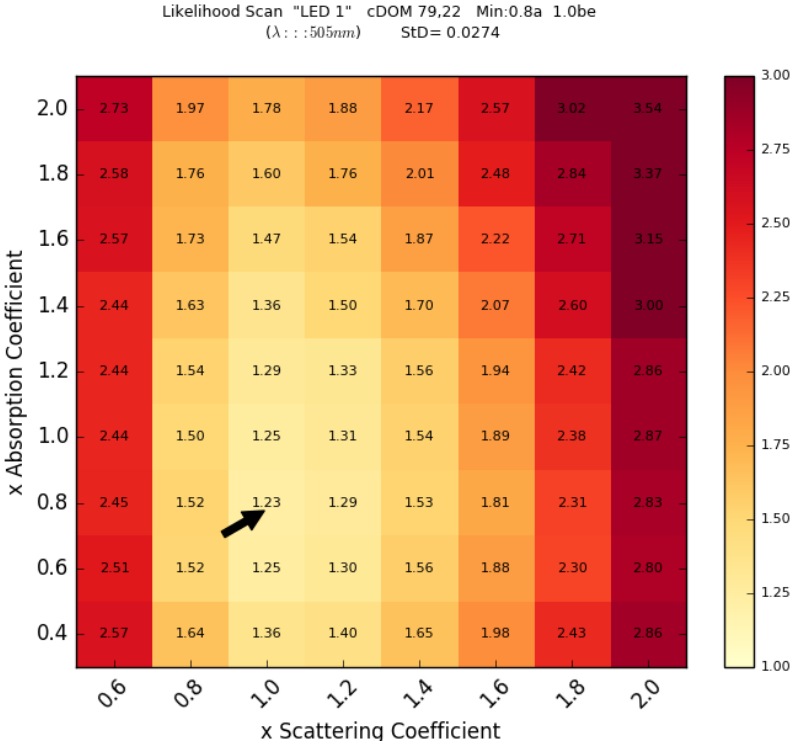

Figure 6.1: 2d scanning of minimum likelihood values. Emitter LED 1, DOM 79,22.

Given that the depth dependence of the absorption and scattering coefficients has been preserved in the characterisation of the ice used in our studies, we would expect to see similar results for each of the different colour DOMs. Figure 6.2 and 6.3 show the 2d scans of LED 1 for all colour-DOMs on string 79, and indeed the results appear to be consistent. Although some DOM to DOM variation is seen overall the results seem to be remarkably independent of the emitting DOM.

The same likelihood evaluation was performed for each of the different wavelength LEDs. For example figure 6.5 shows the 2d scans of LED 7 for all colour-DOMs on string 79 which emit light at a smaller wavelength of ∼ 340 nm.

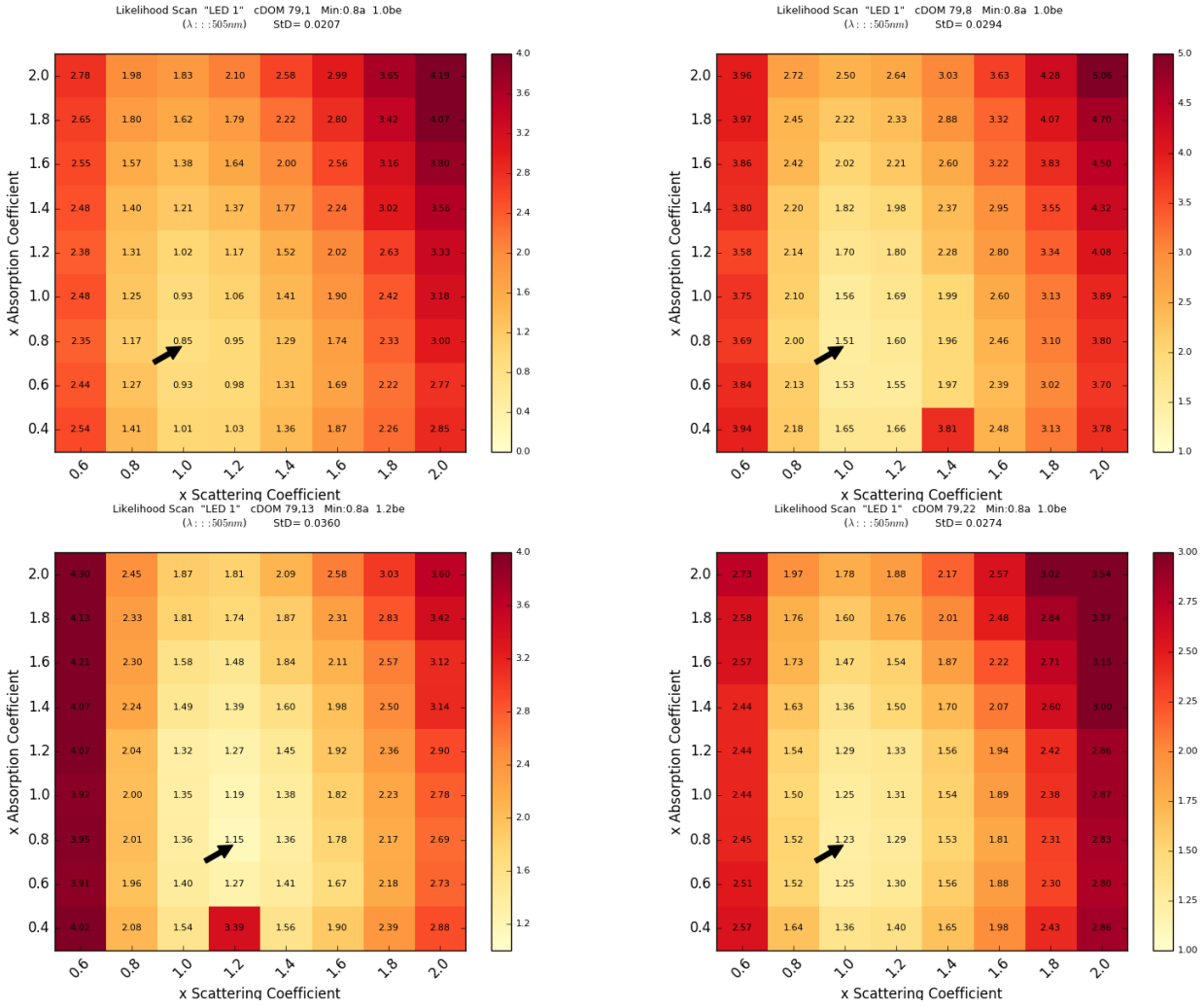

Figure 6.2: 2d scanning of minimum likelihood values. Emitter LED 1, 4 top c-DOMs on string 79. Wavelength: 505 nm.

We can see that in the case of LED 7 where the wavelength is less than the standard wavelength, similar to the previous example where the wavelength was greater than the standard one, the best fit (i.e: smallest likelihood values) are mostly correlated to a smaller absorption coefficient. The reason for having only 7 plots for LED 7 is that a few colour-LEDs are not operational and cannot be used as the in-situ light sources such as LED 7 on c-DOM 79,08 which is excluded from the plots in figures 6.5 and 6.6.

To obtain our final values for the absorption and scattering coefficients for each wavelength, we determined the best fit for a comparison including all of the different depth colour-DOMs. Figure 6.4 shows the 2d likelihood scan of this aggregation of the computed likelihood values for all LEDs with 505 nm wavelength (i.e: LED 1, 3 & 5) on all 8 colour-DOMs of string 79. It can be seen that our initial conclusion that was derived based on the 2d scanning of LED 1 is reaffirmed. That is for the 505 nm fit a lower absorption coefficient than predicted by the current wavelength pa-

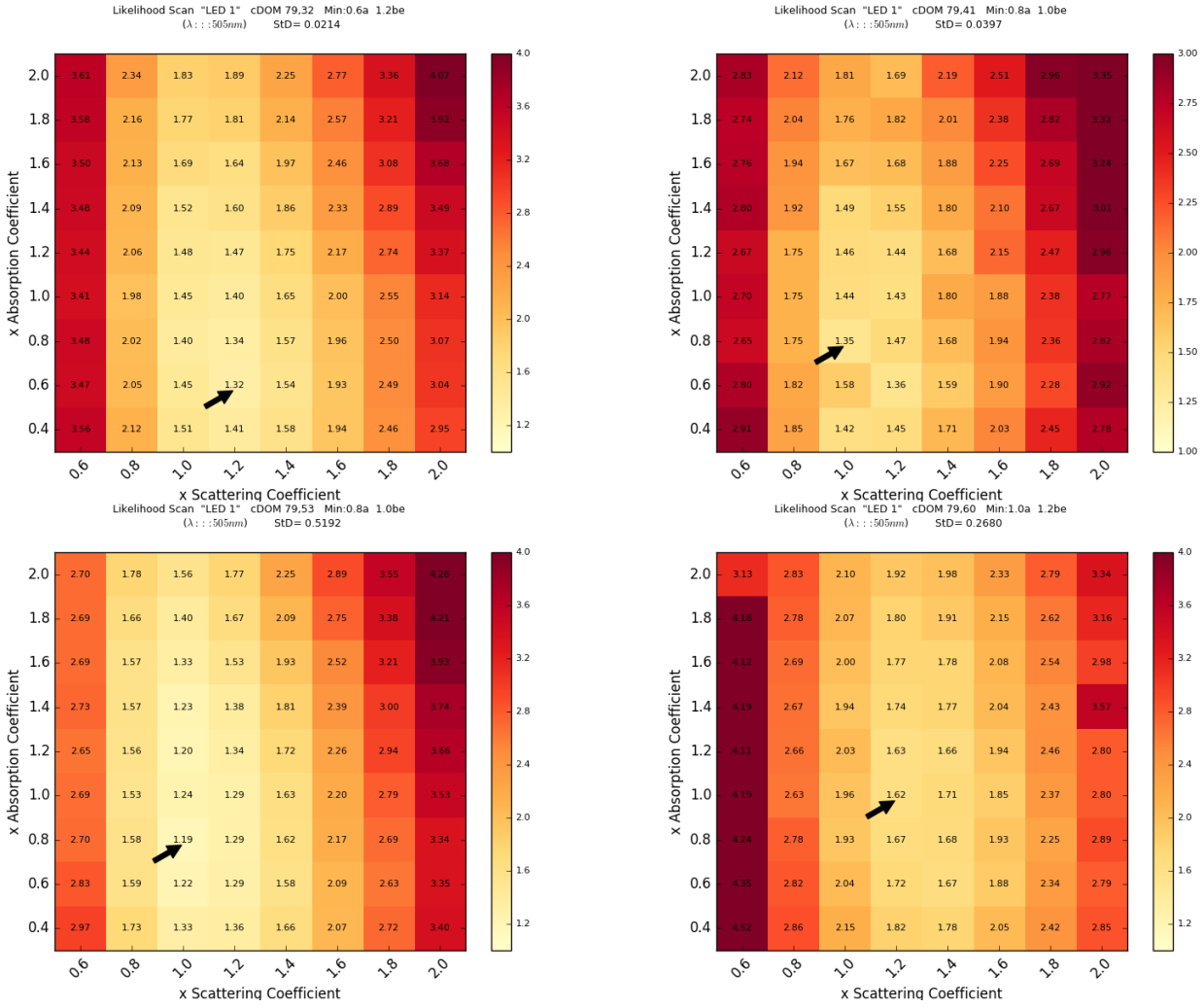

Figure 6.3: 2d scanning of minimum likelihood values. Emitter LED 1, 4 bottom c-DOMs on string 79. Wavelength: 505 nm.

rameterisation was preferred. A lower coefficient corresponds to a larger absorption length. Figure 6.7 shows the same likelihood scan approach for other wavelengths.

A further investigation was made to check the consistency of the results obtained with the positioning of the colour-DOMs. In order to check for possible depth biases the same 2d likelihood aggregation was made for a combination of selected c-DOMs. The four top c-DOMs (i.e: cDOMs 1,8,13,22), the four bottom DOMs (i.e: cDOMs 32,41,53,60) were studied in addition to two more alternative groupings where once 4 cDOMs were picked by choosing the 1st cDOM and then selecting every other cDOMs from the top (i.e: cDOMs 1,13,32,53) and then every other cDOMs were picked from the 2nd cDOM on top (i.e: cDOMs 8,22,41,60).

The computed likelihood values for the selected depth groups did not show any significant difference from the sum of *llh* values calculated from all c-DOMs. Figure 6.8 shows an example of the results of the combined likelihood values corresponding to each group all for LEDs with the wavelength of 370 nm and table 6.1 summarises

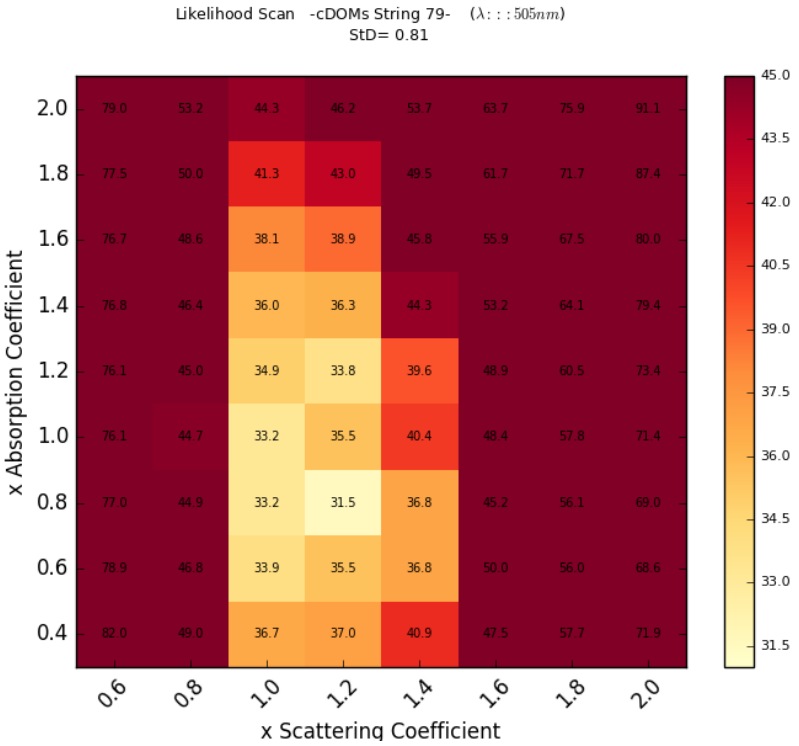

Figure 6.4: 2d scanning of sum of all minimum likelihood values of LEDs with 505 nm wavelength on string 79.

all the results that were obtained both from all eight c-DOMs on string 79 and from the grouped c-DOMs as defined above. The small variation that can be seen in table 6.1 is due to the fact that our 2d scanning needs to go further and finer steps should be considered because the differences between the minimum computed likelihood values and the next to smaller *llh* values are larger than the standard deviation indicating that the best fit usually lays in a region rather than a fixed point. These regions are then scanned through to find the best fits.

In figure 6.9 the red rectangle shows the region on the 2d likelihood plot where the best fit is believed to lie. This plot is the result of summing all computed likelihood values of all colour-LEDs with the wavelength of 370 nm on string 79.

A finer likelihood scan in a selected region derived from the initial scanning was performed. The finer scanning used first 0.1 steps and then 0.05 steps. The approximate best fit which resulted for each available wavelength are as follows:

- Wavelength λ= 505 nm: $a = 0.85 \times a(400)$ and $b_e = 1.15 \times b_e(400)$,
- Wavelength λ= 450 nm: $a = 0.80 \times a(400)$ and $b_e = 1.10 \times b_e(400)$,
- Wavelength λ= 370 nm: $a = 0.95 \times a(400)$ and $b_e = 1.10 \times b_e(400)$, and
- Wavelength λ= 340 nm: $a = 0.80 \times a(400)$ and $b_e = 1.15 \times b_e(400)$,

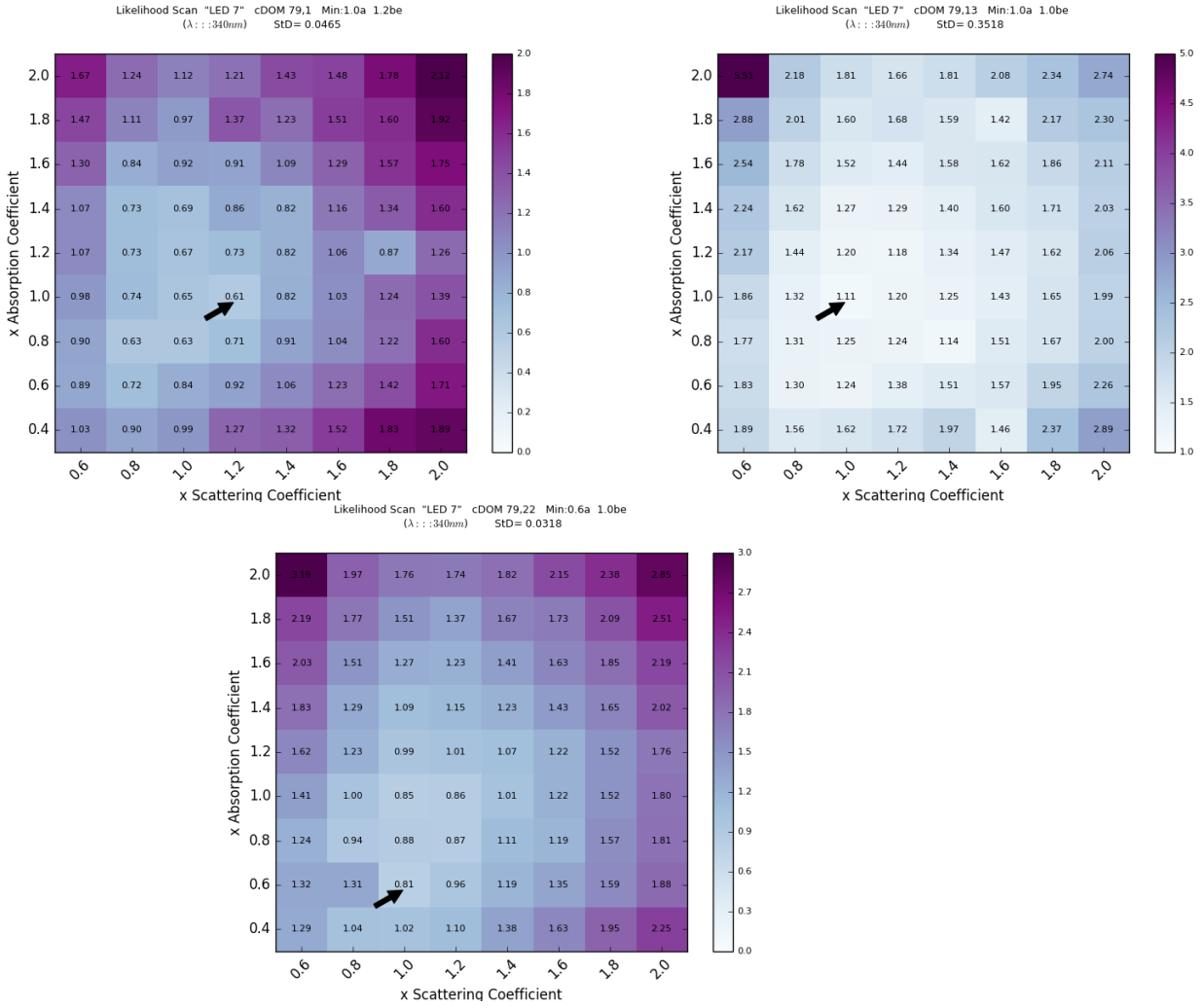

Figure 6.5: 2d scanning of minimum likelihood values. Emitter LED 1, 3 top c-DOMs on string 79. Wavelength: 340 nm

The last finer likelihood scanning results are shown in figure 6.10 where the regions are chosen based on the previous iterations and the steps are selected to reach a point where the difference between the smallest computed likelihood value and the next to smallest value is less than the standard deviation. The standard deviation itself was computed by repeating the whole process of simulation and likelihood evaluation for 10 times to consider the statistical uncertainties due to the fluctuation of the computed results by the simulation software.

In addition to the flashers available in the colour DOMs, for consistency, and to give an extra wavelength point to use in the fitting for α and κ, we also repeated our likelihood fitting procedure with the standard wavelength LEDs which have wavelength of around 400 nm. Eight normal DOMs on string 79 were selected to be the adjacent DOMs to the colour-DOMs and the same process of the likelihood

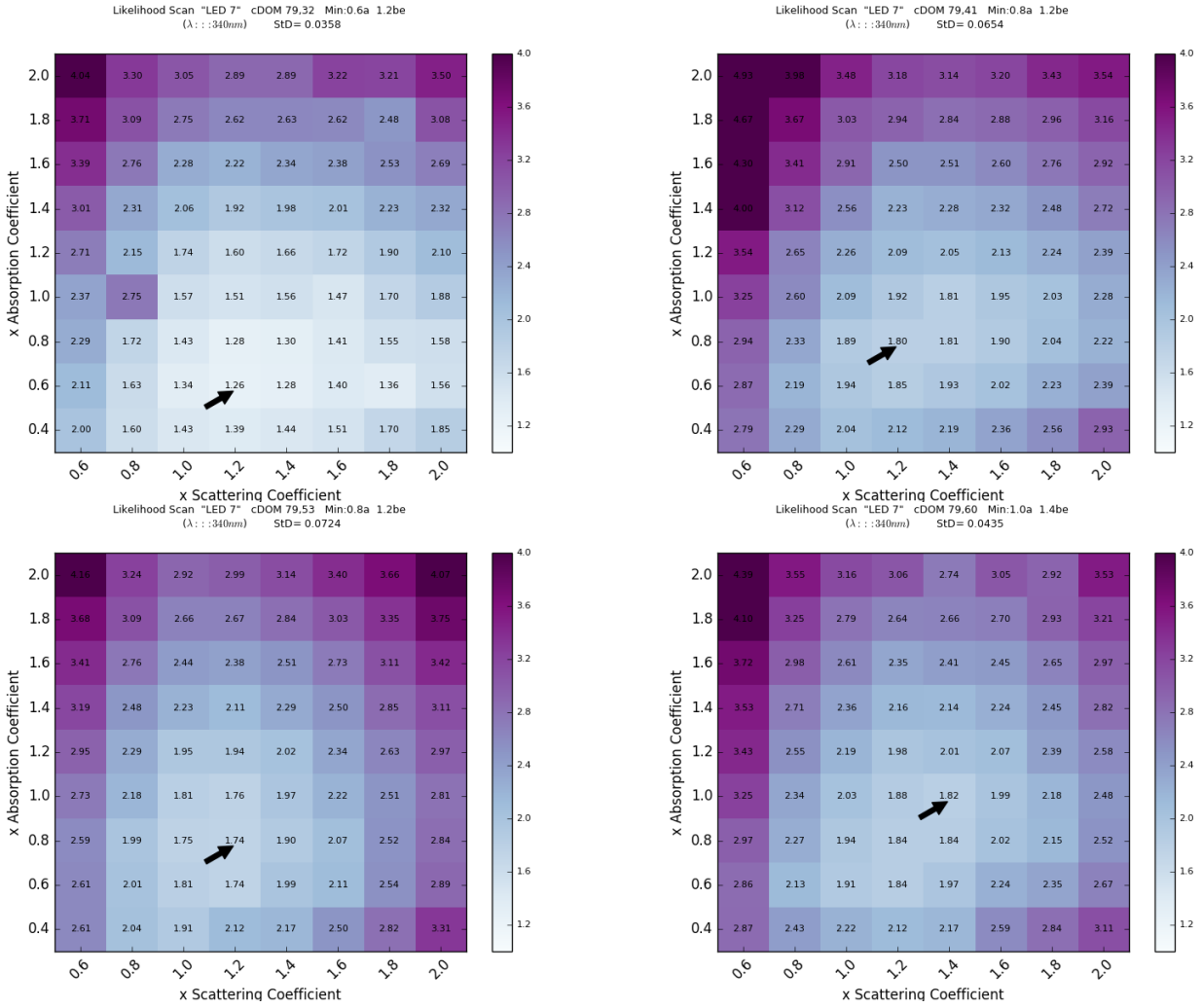

Figure 6.6: 2d scanning of minimum likelihood values. Emitter LED 1, 4 bottom c-DOMs on string 79. Wavelength: 340 nm

evaluation was performed on them. These 8 DOMs are DOMs 2, 7, 14, 21, 33, 40, 54, and 59 each equipped with 12 LEDs capable of emitting light at wavelength of $\lambda \sim 400$ nm. It should be noted here that in order to be consistent with the colour DOM study we have only used the flasher data taken from the horizontal LEDs, and not the tilted LEDs on the standard DOMs. The results can be seen in 6.11. While in comparison to other subject wavelengths the results show a better match with its corresponding standard values that are already being used there is a slight preferred shift from the 1.0 scaling.

Our final results for the best fit absorption and scattering coefficients were obtained from the 2D scans using a spline contour approach. Our procedure was as follows. First the 1σ spread in LLH values was determined using the approach mentioned earlier of re-simulating a realisation close to the optimum 10 times. A spline contour was then fitted to this 1σ spread value. The result can be seen in figure 6.12. The contour gives the uncertainty associated with the best fit coefficients for

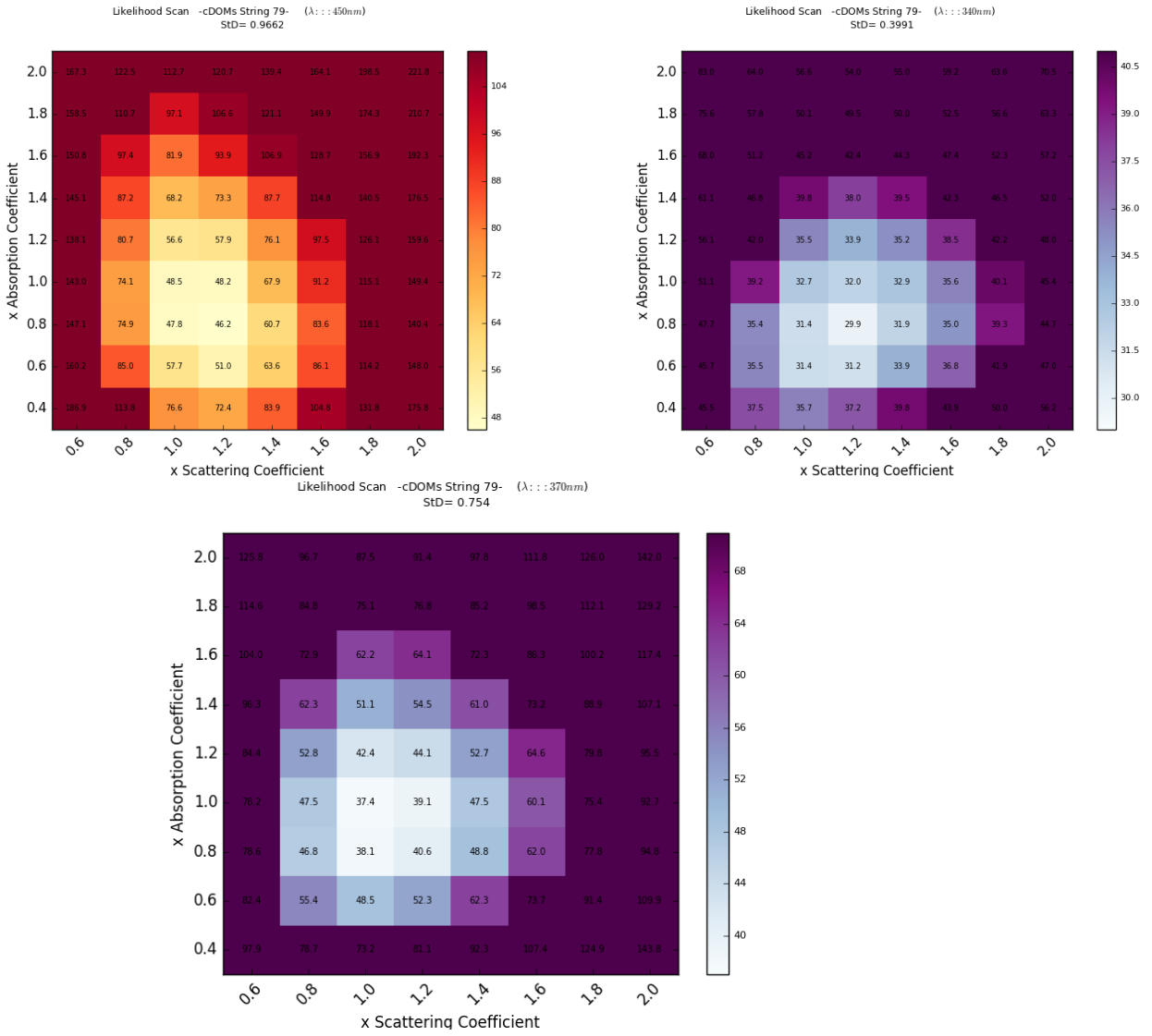

Figure 6.7: 2d scanning of sum of all minimum likelihood values for LEDs with λ= 450, 370 & 340 nm, String 79.

each wavelength. It was also decided to use the centre of the contour region as the best fit value as, in most cases, the LLH topography within the contour was quite flat meaning the located lowest value was subject to fluctuation with simulations.

The best fits and their associated uncertainties determined based on the Spline contours are as follows:

- Wavelength λ= 505 nm: $a = 0.87 \times a(400) \pm 0.04$ & $b_e = 1.12 \times b_e(400) \pm 0.02$,
- Wavelength λ= 450 nm: $a = 0.83 \times a(400) \pm 0.09$ & $b_e = 1.11 \times b_e(400) \pm 0.06$,
- Wavelength λ= 400 nm: $a = 1.01 \times a(400) \pm 0.02$ & $b_e = 1.05 \times b_e(400) \pm 0.01$,
- Wavelength λ= 370 nm: $a = 0.93 \times a(400) \pm 0.09$ & $b_e = 1.05 \times b_e(400) \pm 0.08$, and

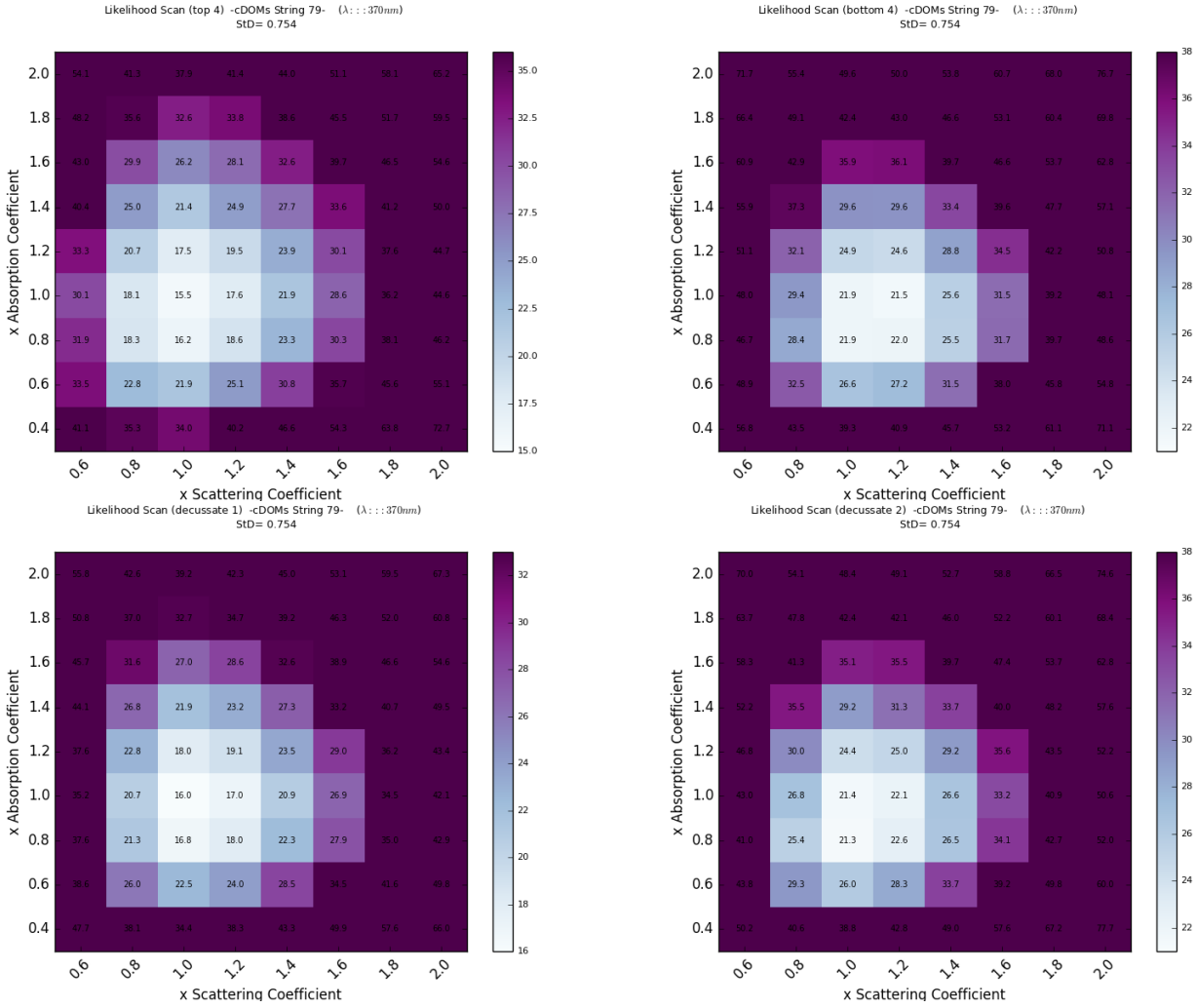

Figure 6.8: 2d scanning of sum of all minimum likelihood values extracted from selected c-DOMs on string 79.

– Wavelength λ= 340 nm: $a = 0.79 \times a(400) \pm 0.08 \quad \& \quad b_e = 1.14 \times b_e(400) \pm 0.09$,

6.3.2 Determination of α and κ

The overall objective of this work is to determine the α and κ values characterising the wavelength dependence in the expressions

$$b_e(\lambda) = \left(\frac{\lambda}{400}\right)^{-\alpha} b_e(400), \tag{6.12}$$

$$a(\lambda) = a_{dust}(\lambda) + Ae^{-B/\lambda}.(1 + 0.01.\delta\tau), \tag{6.13}$$

with

$$a_{dust}(\lambda) = a_{dust}(400).\left(\frac{\lambda}{400}\right)^{-\kappa}, \tag{6.14}$$

	$\lambda = 505nm$		$\lambda = 450nm$		$\lambda = 370nm$		$\lambda = 340nm$	
	b_e	a	b_e	a	b_e	a	b_e	a
All colour DOMs	× 1.2	× 0.8	× 1.2	× 0.8	× 1.0	× 0.8	× 1.2	× 0.8
Four top colour DOMs	× 1.2	× 0.8	× 1.2	× 0.8	× 1.0	× 1.0	× 1.0	× 1.0
Four bottom colour DOMs	× 1.2	× 0.8	× 1.2	× 0.8	× 1.0	× 1.0	× 1.2	× 0.8
Every other cDOM from 1	× 1.2	× 0.8	× 1.2	× 0.8	× 1.0	× 0.8	× 1.2	× 0.8
Every other cDOM from 2	× 1.2	× 0.8	× 1.2	× 1.0	× 1.0	× 1.0	× 1.2	× 0.8

Table 6.1: Summary of the best fits using likelihood scan applied on different c-DOMs.

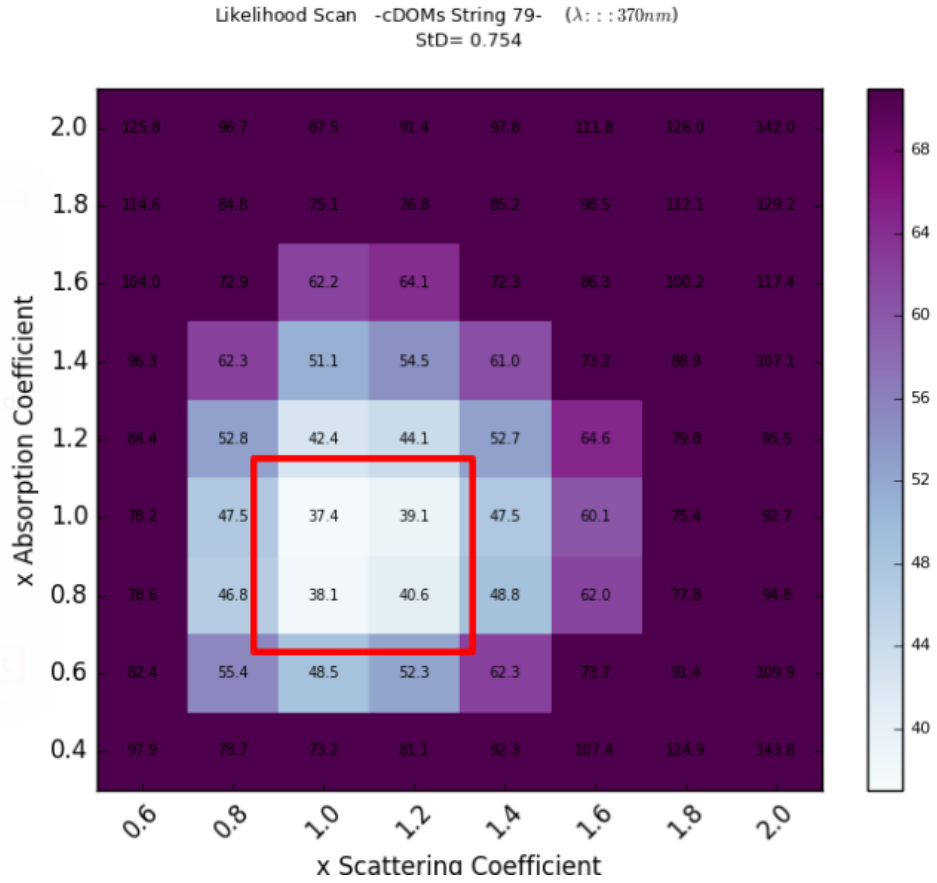

Figure 6.9: Region of best fits in a 2d scanning of sum of minimum likelihood values for all c-DOMs with $\lambda = 370nm$ is represented inside the red rectangle.

A function of the form in eq. 6.12 was fitted to the five values of $b_e(\lambda)$ yielding $\alpha = 0.65 \pm 0.08$. Similarly a function of the form $a_{dust}(\lambda) \propto \lambda^{-\kappa}$ was fitted to the five values $a(\lambda)$ yielding κ to be approximately 1.43 ± 0.41. These fits are shown in figures 6.13 and 6.14 respectively, where the black curves show the fit based on the standard values of the coefficients and the blue curves illustrate the same fits based on the results obtained in this research programme. For fitting purposes, the derived errors

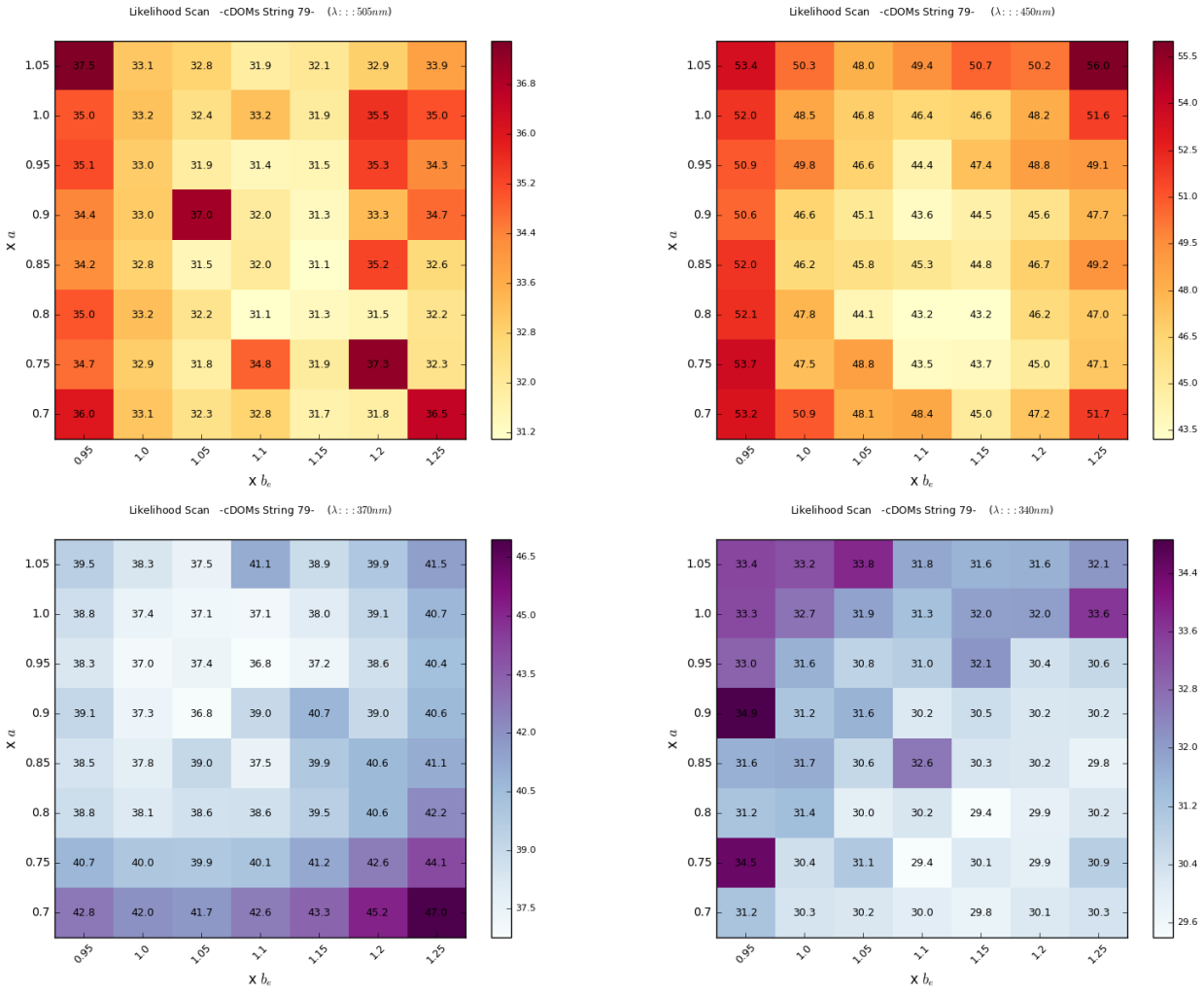

Figure 6.10: 2d scanning of sum of all minimum likelihood values of all c-DOMs on string 79 with 0.05 steps.

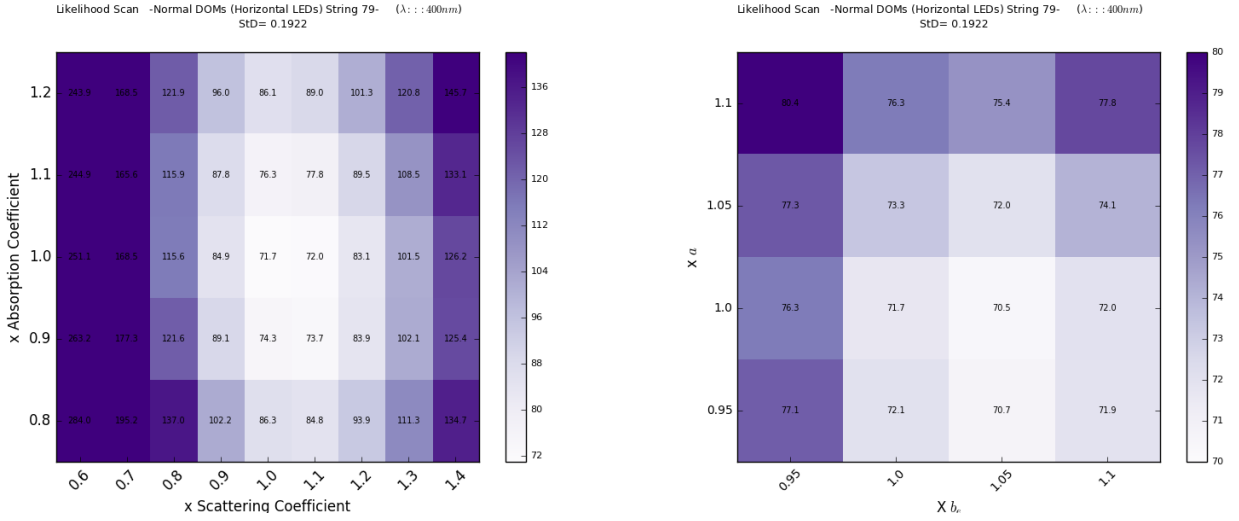

Figure 6.11: 2d scanning of sum of all minimum likelihood values from selected normal DOMs on string 79 with left: 0.1 steps, and right: 0.05 steps.

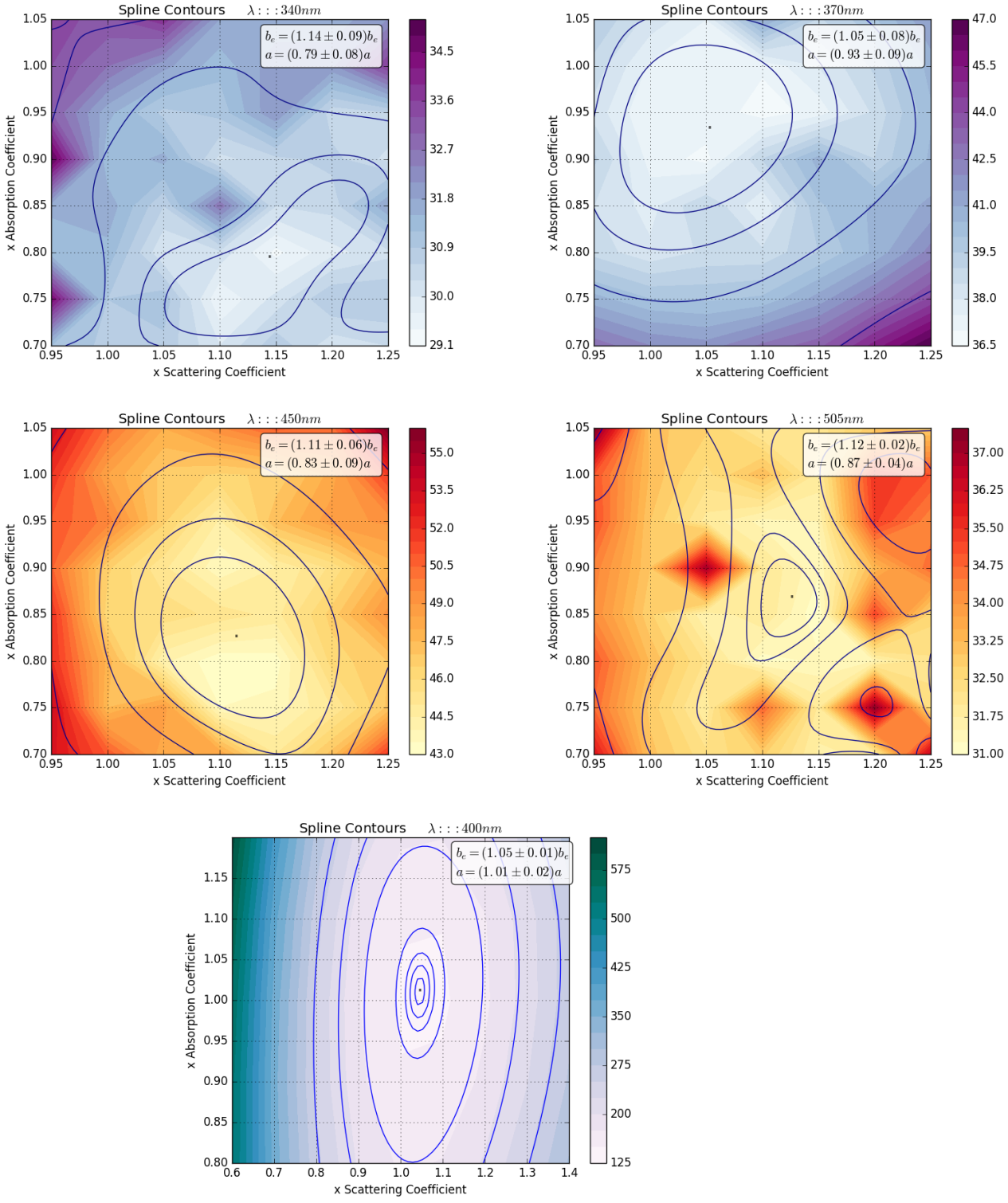

Figure 6.12: Spline contours to determine the uncertainties for all 5 available wavelengths. The background colour is a smoothing spline used to construct the statistical confidence contour, while the inner contour corresponds to one standard deviation. The optimum points are denoted by dots and are chosen to be in the middle of the inner enclosed contours.

have been scaled by a factor constant for all wavelengths until $\sum \chi^2/dof$ became 1. This ensures that the relative uncertainty between the wavelengths is preserved.

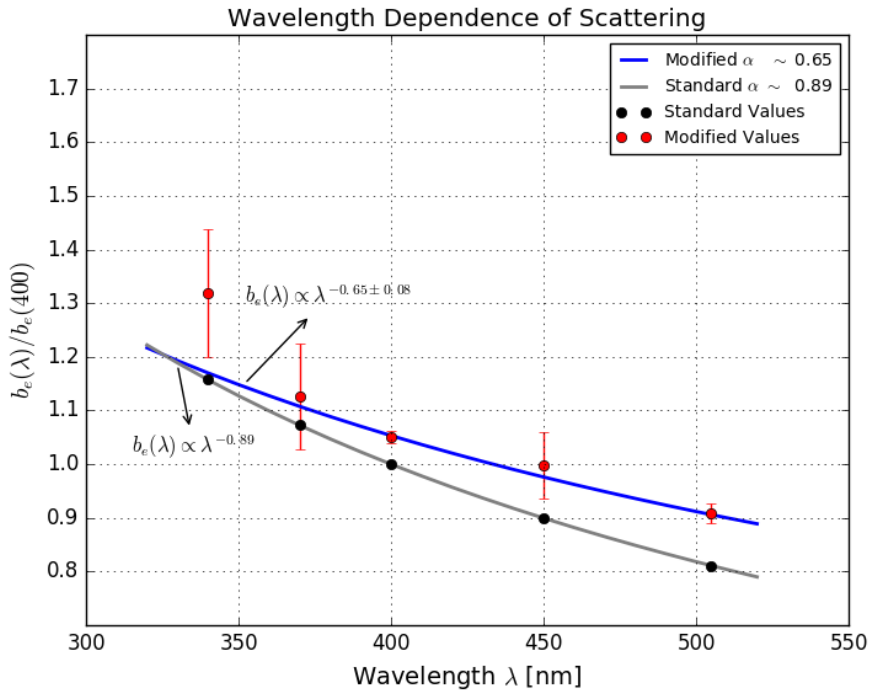

Figure 6.13: Wavelength dependence of scattering. A power law $b_e(\lambda) \propto \lambda^{-\alpha}$ with $\alpha = 0.65 \pm 0.08$ was fitted to the effective scattering coefficients $b_e(\lambda)$ determined with pulsed data at five wavelengths. The data points are wavelength averages (normalised with $b_e(400)$) and the red error bars represent the uncertainties determined by the contour plots.

The values of α and κ currently used by IceCube in simulations are $\alpha_{\text{standard}} = 0.89$ and $\kappa_{\text{standard}} = 1.08$ respectively. The values obtained here are reasonably close to these values and, given the values used currently should have a similar uncertainty, their uncertainty ranges overlap.

Regardless of the shape of the wavelength dependence curve, as has been remarked earlier, and as is clear from figures 6.13 and 6.14, the results obtained in our study favour overall higher scattering and lower absorption coefficients than the values currently used in IceCube modelling. Some of the reason behind this may be due to the fact that the results are obtained for a single string, and it is likely that not all of the $x-y$ plane inhomogeneity in ice properties is captured by the ice tilt modelling (see section 3.5.4 for discussion of the ice tilt). Some support for this possibility, for scattering at least, is that the standard LED best fit coefficient is also somewhat higher than standard although not as large a factor. Further discussion around this point is made in Chapter 7.

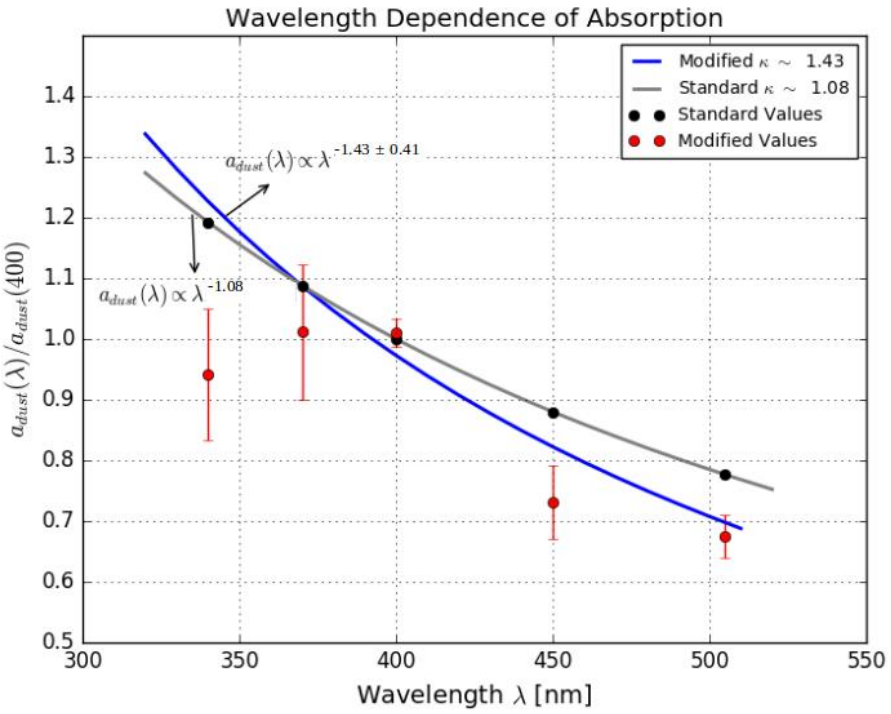

Figure 6.14: Wavelength dependence of absorption. A power law $a_{dust}(\lambda) \propto \lambda^{-\kappa}$ with $\kappa = 1.43 \pm 0.41$ was fitted to the absorption coefficients $a(\lambda)$ determined with pulsed data at five wavelengths. The data points are wavelength averages (normalized with $a(400)$) and the red error bars represent the uncertainties determined by the contour plots.

Also it can clearly be seen in figures 6.13 and 6.14 that the uncertainties associated with the scattering and absorption coefficients for the standard wavelength values are much smaller than those of the coefficients for the other wavelengths. The exact reason for this is unclear, but it is possibly due to the fact that the base ice model used has been derived from the standard wavelength flasher data and, for instance, it could be possible that the anisotropy or depth variation is somewhat wavelength dependent. The smallness of the uncertainties associated with the standard wavelength values means that these values have a higher influence than the other points on the curve fit. Comparing figures 6.13 and 6.14 with 6.15 by eyes it appears that the curve through the coloured wavelength points, without the 400 nm point, would have a more similar shape to the current wavelength dependence curve.

To check this influence, the α and κ factors were also determined with the data points associated with the standard wavelength excluded. This, as it can be seen in figure 6.15, resulted in different values for α and κ. These values $\alpha \sim 0.83$ and $\kappa \sim 0.99$ both show a better match with the currently used values of $\alpha_{standard} \sim 0.89$ and

$\kappa_{standard} \sim 1.08$ respectively. However before any final decisions are made it would be best to have a better understanding for the reasons for the colour LEDs and the standard LEDs giving somewhat different results.

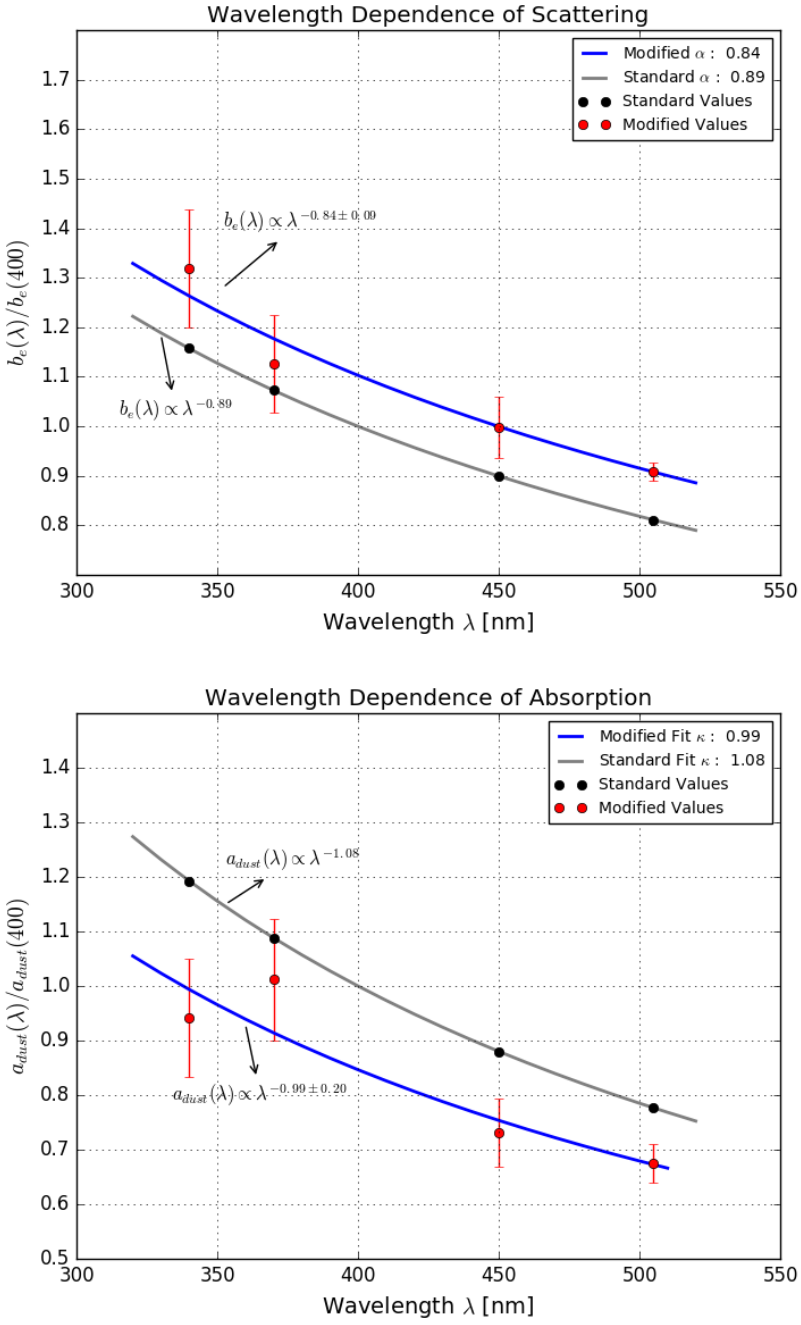

Figure 6.15: Wavelength dependence of scattering and absorption. α and κ are determined after excluding the standard wavelength of 400 nm. A better match is shown between these values and the standard ones but still an overall higher scattering and lower absorption have been observed.

As far as the absorption fit is concerned, the modelling we have done is limited

in that we have only considered a scaling of $a_{dust}(\lambda) = a_{dust}(400).\left(\frac{\lambda}{400}\right)^{-\kappa}$ to determine κ and no account has been taken of the $Ae^{-B/\lambda}.(1 + 0.01.\delta\tau)$ term in equation 6.13. The term we have considered is the Mie Theory[118] term that describes the absorption of the photons in the 200 nm to 500 nm wavelength range, due to insoluable dust.

The second term in equation 6.13 determines the absorption of photons in the red and infrared range where an exponential rise in absorption occurs for wavelengths greater than around 500 nm in South Pole ice. This can be seen in figure 6.16-left from [79]. Absorptivity in this regime exhibits spectral structure due to different modes of H_2O molecular stretching, bending and vibration. Furthermore, the temperature profile of the ice is also included for in the second term in 6.13 where τ represents the temperature. As discussed in section 3.3 temperature is a depth dependent parameters [92].

We investigated how the second term of equation 6.13 fits with the parameters we determined. To do this we extracted the z coordinates of the c-DOMs on string 79 for the depths of the c-DOMs we used, and substituted these depth values into equation 6.13 to find the absorptivity values at different depth levels. The result is depicted in figure 6.16-right and shows a similar pattern to the fit shown in 6.16-left. We can conclude that although the calculated κ value is only an approximation, the overall absorptivity behaviour of the light at different wavelength is consistent with equation 6.13.

The values of α and κ currently in use in IceCube modelling were obtained from a study in 2006[79]. Overall the study presented here has the potential to provide more reliable results than those from the 2006 investigation. This is due to at least three reasons: first, the number of in-situ light sources available in 2006 work is less than the number of LED emitters that are used in our current analysis, second, prior to 2011 the precise orientation of the azimuth angle of the LEDs were unknown, and third the advancements in the calibration processes as well as in simulation software over the last years grant us to have an analysis that includes the systematic with higher precision. However further work should be done before a final decision is made, but this work is best undertaken after the completion of the birefringence investigations and modelling (see section 3.5.6).

6.4 Systematic Errors and Uncertainties

The systematics relevant to IceCube experiments can be classified into three categories: uncertainties in the ice properties, errors originating from hardware effects,

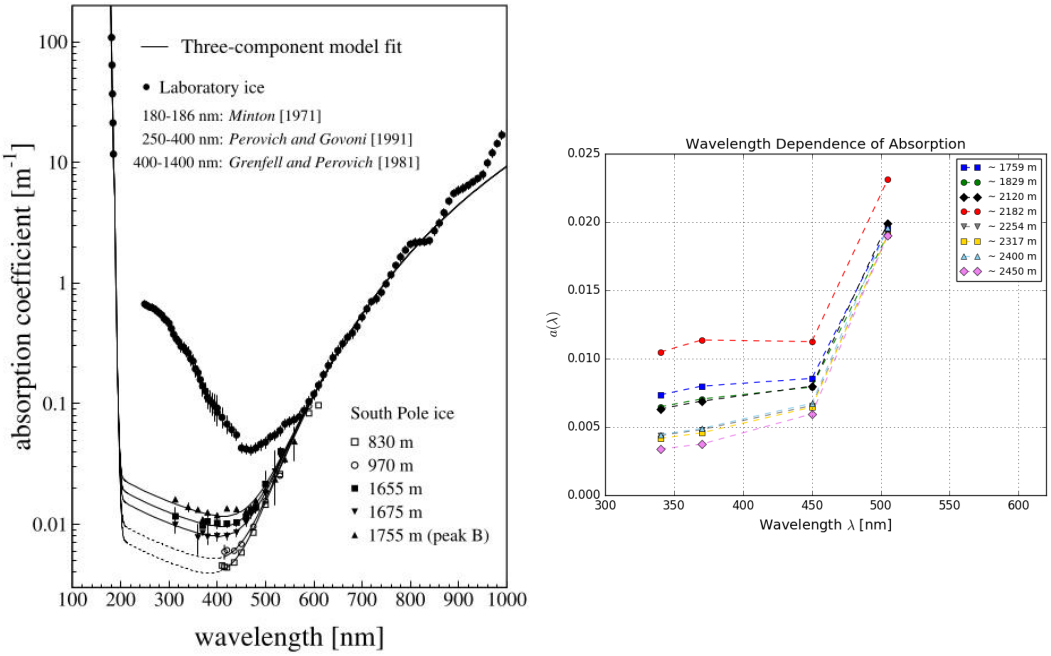

Figure 6.16: Wavelength dependence of absorption from ultraviolet to infrared, for deep South Pole ice and for laboratory-grown ice. [(left:) Ackermann et al. "Optical properties of deep glacial ice at the south pole". Journal of Geophysical Research, 111:126, (2006).]

and uncertainties as a result of our physics assumptions.

Calibration procedures take care of most of the hardware parameters such as PMT transit times, ADC gain, to an extent that we usually do not need to consider them in our analysis. However, the hardware parameter that required to be considered at analysis level is the absolute photon detection efficiency averaged over all DOMs. As discussed in section 3.5.2 determining the DOM efficiency is one of the challenges of any proposed ice model and its evaluation is closely correlated with the accuracy of the description of the ice properties. We usually consider a 10% uncertainties on the absolute photon detection efficiency in our analyses. However, other systematics, including absorption in the hole ice, shadowing by the DOM cable as well as positional uncertainties of the LEDs and the quantum efficiency of individual PMTs, were not considered in this thesis.

In addition, a primary systematic uncertainty for the simulation is considered to be about 15% and is included in our analyses in this chapter. The main causes of this uncertainty is believed to be due to uncertainties in the flasher parameterisation as well as LED-to-LED fluctuations.

In the 2006 study mentioned above[79] a thorough investigation of the uncertain budget was completed. We have not repeated these investigations but summarise the results of the 2006 study.

For the simulation based fits similar to what is done in our work, the effects of systematics can be estimated by altering the ice model parameters in the photon propagation simulation within ranges that reflect the uncertainty in our knowledge. For instance the mean scattering angle (θ), introduced in section 3.2.2, can be altered in the simulations to determine the uncertainties in our modeling of dust. In the 2006 study, $<\cos\theta>$ was varied in steps of 0.1 between 0.4 and 0.99 in simulations and compared to the data set which was derived from in-situ light sources embedded at different depths all emitting light at 370 nm wavelength [79]. The result of that study showed a weak dependence of the fitted values of scattering and absorption lengths on the choice of $<\cos\theta>$. It was showed that both scattering length (λ_e) and absorption length (λ_a) decrease by $\sim$2.5% for each increase of 0.1 in $<\cos\theta>$.

As it was discussed in section 3.5.1, the properties of hole-ice (column of refrozen ice around each string with approximately 30 cm radius) is different from the properties of the bulk ice, mainly due to the higher abundance of the air-bubbles in the hole ice and also due to impurities as a result of drilling process. It is believed that the properties of the hole-ice can affect the angular acceptance of the DOMs by making it slightly more isotropic. This assumption can be tested by repeating all fits to pulsed data with simulation generated based on alternative models of angular DOM efficiency. Studies show a minimal dependency and yield to the uncertainty in the measured coefficients to be between 1 and 2%.

In addition, the uncertainties related to detector calibration should also be considered because these errors that are caused by the device calibration can affect the timing fit by convoluting Gaussian errors with the delay time distributions. Our knowledge about the relative positions of the DOMs comes with an uncertainty of less than 1 m which can affect the uncertainty in timing to a value close to 5 ns. This impact can be investigated by randomly smearing hit times in the simulation time distributions. Studies indicate this effect to be less than 1% for both scattering and absorption.

Other sources of uncertainties have been also proposed and tested but the results showed that those uncertainties are relatively too small and thus the uncertainties that are caused by them in the fitted parameters are negligible. Those proposed sources of uncertainties are the velocity of light in the ice [120], the sensitivity to the binning of the time distributions, ice layers, etc. The estimates of some of the systematic errors are summarised in table 6.2.

On the basis of these investigations into potential error sources, a 10% overall systematic error to the optical parameters from fits to pulsed data is considered in our analyses in this thesis.

Systematic Error Source	**Timing Fits**	
	σ_{b_e}	σ_a
Light propagation modeling		
Mean scattering angle	2.5%	2.5%
Velocity of light in ice	<0.5%	<0.5%
Light source characteristics		
Spatial emission pattern	<2%	<1%
Emission time profile	<1%	<1%
Wavelength spectrum	<1%	<1%
Detector calibrations		
Time resolution	<1%	<1%
Geometry calibration	<1%	<1%
Properties of refrozen ice column	<2%	<2%
Absolute OM detection efficiency	-	-
Relative OM detection efficiencies	-	-
Methodology		
Time distribution binning	<0.5%	<0.5%
Averaging over depth	<2%	<2%

Table 6.2: Estimates of Systematic Uncertainty in Measurements of Scattering (b_e) and Absorption (a). [Ackermann et al. "Optical properties of deep glacial ice at the south pole". Journal of Geophysical Research, 111:126, (2006).]

7 Conclusion and Outlook

This thesis has mainly explored the wavelength dependency of the optical properties of the glacial ice at the South Pole where the IceCube neutrino observatory has been constructed. A good understanding of the optical properties of the ice is essential for reliabe reconstruction of the characteristics of the neutrinos detected.

Each DOM in IceCube includes a flasher board with LED light sources arranged in 6 pairs around a circular disk. Flashes from the LED light sources are detected on the surrounding strings. Comparison of the detected time distributions of light with a simulation of the experimental set-up allows the optical properties of the ice to be tested.

In Chapter 4 we presented two smaller calibration studies which were completed as part of this thesis research. In the first we determined the time of direct travel for photons between IceCube DOMs which allows the spacing of the DOMS to be verified. In the second study we determined the orientation of the DOM, in particular the azimuthal angle for the LED flashers. This study is important for accurate simulations of the LED flashers.

In Chapters 5 and 6 we have presented our main studies with the aim to investigate the wavelength dependency of the optical properties of the ice where a least-square method and Dima's likelihood method have been used as our statistical tools.

In chapter 5 we presented a pilot study examining the wavelength dependency of the ice optical properties. The data used is flasher data taken with the colour LEDs on string 79. In the pilot study we used a least-square statistic to determine the goodness of fit. We first verified that the most recent ice model Spice 3.2.2 gave the best fit to the data compared with recent alternatives. The pilot study allowed us to get a good understanding of the complicating factors which need to be addressed in ice calibration studies. Examples of these issues are the variable time-offset and the low statistics in some bins of the photon time distribution. The time-offset refers to the non-zero time difference between when the flasher is recorded to flash and the apparent time of flashing. A set of routines, developed by Chirkin, which can address these issues were used for our final analysis.

Chapter 6 has presented our final results where Chirkins's machinery with the Dima likelihood statistic were used to derive the best fit scattering and absorption

coefficients. Our method was to apply an overall scaling to the depth dependent values used thus preserving the form of the depth dependence. It was found that an overall higher scattering and a lower absorption gave the best fits across the different wavelengths. The reasons for this were unclear. Although it could merely be that string 79 lies in a $x - y$ position which has this difference from the average $x - y$ dependent values, given that not as large differences were seen in a study of the standard 400 nm wavelength flashers this does not seem to be the full solution. Further work is necessary to understand the differences. However it is already known that the current ice modeling is incomplete, and as described in section 3.5.6, studies of the birefringence properties of the ice are in progress.

These studies suggest that the optical ice anisotropy is the result of the ice micro-structure or so called birefringent poly-crystal. Development of a new ice model in which this poly-crystal property is considered and fully implemented is one of the main goals of the ice calibration studies. This prospective model could possibly explain some of the discrepancies we always observe in the in-situ light propagation and eventually improve our understanding of the wavelength dependency of the optical ice properties. This is because prior to this new model being proposed, we used to assumed that the optical ice anisotropy is caused by impurities and associated Mie scattering and hence concentrate our studies to explain the observed anisotropy in that way. However, considering the effect of the ice micro-structure will open a new window to the understanding of the realisation of the glacial ice.

The wavelength dependence should be revisited after the birefringence has been taken into account in the ice modelling. Nevertheless, the values of the two parameters, α and κ, which determine the power law scaling of the wavelength dependence, which we obtained were consistent with those currently in use, giving reassurance for this aspect of the ice characterisation. Determination of α and κ and the verification, or otherwise, of the current wavelength dependency modelling in use by the IceCube collaboration was the main goal of this research project.

Characterisation of the glacial ice is an ongoing project. It is crucial not only for improving the reconstruction analyses or enhancing the overall resolution of the detector, but also for being able to introduce the next generation IceCube detector. IceCube-Gen2 is planned to address the requirement of a further deep exploration of the neutrino universe. IceCube-Gen2 aims to deliver statistically significant samples of very high energy astrophysical neutrinos, in the PeV to EeV range, and yield hundreds of neutrinos across all flavours at energies above 100 TeV. This will enable detailed spectral studies, significant point source detection, and new discoveries.

A number of new calibration devices are already under development to be de-

ployed and used in IceCube-Gen2.

POCAM or Precision Optical CAlibration Module for IceCube-Gen2 has been developed as a fully isotropic light source. Current flasher LEDs are only able to emit light either horizontally or at a $\sim 45^{\circ}$ angle into the ice. A fully isotropic light source will be beneficial when it comes to study in which illumination at different angles is required. Studies such as determining hole ice properties, relative DOM efficiencies, or the ice anisotropy will be improved by using POCAM.

A rotatory laser system is also under development to work as a complementary tool to POCAM. This laser system would be able to provide narrow laser based pencil beams with sub-degree accuracy. This device will be used to improve the scattering function measurements or to explore the hole ice with a higher precision.

In addition, it has been decided to use a new camera system in IceCube-Gen2. A camera system will be integrated into every future DOM to provide a clearer picture about the local ice around each DOM.

These new devices will eventually enhance the accuracy of our knowledge on the properties of the glacial ice which in return will improve the precision of the future analyses and ultimately the overall sensitivity of the observatory. The techniques used in this thesis will be able to be adapted to use the wealth of new calibration data to realise these improvements.

A Steps for determining likelihood values

As it is discussed in 4.5 the raw data is processed by a sequence of some codes which eventually results in a single value that represents the likelihood. Below those codes are introduced in the order of their use:

- "*Flashermaster.py*": This code takes the raw data file as well as the *gcd* file as the input and the output is an **.h5** file.
- "*h5qtot.py*": The **.h5** file from the previous step is the input file for this script. This code then gives the total charge (an approximation of the number of photons observed by receiving DOMs) which should be used as an input when we run the main likelihood code.
- "*h5todata.py*": This code processes the **.h5** file and generates a **.txt** file which is soft-linked to a *dat* file that is the main input for the likelihood code.
- "*llh method* 1": This code reads the *dat* file that is generated from the **.h5** file for the flasher run and gives the light yield which is a constant that relates the number of simulated photons to the number of observed photons and should be used for running *llh* method 2.
- "*llh method* 2". This code also reads the *dat* file but gives the likelihood of the chosen angle as the output. We can then alter the angle and run it again and repeat this over a range of angles from 0 to 360 degrees.

B PPC configuration files

The configuration files stored in the relative ice model directory each contains important information that are used by PPC for generating desired simulation outputs. Some of the main configuration files are listed below:

- **cfg.txt**

  This file contains the main configuration used for simulation. Below is a general example of what a typical *cfg.txt* file can contain. While the first block is essential and therefore exits in all *cfg.txt* files, the last two blocks are optional where the first of these two last blocks represents the major anisotropy of the ice and the last block contains the information related to the hole-ice specific properties. By omitting one of these two last blocks or two, major anisotropy and/or hole-ice properties will be excluded from the simulation.

```
# ppc configuration file: follow strict order below
5 # over-R: DOM radius "oversize" scaling factor
1.0 # overall DOM efficiency correction
0.35 # 0=HG; 1=SAM
0.9 # g =< cos θ >


130 # direction of major anisotropy axis
-0.106 # magnitude of major anisotropy coefficient k1
0.053 # magnitude of minor anisotropy coefficient k2


0.5 # hole ice radius in units of [DOM radius]
0.5 # hole ice effective scattering length [m]
100 # hole ice absorption length [m]
0.35 # hole ice 0=HG; 1=SAM
0.9 # hole ice g =< cos θ >
```

- **eff-f2k.ori**

  This file contains information related to "relative DOM efficiency" or RDE. It usually comes into four columns where the 1st two columns contain the string and DOM numbers and the last two columns stored RDE value and Type respectively. In most recent ice models the last column is usually omitted and Type=0 are assumed for all rows. Type=1 used to be assumed for DOMs with high quantum efficiency but since we can alternatively specify Type=0 to those high-QE DOMs simply by using a higher RDE value (i.e: 1.35 instead of 1), in recent ice models *eff-2fk.ori* usually contains only three columns.

- **icemodel.par**

  While the *icemodel.dat* file contains $b_e(400)$ and $a_{dust}(400)$ which are two of the six parameters ice description discussed in section 3.3, this file contains the rest four including alpha (α), kappa (κ), A and B as defined in section 3.3.

- **tilt.dat**

  This file describes ice layer tilt, each line contains: 1-center depth of layer, and 2- several depth corrections for locations specified in file *tilt.par* (below).

  and,

- **tilt.par**

  This file contains a map of tabulated ice layer tilt locations, each line has: string number, and a relative distance along the gradient tilt direction (225 degrees SW).

C PPC Flasher Configuration

As discussed in section 4.3 executing PPC should be performed in a way that the emitting LED represents the designated LED of the actual experiment, hence we need to specify many factors in order to improve the accuracy of our simulation. These factors are introduced below [114]:

−*SREP:* This can be used to specify the number of simulations at each step of the calculation. Default is 1 and the value that is used in our analysis was 10.

−*FAIL:* This by setting to 0 will cause program to fail on some warnings. Default is 0 but we have used 1 to avoid failure.

−*FAST:* This could be set to either 0 or 1. If 1 is used the software will only use time-integrated charges during simultaneous t_0 (start time) and energy unfolding steps and if 0 is assigned time-binned charges in parts of the calculation when optimising t_0 and unfolding energy/flasher brightness is used . Default value of 0 has been used.

−*CYLR:* This is for cable simulation: 1 will cause the software to simulate straight cylindrical cable, and 0 will result to simulating a curved Gaussian-like shape of cable that curves around the DOM and asymptotically approaches the DOM axis above/below the DOM. The former is faster and has been used in our analysis.

−*FLOR:* This can be used to align the flasher tilt with the tilt of the DOM. For such an alignment value 1 should be assigned. Default value is 0 and has been used in our current work.

−*FSEP:* By setting FSEP to be *"n"* likelihood will only accept DOMs that are more than *"n"* DOMs away from flasher. Default is 1 which means that if DOM 79 is flashing, DOMs 78 and 80 are not used.

−*FWID:* This can be used to set the width (in degrees) of the 2d Gaussian that determines the light emission profile of flasher LEDs.

−*DREP:* We have used DREP=250 which indicates that the data file contained averages for this many events. Numbers above 1 are usually used only if there were

multiple in-situ light source events taken with the same configuration (e.g. 250 flasher events)

– *FLDR:* Here we can assign the azimuth angle of the flasher LED.

Bibliography

[1] Anthony M. Hillas. *Cosmic Rays: Recent Progress and some Current Questions.* Cosmology, Galaxy Formation and Astroparticle Physics on the pathway to the SKA Conf. Proc., (2006).

[2] A.M. Hillas. *The Origin of Ultra high-Energy Cosmic Rays.* Ann.Rev.Astron.Astrophys., 22:425–444, (1984).

[3] Anthony M. Hillas. *Cosmic Rays: Recent Progress and some Current Questions.* Cosmology, Galaxy Formation and Astroparticle Physics on the pathway to the SKA Conf. Proc., (2006).

[4] Zatsepin, G.T. and Kuzmin, V.A. *Upper limit of the spectrum of cosmic rays.* JETP Lett. Vol:4, pp: 78-80, Pisma Zh.Eksp.Teor.Fiz. 4 (1966).

[5] The IceCube Collaboration., Aartsen, M., Ackermann, M. et al. *Measurement of the multi-TeV neutrino interaction cross-section with IceCube using Earth absorption.* Nature 551, 596–600 (Nov, 2017). https://doi.org/10.1038/nature24459

[6] Longair, Malcolm S. *High Energy Astrophysics, Volume 2* Cambridge University Press. ISBN 978-0-521-43584-0, (1994).

[7] Bell, A. R. *The acceleration of cosmic rays in shock fronts – I.* Monthly Notices of the Royal Astronomical Society, Vol 182, Nu 2, Pages 147-156, (1978).

[8] Biermann, P. L. and P. A. Strittmatter. *Synchrotron emission from shock waves in active galactic nuclei.* The Astrophysical Journal 322, p. 643. doi: 10.1086/165759, (1987).

[9] Stanev, Todor. *High Energy Cosmic Rays. Springer Berlin Heidelberg.* (2010).

[10] Donald V. Reames. *The Two Sources of Solar Energetic Particles.* Space Sci. Rev. 175, 53, (2013).

[11] R. Abbasi at al. *Search for GeV Neutrino Emission During Intense Gamma-Ray Solar Flares with the IceCube Neutrino Observatory.* High Energy Astrophysical Phenomena (astro-ph.HE), arXiv:2101.00610v1, (2021).

[12] Pierre Auger Collaboration. Abraham, J. at al. *Correlation of the highest energy cosmic rays with nearby extragalactic objects.* Science, Vol 318, Pages 938-943, (2007).

[13] P. Mészáros. *Astrophysical Sources of High Energy Neutrinos in the IceCube Era.* Annual Review of Nuclear and Particle Science Vol.67, (2017).

[14] Budnik R, Katz B, MacFadyen A, Waxman E. *Cosmic Rays From Trans-Relativistic Supernovae..* Astrophys.J. 673:928 (2008).

[15] Sara Buson et al. *A Unique Messenger to Probe Active Galactic Nuclei: High-Energy Neutrinos..* Bull. Am. Astron. Soc. Volume 51, (2019).

[16] Peter Mészáros *Gamma ray bursts..* Astroparticle Physics, Volume 43, ISSN 0927-6505, (2013).

[17] Waxman E, Bahcall J. *High Energy Neutrinos from Cosmological Gamma-Ray Burst Fireballs..* Physics Review Letter. Volume 78:2292 (1997).

[18] Waxman E, Bahcall JN. *Neutrino afterglow from Gamma-Ray Bursts:* 10^{18} *eV.* Astrophysice Journal Volume 541:707-711, (2000).

[19] Gao S, Asano K, Meszaros P. *Jour. Cosmology and Astro-Particle Phys.* 11:58 (2012).

[20] H. Athar, M. Jezabek, and O. Yasuda. *Effects of neutrino mixing on high-energy cosmic neutrino flux.* Phys.Rev., D62:103007, (2000).

[21] John F. Beacom, Nicole F. Bell, Dan Hooper, Sandip Pakvasa, and Thomas J. Weiler. *Measuring flavor ratios of high-energy astrophysical neutrinos.* Phys.Rev., D68:093005, (2003).

[22] Luis A Anchordoqui, Haim Goldberg, Francis Halzen, and Thomas Weiler. *Galactic point sources of TeV antineutrinos.* Phys.Lett. B593:42, (2004).

[23] Paolo Lipari, Maurizio Lusignoli, and Davide Meloni. *Flavor Composition and Energy Spectrum of Astrophysical Neutrinos.* Phys.Rev., D75:123005, (2007).

[24] Kaoru Hagiwara et al. *Review of particle physics. Particle Data Group.* Phys.Rev., D66:010001, 2002.

[25] IceCube collaboration, M. G. Aartsen et al. *Measurements using the inelasticity distribution of multi-TeV neutrino interactions in IceCube.* Physics Review D Journal. Vol 99-3, (2019).

[26] Sheldon L. Glashow. *Resonant Scattering of Antineutrinos.* Physical Review Volume: 118.1, pp. 316–317, (1960).

[27] C. Giganti, S. Lavignac, M. Zito. *Neutrino oscillations: the rise of the PMNS paradigm.* Progress in Particle and Nuclear Physics, Vol:95, pp:1-54, (2018).

[28] G. Altarelli. *An Overview of Neutrino Mixing.* Nuclear Physics B - Proceedings Supplements, Vols: 241–242, pp: 77-82, (2013).

[29] Minako Honda, Yee Kao, Naotoshi Okamura, Tatsu Takeuchi. *A Simple parameterization of matter effects on neutrino oscillations.* e-Print: hep-ph/0602115 [hep-ph], (2006).

[30] Sebastian Euler. *Observation of oscillations of atmospheric neutrinos with the IceCube Neutrino Observatory.* Aachen: RWTH Aachen University, (2014).

[31] IceCube Collaboration, M. G. Aartsen et. al. *Evidence for High-Energy Extraterrestrial Neutrinos at the IceCube Detector.* Science 342, 1242856, [arXiv:1311.5238], (2013).

[32] IceCube Collaboration, M. G. Aartsen et. al. *Observation of High-Energy Astrophysical Neutrinos in Three Years of IceCube Data.* Phys. Rev. Lett. 113, 101101, [arXiv:1405.5303], (2014).

[33] IceCube Collaboration, Abbasi, R. and others. *The IceCube high-energy starting event sample: Description and flux characterization with 7.5 years of data.* eprint 2011.0354", archivePrefix = "arXiv", primaryClass = "astro-ph.HE", November 2020.

[34] IceCube Collaboration, M. G. Aartsen et. al. *Evidence for Astrophysical Muon Neutrinos from the Northern Sky with IceCube.* Phys. Rev. Lett., Volume 115, issue 8, August 2015.

[35] IceCube Collaboration, M. G. Aartsen et. al. *Observation and Characterization of a Cosmic Muon Neutrino Flux from the Northern Hemisphere using six years of IceCube data.* Astrophys. J., Volume 833, Nu 1, Pages 3, (2016).

[36] Joeran Stettner. *Measurement of the diffuse astrophysical muon-neutrino spectrum with ten years of IceCube data.* doi: 10.22323/1.358.1017, Proceedings of 36th International Cosmic Ray Conference — PoS(ICRC2019), Volume 358, (2019).

[37] IceCube Collaboration, M. G. Aartsen et. al. *The IceCube Realtime Alert System.* Astropart. Phys. 92, 30–41, [arXiv:1612.0602], (2017).

[38] Liverpool Telescope, MAGIC, H.E.S.S., AGILE, Kiso, VLA/17B-403, INTEGRAL, Kapteyn, Subaru, HAWC, Fermi-LAT, ASAS-SN, VERITAS, Kanata, IceCube, Swift NuSTAR Collaboration, M. G. Aartsen et. al. *Multimessenger observations of a flaring blazar coincident with high-energy neutrino.* IceCube-170922A, Science 361, eaat1378, [arXiv:1807.0881], (2018).

[39] IceCube Collaboration, M. G. Aartsen et. al. *Neutrino emission from the direction of the blazar TXS 0506+056 prior to the IceCube-170922A alert.* Science 361, 147-151, [arXiv:1807.0879], (2018).

[40] Gerard Jungman, Marc Kamionkowski, and Kim Griest. *upersymmetric dark matter.* Phys.Rept., 267:195–373, (1996).

[41] Rikard Enberg, Mary Hall Reno, and Ina Sarcevic. *Prompt neutrino fluxes from atmospheric charm.* Physical Review., D. 78:043005, (2008).

[42] T. Sanuki, M. Honda, T. Kajita, *Study of cosmic ray interaction model based on atmospheric muons for the neutrino flux calculation.* Physical Review D. 75, (2006).

[43] M. Honda, and T. Kajita. *Calculation of atmospheric neutrino flux using the interactionmodel calibrated with atmospheric muon data.* Physical Review D. (2007)

[44] G. Battistoni, A. Ferrari, T. Montaruli, and P.R. Sala. *The atmospheric neutrino flux below 100-MeV: The FLUKA results.* Astro-particle. Physics, Vol: 23, PP: 526-534, (2005).

[45] T. Stanev. *Primary cosmic ray flux.* Nuclear Physics B - Proceedings Supplements, Vol: 100, PP: 95-100, (2001).

[46] IceCube collaboration, M. G. Aartsen et al. *Measurement of Atmospheric Neutrino Oscillations at 6-56 GeV with IceCube DeepCore.* Phys. Rev. Lett. 120, 071801 - February 2018.

[47] IceCube collaboration, M. G. Aartsen et al. *Measurement of Atmospheric Tau Neutrino Appearance with IceCube DeepCore.* Phys. Rev. D, Vol 99, 032007, (2019).

[48] IceCube collaboration, M. G. Aartsen et al. *Development of an analysis to probe the neutrino mass ordering with atmospheric neutrinos using three years of IceCube DeepCore data.* Eur. Phys. J. C, Vol 80", 9, (2020).

[49] Heix, Patrick and Tilav, Serap and Wiebusch, Christopher and Zöcklein, Marit. *Seasonal Variation of Atmospheric Neutrinos in IceCube.* PoS, Vol ICRC2019, Pages 465, (2020).

[50] IceCube collaboration, M. G. Aartsen et al. *Searching for eV-scale sterile neutrinos with eight years of atmospheric neutrinos at the IceCube Neutrino Telescope.* Phys. Rev. D, Vol 102, 5, 052009, (2020).

[51] P.A. Cerenkov. *Visible radiation produced by electrons moving in a medium with velocities exceeding that of light.* Phys.Rev., 52:378–379, (1937).

[52] J.D. Jackson. *Classical electrodynamics.* Wiley, (1999).

[53] Kaoru Hagiwara et al. *Review of particle physics. Particle Data Group.* Phys.Rev., D66:010001, (2002).

[54] Kaoru Hagiwara et al. *Review of particle physics. Particle Data Group.* Phys.Rev., D66:010001, (2002).

[55] J.D. Jackson. *Classical electrodynamics.* Wiley, (1999).

[56] Normile, Dennis. *Japanese neutrino physicists think really big.* Science. American Association for the Advancement of Science.347, (2015).

[57] P.K.F. Grieder. Talk given at *Trends in Astroparticle Physics.* to appear in Nucl. Phys. B, (1994).

[58] Belolaptikov, I.A. et al. *The Baikal underwater neutrino telescope: Desing,performance, and first results.* Astroparticle Physics. 7 (3): 263. (1997).

[59] The NESTOR collaboration, *Proceedings of the Workshop on High Energy Neutrino Astrophysics,* Honolulu, Hawaii (1992).

[60] Christian Spiering. *IceCube and KM3NeT: Lessons and Relations.* DESY, Platanenallee 6, Zeuthen, 15738 Germany; (2001).

[61] P. Askebjer , S.W. Barwick y. *Optical Properties of the South Pole Ice at Depths Between 0.8 and 1 km.* Science 24 Feb 1995:Vol. 267, Issue 5201, pp. 1147-1150.

[62] G. A. Askaryan. *Excess negative charge of an electron-photon shower and its coherent radio emission.* JETP, Vol 14, Pages: 441-443, (1962).

[63] G. A. Askaryan. *Coherent radio emission from cosmic showers in air and in dense media.* JETP, Vol 21, Pages: 658, (1965).

[64] Frank G. Schroder. *Radio detection of Cosmic-Ray Air Showers and High-Energy Neutrinos.* Prog. Part. Nucl. Phys., Vol 93, Pages: 1-68, (2017).

[65] Karl-Heinz Kampert and A. Aab et al. *Multi-Messenger Physics with the Pierre Auger Observatory.* Front. Astron. Space Science, (2019).

[66] Francis Halzen, Spencer R. Klein. *Invited Review Article: IceCube: An instrument for neutrino astronomy.* 30 August (2010).

[67] R. Abbasi, Y. Abdou ,T. Abu-Zayyad. *The Design and Performance of IceCube Deep-Core.* ArXive: 1109.6096v1. 25 September (2011).

[68] IceCube collaboration, M. G. Aartsen et al. *Measurement of the cosmic ray energy spectrum with IceTop-73.* Phys. Rev. D 88 (2013) 042004.

[69] IceCube collaboration, R. Abbasi et al. *IceTop: The surface component of IceCube.* Nucl. Instrum. Meth. A 700 (2013) 188–220.

[70] R. Abbasi , Y. Abdou. et al. *IceTop: The surface component of IceCube.* ArXive: 1207.6326v2. 27 July (2012).

[71] R. Abbasi et al. *Calibration and characterization of the IceCube photomultiplier tube.* Nucl. Instrum. Meth. A 618 (2010) 139–152.

[72] E. Calvo et al., *Characterization of large-area photomultipliers under low magnetic fields: Design and performance of the magnetic shielding for the Double Chooz neutrino experiment.* Nucl. Instrum. Meth. A 621 (2010) 222–230.

[73] R. Abbasi et al., *The IceCube data acquisition system: Signal capture, digitization, and timestamping.* Nucl. Instrum. Meth. A 601 (2009) 294–316.

[74] The IceCube Collaboration: M. G. Aartsen et al., *The IceCube Neutrino Observatory: Instrumentation and Online Systems.* Prepared for submission to JINST (2017).

[75] IceCube collaboration, M.G. Aartsen et al. *The IceCube Neutrino Observatory: instrumentation and online systems.* Journal of Instrumentation 12.03 , P03012–P03012, (2017).

[76] K. Nakamura et al. *Review of particle physics.* J.Phys.G, G37:075021, 2010.

[77] Ignacio Jose Toboada Fermin. *Search for high-energy neutrino induced cascades with the AMANDA B10 detector.* PhD thesis, 2002.

[78] Eike Middell, Joseph McCartin & Michelangelo D'Agostino. *Improved Reconstruction of Cascade-like Events in IceCube.* Proceedings of the 31st ICRC. (2009).

[79] Ackermann et al. *Optical properties of deep glacial ice at the south pole.* Journal of Geophysical Research, 111:126, (2006).

[80] IceCube collaboration, F. Bos et al. *Observation of the Cosmic-Ray Shadow of the Moon and Sun with IceCube.* ASTRA Proc. 2, (2015).

[81] IceCube collaboration, M. G. Aartsen et al. *Energy Reconstruction Methods in the IceCube Neutrino Telescope.* JINST 9 (2014) P03009, [arXiv:1311.4767].

[82] Ahlers, M., Helbing, K. & Pérez de los Heros, C. *Probing particle physics with IceCube.* Phys. J. C 78, 924, (2018).

[83] IceCube collaboration, M.G. Aartsen et al. *South pole glacial climate reconstruction from multi-borehole laser particulate stratigraphy.* Journal of Glaciology 59.218, (2013).

[84] Woschnagg, Kurt et al. *Standard Candle.* IceCube Wiki.

[85] IceCube collaboration, M. Rongen et al. *Measuring the optical properties of IceCube drill holes.* EPJ Web Conf. 116, 06011, (2016).

[86] T. Hondoh et al. *T. Uchida. private communication.* J. Inclusion Phenomena , 8 , 17 (1990).

[87] Price, P. B. *Kinetics of conversion of air bubbles to air hydrate crystals in Antarctic ice.* Science, 267, 1802 – 1804, (1995).

[88] Price, P. B., and L. Bergstrom. *Optical properties of deep ice at the South Pole: Scattering.* Appl. Opt., 36, 4181 – 4194, (1997).

[89] Price, P. B., K. Woschnagg, and D. Chirkin. *Age vs depth of glacial ice at South Pole.* Geophys. Res. Lett., 27(14), 2129 – 2132, (2000).

[90] Kurt Woschnagg, P. Buford Price. *Temperature dependance of absorption in ice at 532nm.* Applied Optics, Vol 40, No 15, 20 May (2001).

[91] Woschnagg, K., and P. B. Price. *Temperature dependence of absorption in ice at 532 nm.* Appl. Opt., 40, 2496 – 2500, (2001).

[92] Price PB, Nagornov OV. *Temperature profile for glacial ice at the South Pole: implications for life in a nearby subglacial lake.* Proc Natl Acad Sci USA. 2002 Jun 11;99(12):7844-7.

[93] Delmonte, B., J. R. Petit, and V. Maggi. *Glacial to Holocene implications of the new 27000-year dust record from the EPICA Dome C(East Antarctica) ice core.* Clim. Dyn., 18, 647 – 660, (2002).

[94] L. G. Henyey and J. L. Greenstein. *Diffuse radiation in the Galaxy.* Annales d'Astrophysique, 3:117, Jan (1940).

[95] P. Buford Price and Lars Bergström. *Optical properties of deep ice at the south pole: scattering.* Appl. Opt., 36(18):4181–4194, Jun 1997.

[96] Price, P. B., and L. Bergstrom. *Enhanced Rayleigh scattering as a signature of nanoscale defects in highly transparent solids.* Philos. Mag. A, 75, 1383 – 1390, (1997).

[97] Dmitry Chirkin. *Photon tracking with GPUs in IceCube.* Nuclear Instruments and Methods in Physics Research Section A: Accelerators, Spectrometers, Detectors and Associated Equipment 725, pp. 141–143. (2013).

[98] Dimitry Chirkin. *Spice powerpoint.* Presented at IceCube collaboration meeting, September (2010).

[99] Pingyu Liu. *A new phase function approximating to mie scattering for radiative transport equations.* Physics in Medicine and Biology, 39(6):1025, (1994).

[100] Francis Halzen and Spencer R. Klein. *IceCube: An Instrument for Neutrino Astronomy.* (2010).

[101] Dmitry Chirkin. *Study of ice transparency with icecube flashers.* IceCube Collaboration, University of Wisconsin.

[102] IceCube collaboration, M. G. Aartsen et al. *Energy Reconstruction Methods in the IceCube Neutrino Telescope.* JINST 9 (2014) P03009, [arXiv:1311.4767].

[103] Wendt, Chris and Dahai Liu. *"PMT Saturation Lab, In-Ice, FAT." IceCube Collaboration Meeting Baton Rouge.* (2006).

[104] Dmitry Chirkin and Martin Rongen. *Light diffusion in birefringent polycrystals and the IceCube ice anisotropy.* arXiv: 1908.07608v1 [astro-ph.HE], (2019).

[105] Bohren, C.F. and D.R. Huffman. *Absorption and Scattering of Light by Small Particles.* Wiley Science Series. Wiley. url: https://books.google.de/books?id=ib3EMXXIRXUC, (2008).

[106] Zhang, Z. and H.J. Caulfield. *Reflection and refraction by interfaces of uniaxial crystals.* Optics Laser Technology 28.7, pp. 549–553. doi: https://doi.org/10.1016/S0030-3992(96)00022-9, (1996).

[107] E. Calvo et al., *Characterization of large-area photomultipliers under low magnetic fields: Design and performance of the magnetic shielding for the Double Chooz neutrino experiment.* Nucl. Instrum. Meth. A 621 pp. 222–230. (2010).

[108] Henyey, L. C. and J. L. Greenstein. *Diffuse radiation in the Galaxy.* The Astrophysical Journal 93, p. 70. doi: 10.1086/144246. (1941).

[109] Pingyu Liu. *A new phase function approximating to Mie scattering for radiative transport equations.* Physics in Medicine and Biology 39.6, p. 1025. (1994).

[110] Dmitry Chirkin. *Likelihood description for comparing data with simulation of limited statistics.* arxive: 1304.0735vs", (2013).

[111] Jeffrey D. Scargle. *Studies in Astronomical Time Series Analysis. V. Bayesian Blocks, a New Method to Analyze Structure in Photon Counting Data.* The Astrophysical Journal 504.1, pp. 405–418. (1998).

[112] Karle, A. and K. Woschnagg. *Hole Ice Studies with YAG data/MC.* AMANDA internal report, (1998).

[113] IceCube Calibration Group, *LED angular emission profile.* IceCube Wiki Page, (2007).

[114] IceCube Calibration Group, *Photon Propagation Code (ppc).* IceCube Wiki Page, (2009), Last Updated June-2020.

[115] Jeffrey D. Scargle. *Studies in Astronomical Time Series Analysis. V. Bayesian Blocks, a New Method to Analyze Structure in Photon Counting Data.* The Astrophysical Journal, 504:405-418, (1998).

[116] Delia Tosi, Christopher Wendt. *Calibrating the photon detection efficiency in IceCube.* Proceedings of Technology and Instrumentation in Particle Physics 2014, arXiv:1502.03102, (2015).

[117] Dawn Williams, et al. *Flasher Timing Offset.* IceCube Wiki Page, (2007).

[118] Y. D. He & P. B. Price *Remote sensing of dust in deep ice at the South Pole.* Journal of Geophysical Research, 03, 17,041–17,056. (1998).

[119] Khadka Bahadur Chhetri. *Computation of Errors and Their Analysis on Physics Experiments.* Himalayan Physics 3:78, (2013).

[120] P. B. Price, K. Woschnagg. *Role of Group and Phase Velocity in High-Energy Neutrino Observatories.* Journal of Astroparticle Physics., 15, 97-100. (2001).